

Design and Characterization of a Multi-beam Micro-CT Scanner based on Carbon Nanotube Field Emission X-Ray Technology

Rui Peng

A dissertation submitted to the faculty of the University of North Carolina at Chapel Hill in partial fulfillment of the requirement for the degree of Doctor of Philosophy in the Curriculum in Applied Science and Engineering.

Chapel Hill
2010

Approved by

Advisor: Dr. Otto Z. Zhou

Reader: Dr. Jianping Lu

Reader: Dr. David Lalush

Reader: Dr. Sha X. Chang

Reader: Dr. Richard Semelka

© 2010
Rui Peng
ALL RIGHTS RESERVED

ABSTRACT

Rui Peng

Design and Characterization of a Multi-beam Micro-CT Scanner Based on Carbon Nanotube Field Emission Technology

(Under the direction of Professor Otto Zhou)

In this dissertation, I will present the results for my Ph.D. research for the past five years. My project mainly focuses on advanced imaging applications with a multi-beam x-ray source array based on carbon nanotube field emission technology. In the past few years, research in carbon nanotubes gradually changed from the raw material science to its application. Field emission x-ray application is one of the hottest research areas for carbon nanotube. Compared to traditional thermionic x-ray sources, the carbon nanotube field emission x-ray source has some natural advantages over traditional thermionic x-ray sources such as instantaneous x-ray generation, programmability and miniaturization.

For the past few years, the research and development of carbon nanotube field emission x-ray has shifted from single x-ray beam applications to spatially distributed multi-beam x-ray sources. Previously in Zhou group, we have already built a gated micro-CT system with single beam micro-focus x-ray tube for higher spatial and temporal resolution as required in live animal imaging and a multi-beam tomosynthesis

system targeting for faster and more stable breast imaging. Now my project mainly focused on the design, characterization and optimization of a multi-beam micro-CT imaging system. With the increase of gantry rotation speed approaching the mechanical limit, it is getting more and more difficult to further speed up the CT scanning. My new system promises a potential solution for the problem, and it serves as a great test platform for truly stationary micro-CT geometry. The potential capabilities it showed during the characterization and imaging measurements was promising.

The dissertation is composed of five chapters. In Chapter 1, I will generally review the physics principles of x-ray generation and interaction with matter. Then the discovery of carbon nanotube and its great potential to serve as an excellent field emission electron source will be introduced in the second chapter, also the synthesis and technique of carbon nanotube field emission x-ray source fabrication demonstrated. Chapter 3 will be mainly describing the design of the multi-beam micro-CT system. Afterwards characterization, optimization and results from imaging measurements will be discussed in Chapter 4. Finally the conclusion and future work of this field will be given in Chapter 5.

ACKNOWLEDGEMENT

The past six years at UNC Chapel Hill will always be my unforgettable experience for lifetime. Ph.D. education to me is the systematic training of independent thinking and research. Towards the completion of this degree, I'm so grateful for all the guidance, help and support from my mentors, colleagues, friends, and family.

I want to thank my advisor Dr. Zhou for his guidance and encouragement throughout my graduate studies. His enthusiasm and dedication in converting laboratory research into useful application truly inspire my own understanding of science and engineering. I also highly appreciate all the professors in my committee, Dr. Jianping Lu, Dr. David Lalush, Dr. Sha Chang, and Dr. Richard Semelka for their advice and discussion.

Also, I would like to express my gratitude toward fellow members of Zhou research group. Thanks to Xiomara Calderon-Colon, David Bordelon, Ramya Rajaram, Shabana Sultana, Zhijun Liu, Mathew McIntosh, and Tuyen Phan for working with me along the way as fellow students. Your friendship and support have made this process much more joyful. Thanks to the post-docs and research scientists in our lab, Zejian Liu, Lei An, Sigen Wang, Xin Qian, Yueh Lee and Guohua Cao, who have supported me throughout this process with friendship and expertise. Many thanks to Christy Redmon,

who has been taking care of the supporting tasks for this project and the entire group. Many thanks to Ms. Carolyn Newman, for being a friend and taking care of all the material science students. Special thanks to Jian Zhang, Guang Yang and Peng Wang, who have passed their hands-on experience to me. Your experiences and suggestions are of great help to me for the successful completion of this project. Finally, I'm so grateful for the never-ending support and understanding from my family for all these years.

At last, this work could not have been possible without the support from National Institute of Biomedical Imaging and Bioengineering, National Cancer Institute, Xintek Inc, and Xinray systems.

TABLE OF CONTENTS

CHAPTER 1	INTRODUCTION AND BACKGROUND	1
1-1	Historical review of X-ray radiation.....	1
1-2	Fundamentals of x-ray generation.....	3
1-3	Interaction between x-ray and matter	10
1-3-1	Coherent scattering	11
1-3-2	Compton Scattering.....	12
1-3-3	Photoelectric effect	13
1-4	Attenuation of x-ray.....	15
1-5	X-ray source technology.....	19
1-5-1	Conventional x-ray tube	20
1-5-2	Synchrotron X-ray Source.....	24
1-6	X-ray Source Based on CNT	26
CHAPTER 2	CARBON NANOTUBE FIELD EMISSION AND ITS APPLICATION	29
2-1	Fundamentals of Carbon Nanotube (CNT)	30
2-1-1	History of the discovery of carbon nanotube.....	30
2-1-2	The Structure of CNT	31
2-1-3	Properties of CNT.....	33
2-2	Applications of CNTs in field emission	35

2-2-1	Thermionic emission.....	37
2-2-2	Field emission	39
2-2-3	Carbon nanotube in field emission.....	42
2-3	Fabrication of CNT field emission cathode.....	45
2-3-1	Electrophoresis Deposition (EPD) of CNT electron source.....	46
2-3-2	Fabrication of CNT cathode	47
2-3-3	Field emission characterization for the Si-based cathode	54
CHAPTER 3	DESIGN OF MULTI-BEAM MICRO-CT SCANNER ...	61
3-1	Overview of computed tomography (CT) and Micro-CT.....	62
3-2	Micro-CT imaging system with single-beam CNT micro-focus x-ray tube	65
3-3	Design of a Multi-Beam Micro-CT system based on CNT field emission technology.....	68
3-3-1	The evolution of CT geometry for faster scanning.....	68
3-3-2	Design of multi-beam micro-CT scanner	71
3-3-3	System overview.....	72
3-3-4	Multi-beam field emission x-ray source design.....	74
3-3-5	System control circuitry and software interface	82
CHAPTER 4	PRELIMINARY CHARACTERIZATION AND OTHER IMAGING APPLICATIONS OF MULTI-BEAM MICRO-CT	91
4-1	System Integration.....	91
4-2	Preliminary characterization	94
4-2-1	MBFEX field emission performance and current regulation.....	94
4-2-2	Control circuit timing test.....	98
4-2-3	Focal spot size characterization.....	100

4-3	Mouse imaging with the multi-beam micro-CT system.....	102
4-4	Multiplexing imaging investigation	107
4-4-1	Multiplexing with CNT field emission x-ray.....	108
4-4-2	Noise characteristic in the multi-beam micro-CT system	110
4-4-3	Results and Discussion.....	117
4-5	Summary.....	127
CHAPTER 5	CONCLUSION AND FUTURE DIRECTION	130

LIST OF FIGURES

- Figure 1-1 Prof. Wilhelm Conrad Röntgen and the very first x-ray image from Ms. Röntgen's hand (Image reproduced from: http://www.nlm.nih.gov/exhibition/dreamanatomy/da_g_Z-1.html) 2
- Figure 1-2 (a) The Chandra X-ray telescope is launched in July 1999 (reproduced from <http://jelley.wustl.edu/x-ray/>) (b) Burke D8 Advance X-ray diffraction machine (reproduced from www.wmi.badw.de/methods/xray.htm) (c) Analogic OnGuard DualUse airport security machine (reproduced from <http://www.analogic.com/products-security-checkpoint-onguard-dualuse.htm>) (d) Siemens SOMATOM Definition dual source CT scanner (reproduced from <http://www.medical.siemens.com/>) 3
- Figure 1-3 electromagnetic wavelength range[2] 4
- Figure 1-4 A: Excitation (left) and de-excitation (right) with the subsequent release of electromagnetic radiation. B: Ionization and the production of delta rays. (reproduced from [13])..... 6
- Figure 1-5 A typical X-ray spectrum with a tungsten target at 150kVp. Both filtered Bremsstrahlung and characteristic radiation are showed 7
- Figure 1-6 Bremsstrahlung radiation arises from energetic electron interactions with an atomic nucleus. In a close approach, the positive nucleus attracts the negative electron, causing deceleration and redirection, thus a loss of kinetic energy that is converted to an x-ray. (reproduced from [13]) 8
- Figure 1-7 a. Generation of a characteristic x-ray in a target atom occurs as following (1) the incident electron interacts with the K-shell electron (2) the K-shell electron is removed (only if the energy of the incident electron is greater than the binding energy), leaving a vacancy in the K shell. (3) an electron from the adjacent L shell (or other higher energy level shells) fills the vacancy. (4) a K_{α} characteristic x-ray photon is emitted with an energy equal to the difference between the binding energies of the two shells. b. The filtered spectrum of bremsstrahlung and characteristic radiation from a tungsten target with 90kVp depicts specific characteristic radiation energies from K_{α} and K_{β} transitions. (reproduced from [13])..... 10
- Figure 1-8 Coherent scattering process shows that the incident photon λ_1 interacts with the target atom and the scattered photon λ_2 is then emitted with almost the same energy merely towards a different direction. (reproduced from [13]) 11

Figure 1-9 Compton scattering. The incident photon with energy E_0 interacts with a M shell electron that results in the emission of the Compton electron E_{e-} as well as the Compton scattered photon E_{sc} at an angle θ . (reproduced from [13]).....	13
Figure 1-10 The photoelectric effect. Left diagram shows the photoelectric absorption between a 100 keV photon and an iodine atom. The K shell electron is ejected with a kinetic energy equal to the difference between incident photon energy and K shell binding energy. And the vacancy in the K-shell results in the transition of L-shell electron to K-shell, emitting K_{α} characteristic x-ray with energy equal to the difference in binding energies. Furthermore the electron cascade will continue to emit other characteristic x-rays in lower energy. The sum of all these characteristic x-ray energies equal to the binding energy of the ejected photoelectron. (reproduced from [13]).....	14
Figure 1-11 Diagram of attenuation resulted from x-ray photons traversing matter with certain thickness. The absorbed and scattered photons, Δn , are proportional to n and Δx . [14].....	17
Figure 1-12 Polyenergetic x-ray beam “hardens” resulted from lower energy photons being absorbed as they traverse matter. (reproduced from [13]).....	19
Figure 1-13 Schematics of a stationary anode x-ray tube. (reproduced from [13]).....	20
Figure 1-14 Illustration of anode heel effect. (reproduced from [13])	22
Figure 1-15 the illustration of line focus principle. (a) a square (isotropic) cathode source would produce rectangular effective focal spot after projection. (b) a rectangular electron source could be used to produce an isotropic (square) effective focal spot.[14].....	23
Figure 1-16. Schematics of generation of synchrotron x-ray radiation and its properties. http://www.bessy.de/guided_tour/en.02.sr.php?docs=2	25
Figure 2-1 a. The structure of C_{60}	31
Figure 2-2 (a) The graphene sheet labeled with integers (n, m), which could determine the diameter, chiral angle and type of the nanotube. (b), (c) and (d) are schematics for zigzag, chiral and armchair nanotube respectively[8]	32
Figure 2-3. Applications based on CNTs. (a): AFM tip equipped with CNT. (b): Infineon Technologies designed this carbon nanotube transistor, and it is one of the smallest ever made. (c) DNA wrapped SWNT used as biosensor in living cells.[20] (d): Field emission display based on CNT (courtesy of Xintek Inc.).	36

Figure 2-4 Potential energy for an electron in the vicinity of a metal surface with/without applied field. The dashed line shows the energy barrier that an electron must overcome to escape to the vacuum level without external field, while the solid lines shows the reduction of energy barrier both in height and width with an external field applied. [21]	38
Figure 2-5 (a) Microfabrication procedure for a Spindt type metal tip (b) the SEM image of the cross section of a Spindt tip	43
Figure 2-6 Schematics of arcing damage to Spindt-type emitters (left) and to CNT emitters (right) [19].	44
Figure 2-7 Schematic diagram of EPD set-up. CNTs are attracted to the negative electrode and bond to the conducting parts of the substrate and form a pre-defined area coating. [40]	47
Figure 2-8 SEM images showing the top surface of the composite CNT film both: (a) before and (b) after vacuum annealing. The CNTs are randomly oriented on the surface. (c) Corss-sectional SEM image of the CNT cathode after the activation process. The surface CNTs are now vertically aligned in the direction perpendicular to the substrate surface. Corss-sectional SEM images of two cathodes fabricated under the same conditions except different CNT concentrations in the EPD suspension. Cathode in (e) was made in a suspension with 4× the CNT concentration than the cathode in (d).[41]	49
Figure 2-9 (a) Cylindrical metal substrate and shadow mask made of Teflon. (b) a pre-cut 2" silicon wafer with cathode pattern deposited by metal sputtering and photolithography	51
Figure 2-10 The fabrication procedure of photomasked silicon based EPD substrates...	52
Figure 2-11 (a) the post-cut silicon based substrate with five CNT cathodes deposited. Copper stripes are used as conducting material for both EPD process and the field emission. Cathode is 1mm circular shape. The spacing between CNT cathodes is 5mm. (b) a specially designed EPD sample holder for the substrates in (a). It holds two substrates at a time so that a total number of ten CNT cathodes could be produced simultaneously.....	53
Figure 2-12 Left: the customized field emission sample holder for the silicon based 5-cathode substrate. It can measure three cathodes' performance at one time. Right: the simplified field emission scheme. A metal plate is served as anode with an external resistor connected as protector, while the cathode substrate is connected the ammeter for emission current measurement. ...	54

Figure 2-13. Field emission I-V curves of three cathodes on the same silicon substrate demonstrate good uniformity	55
Figure 3-1 The geometries of the first four generations of CT scanners. A. Evolution of the CT scanner: (a) The first-generation of scanner using a pencil x-ray beam and a single detector. (b) The second-generation of scanner with a fan x-ray beam and multiple detectors. (c) The third-generation of scanner using a fan x-ray beam and detector array. (d) The fourth-generation of scanner with a fan beam and a stationary circular detector array.....	64
Figure 3-2 (a) A micro-focus x-ray tube with CNT field emission x-ray source. It could stably generate as high as 2 mA tube current and 100 μm effective focal spot x-ray beam. [24](b) A dynamic single-beam micro-CT scanner equipped with CNT micro-focus x-ray tube. It can provide 10 ms temporal resolution at 81 μm spatial resolution. This system has the capability of live animal free breathing gated CT for both respiratory and cardiac imaging.[26].....	66
Figure 3-3 Axial (a, b) and coronal (c, d) slice images of a wild-type mouse at 0 msec (a, c) and 55 msec (b, d) after the R wave.....	67
Figure 3-4 (a) Conventional CT scans take pictures of slices of the body, then translate the patient. These slices are a few millimeters apart. (b) The newer spiral (also called helical) CT scan takes continuous pictures of the body in a rapid spiral motion, so that there are no gaps in the pictures collected.. Reproduced from (imaging.cancer.gov)	69
Figure 3-5 (a) The DSCT scanner from Siemens. This scanner consists of two x-ray tubes and two sets of detectors with 90° offset particularly designed for cardiac CT imaging. Shortest gantry rotation time is 0.33s. (b) Skyscan 1180 high throughput dual source micro-CT.....	70
Figure 3-6 Alternative concepts for fast volume scanning (a) EBCT permits single scans in the range of 30 to 100 ms without mechanical motion. (b) DSR allowed volume scanning in cone-beam geometry with 1 s rotation time. (reproduced from [36]).....	71
Figure 3-7 imaging geometry of the multi-beam micro-CT system.....	73
Figure 3-8 Schematic drawing of the multi-beam x-ray imaging system with a 20-beam MBFEX x-ray source array, a rotation stage, and a flat panel x-ray detector.	74
Figure 3-9 (a) The CAD drawing of the newly designed multi-beam x-ray tube assembly which includes a Molybdenum x-ray anode housed in a stainless steel assembly with 12° tilting angle, a Einzel focusing lens, an electron extraction	

gate electrode and an 20-beam integrated CNT field emission cathode array (b) The as-fabricated multi-beam x-ray source assembly. The metal surfaces were highly polished and all the materials were HV compatible to improve source stability during high voltage operation.....	75
Figure 3-10. (a) The CNT cathode array has 20 CNT field emission cathode deposited on a single glass chip substrate. (b) Line focus principle: the emitting cathode was designed to have an elliptical shape in order to achieve a desired isotropic focal spot for x-ray imaging.	79
Figure 3-11 (a) The newly designed two-stage Einzel lens for the integrated MBFEX source array. (b) The simulation results of focal spot size as a function of focusing voltage applied on focusing electrode 2.....	81
Figure 3-12(a) The MOSFET based control circuitry used for triggering x-ray generation and (b) its working principle	83
Figure 3-13 Timing diagram for sequential scanning beam generation from the multi- beam micro-CT system.....	84
Figure 3-14 (a) Software UI in CT mode with integrated rotor control and two imaging modes (b) Software UI in a multiplexing planar imaging mode with a cross- wire phantom. 4 x-ray beams are switched on simultaneously.....	85
Figure 4-1 (a) specially designed multi-pin connection unit for cathode individual control (b) the connection unit is connected to the external circuit via a UHV rate ribbon cable	93
Figure 4-2 The overview of the assembled MB μ CT system.....	94
Figure 4-3 (a) Measured field emission current as a function of applied electrical field from 20 CNT cathodes deposited on the glass substrate. The measurement was done under standard parallel plate geometry (inset). (b) Required electric fields to obtain 1 mA cathode current from all 20 CNT cathodes....	95
Figure 4-4 The adjustable serial resistor array is used to modulate emission currents from different cathodes and increase the uniformity of the generated x-ray flux.	96
Figure 4-5 Homebrew field emission measurement program for multi-beam micro-CT system. User can switch on different beams and generate different waveform of x-ray pulses within the program. It could also record the data and display the I-V curve and F-N plot in real time.....	97
Figure 4-6 (a) Initial spread of field emission I-V curves from different CNT field emission cathodes. (b) Relative uniform field emission characteristics from the same	

batch of CNT cathodes after applying a ballast resistor based compensation loop.	98
Figure 4-7 (a) timing diagram showing 2 x-ray triggers (channel 1 and 2) synchronize precisely with the detector integration window (channel 3). (b) Channel 1-4 shows the triggers for first 4 x-ray beams are switched on sequentially. (c) Channel 1-4 shows the first 4 x-ray beams in a multiplexing scanning mode, clearly multiple beams are switched on simultaneously in a single imaging cycle.	99
Figure 4-8 (a) The LabVIEW control software UI in a focal spot size measurement, area in green line stands for the area chosen for line profile and FSS calculation. A standard Tungsten cross wire phantom was used for the focal spot measurement. (b) The experimentally measured optimal focal spot sizes of different emitting cathodes under their corresponding focusing voltage settings. Focal spot sizes around $100\mu\text{m} \times 100\mu\text{m}$ were achievable for all the emitting cathodes by tuning the corresponding focusing voltages.	102
Figure 4-9 The LabView based control software for the prototype MB μ CT scanner.....	103
Figure 4-10 Image acquisition flow chart for the MB μ CT imaging system.....	104
Figure 4-11 Projection images recorded at 0° (a), 112° (b), and 224° (c). (d) Illustration of the difference in projection angle from 4 pixels. Each image in individual group demonstrate different projection angle	106
Figure 4-12 seven element Hadarmad coding matrix and corresponding pulse generation sequence in the right.	110
Figure 4-13 Relative noise level versus proportional-to-constant noise ratio in a seven-source system from simulation results.[8]	111
Figure 4-14 illustration of the experimental geometry settings for 7-beam binary multiplexing	112
Figure 4-15 Field emission measurements for the chosen 7 beams	113
Figure 4-16 7-beam binary multiplexing with a mouse carcass with the geometry introduced above. (a) Sequential Projection images from 7 X-ray beams from MB μ CT, the horizontal translation of mouse body clearly depicts the difference in projection angles from 7 beams (b) Superimposed projection images from 4 beams simultaneously illuminating the same mouse based on a certain sequence (C) Demultiplexed images from the decoding of the superimposed images.....	114

Figure 4-17 (a) the customized signal-to-noise ratio phantom consists of two acrylic plates and an insert of crossed aluminum foil (b) the crossed aluminum foil insert. With different folds of aluminum foil, the area is divided into several smaller regions with different x-ray attenuation. 115

Figure 4-18 illustration of the implication of dark frame subtraction. 5-a is raw image with phantom in the FOV, while 5-b is the raw dark image. There were quite a few bright spots and a dead line in the FOV. After correction, 5-a and 5-b became 5-c and 5-d respectively, with obvious reduction of bright pixels. Then we subtracted 5-d from 5-c and have our final image of 5-e..... 116

Figure 4-19 Mean intensity of ROI in ADU versus standard deviation 120

Figure 4-20 (a) is a single dark frame, (b) is the a subtracted the reference 122

Figure 4-21 Standard deviation of all 2480 frames of dark images with the reference subtracted..... 123

Figure 4-22 P value of our imaging system under the experimental condition. Total 28 curves were listed in the graph, illustrating data from 7 different x-ray beams with 4 identical exposures at each time spot. 124

Figure 4-23 The mean of SNR ratio between a demultiplexed image and sequential image across the 7 beams. 126

Chapter 1 Introduction and Background

1-1 Historical review of X-ray radiation

During the past century after its discovery, x-ray related technology has emerged from planar radiography to three-dimensional computed tomography and radiation therapy. It all started in 1895, when x-rays were first discovered by Prof. Wilhelm Conrad Röntgen, a physicist at Julius Maximilian University of Würzburg in Germany) [1, 2]. During the experiment with a cathode ray tube, he noticed that a screen across the room fluoresced despite the fact that the tube was covered in a black cardboard box and the screen was simply too far away for the cathode ray to hit. He then realized that he might discover an invisible “light”, and named it “x-ray” afterwards.

The discovery of x-rays earned him the Nobel Prize in Physics in 1901, which was the very first Nobel Prize in history. Although having a great discovery, Röntgen did not patent it so that the newly discovered x-rays could be used freely for anyone in various areas. Without many barriers, scientists from different areas started to work on the possible applications with this new x-ray technology. Only two months after Röntgen’s discovery, Drs. Ratcliffe and Hall-Edwards used x-ray in medical examination for the first time.



Figure 1-1 Prof. Wilhelm Conrad Röntgen and the very first x-ray image from Ms. Röntgen's hand (Image reproduced from: http://www.nlm.nih.gov/exhibition/dreamanatomy/da_g_Z-1.html)

Later on, the application of x-ray gradually spread to science and engineering, astronomy, medical science and many other industries. Most of those applications utilize the property of interaction between x-ray and matter. In astronomy and cosmology, x-ray satellites detect and transmit the data about the x-ray emission from celestial objects, while x-ray telescopes are used to observe remote objects in x-ray spectrum[3]. In material sciences, x-ray crystallography investigates the lattice structure and spatial configuration of atoms in different materials by the x-ray diffraction pattern. Another major application for x-ray is imaging, mainly relying on the attenuation of x-ray photons from different matter [4-7]. In airport, x-ray imaging is used to detect safety hazards; in industry, it's widely used to find cracks and leakage; in medicine, x-ray

imaging such as computed tomography and mammography, is also an important non-invasive diagnostic tool[8]. Figure shows some of the common x-ray applications mentioned above.

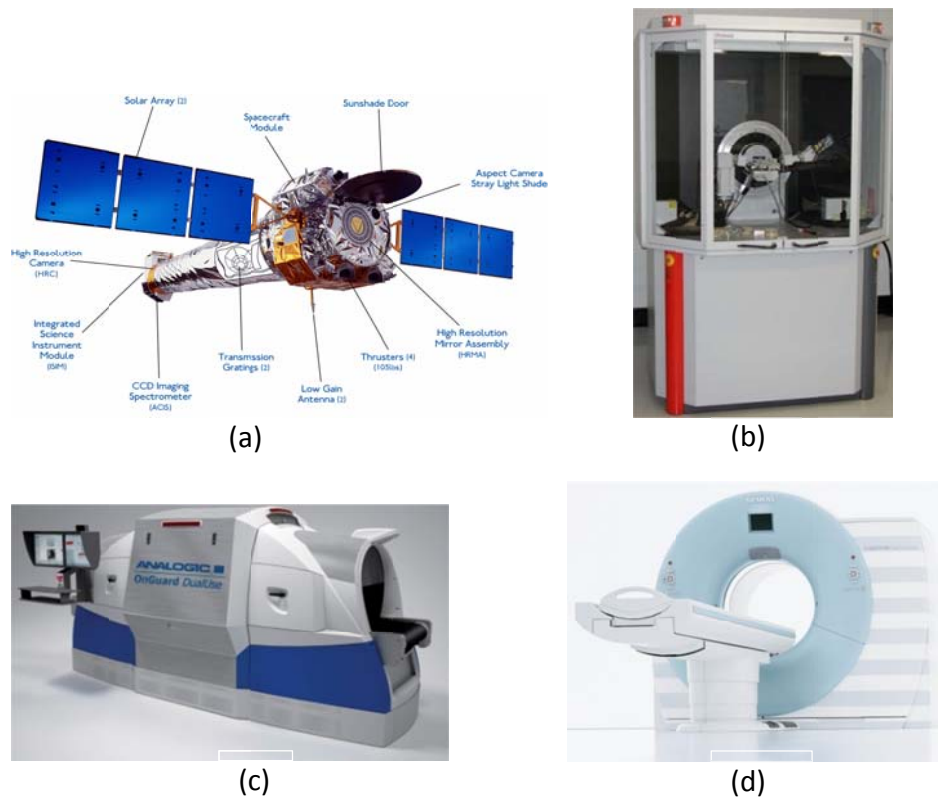


Figure 1-2 (a) The Chandra X-ray telescope is launched in July 1999 (reproduced from <http://jelley.wustl.edu/x-ray/>) (b) Burke D8 Advance X-ray diffraction machine (reproduced from www.wmi.badw.de/methods/xray.htm) (c) Analogic OnGuard DualUse airport security machine (reproduced from <http://www.analogic.com/products-security-checkpoint-onguard-dualuse.htm>) (d) Siemens SOMATOM Definition dual source CT scanner (reproduced from <http://www.medical.siemens.com/>)

1-2 Fundamentals of x-ray generation

X-ray is a specific kind of electromagnetic radiation with short wavelength [2, 9, 10]. Generally x-ray is produced by interaction between highly energetic electrons and

matter. The kinetic energy of the electron is then transformed into electromagnetic energy. Typical wavelength of x-ray (λ) ranges from about 10^{-8} meters to 10^{-12} meters, with corresponding photon energies $E = 120$ eV to 1.2 MeV. Higher energy (shorter wavelength) photons are called γ -rays, and lower energy radiation (longer wavelength) photons are called ultraviolet (UV).

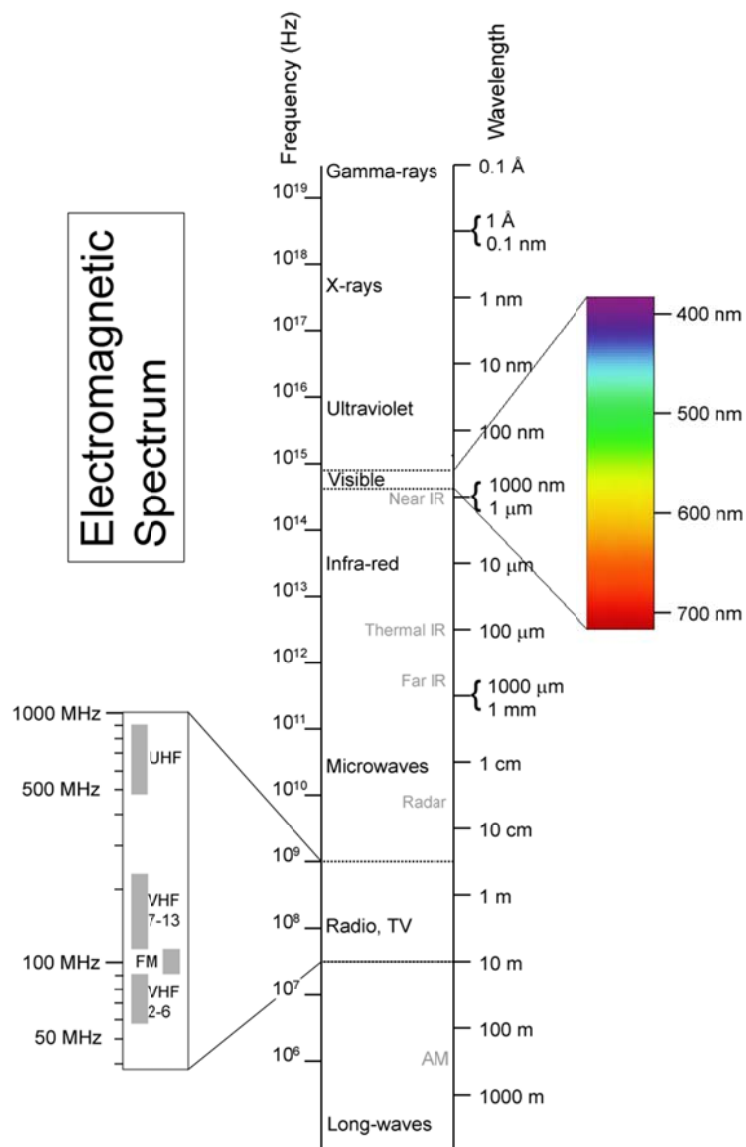


Figure 1-3 electromagnetic wavelength range[2]

X-rays are generated in two different ways: either by electrons switching energy levels within an atom or by interaction encountered by free electrons [2, 9-12].

Electrons move around the nucleus of atom within shells at various energy levels. When an electron occupies an energy shell greater than its ground state, namely the state of lowest energy level, it is in an excited state. Given extra energy, such as absorbing a photon or colliding with a nearby particle, an electron could become excited. However, it could not stay in an excited state for very long, and will return to the ground state. When it does so, a photon is emitted which has the same energy as the difference in energy level between the excited and ground state. Since the energy and wavelength of the photon are related, we see this photon at a specific wavelength in the spectrum.

Because there are many energy shells in any particular atom, there are many different possible energies with different initial and final values. When an atom is in an excited state, the electron can drop all the way to the ground state, or stop in an intermediate level, generating photons in different wavelength. Of the common elements in the universe, Fe and O usually are the two most prominent sources of X-ray lines as well as other rare proton-rich elements and radioactive isotopes.

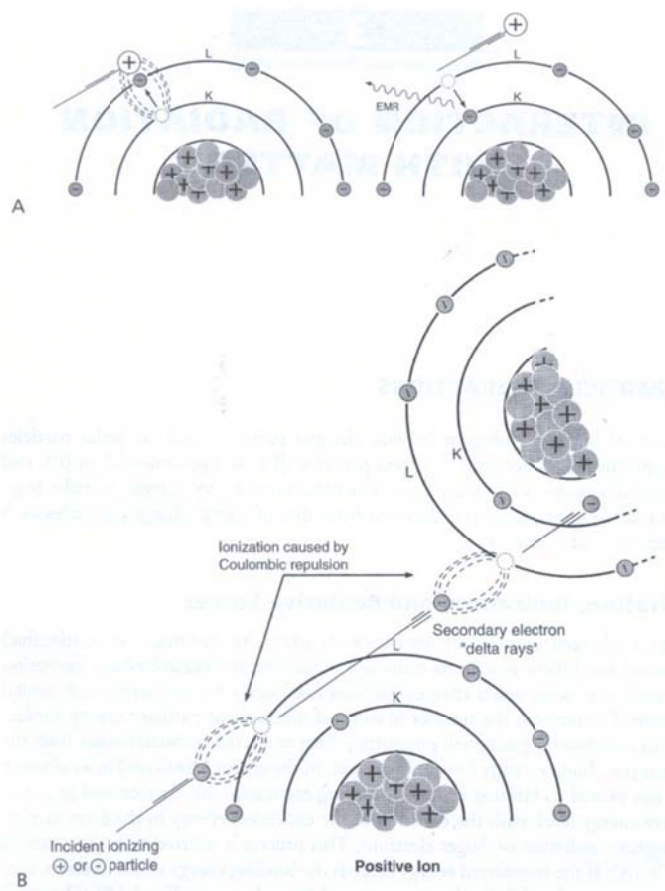


Figure 1-4 A: Excitation (left) and de-excitation (right) with the subsequent release of electromagnetic radiation. B: Ionization and the production of delta rays. (reproduced from [13])

On the other hand, X-ray could also be generated when free electrons interact with matter. There are two types of radiation associated with the x-ray generation from free electrons, white/continuous radiation (Bremsstrahlung) [2] and characteristic radiation as depicted in Figure 1-5.

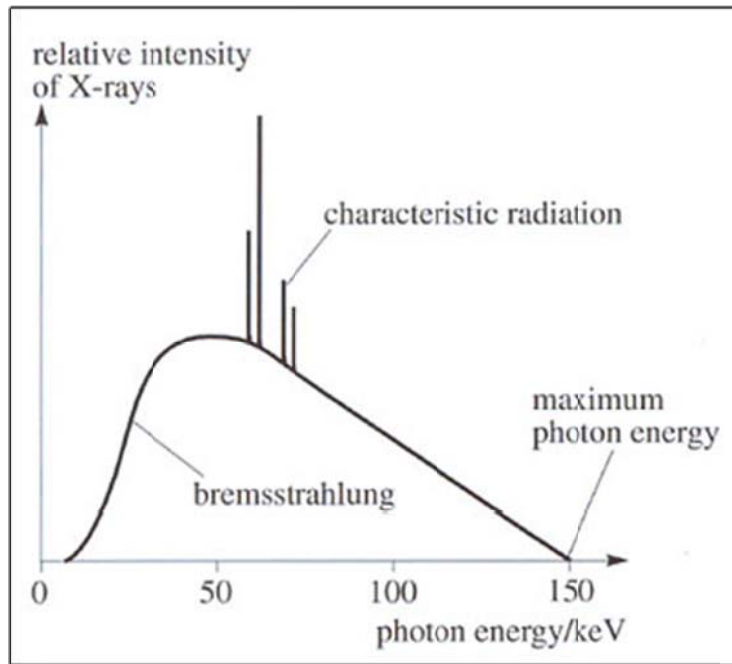


Figure 1-5 A typical X-ray spectrum with a tungsten target at 150kVp. Both filtered Bremsstrahlung and characteristic radiation are showed

Bremsstrahlung means “braking radiation” in German, and it describes the radiation emitted when fast-moving electrons are decelerated or in other words “braked” in certain circumstances, such as accelerating past a charged particle or another photon and moving in a electromagnetic field. The most common situation is the emission from a hot gas as the electrons collide with the nuclei due to their random thermal motions. This is called “thermal bremsstrahlung”. Another type of bremsstrahlung that is discussed more frequently in medical imaging happens when fast-moving electrons decelerated when approaching the positive nuclear field of an atom. Such interactions reduce the kinetic energies of the incident electrons and give off electromagnetic radiation, and when energy is high enough, that radiation is in the

X-ray region of the electromagnetic spectrum. The kinetic energy of the incident electrons could not be dissipated completely in a single collision. Typically, these colliding electrons hit electrons in the target material with a glancing blow dissipating some energy as emitted X-ray photons. Then these photoelectrons hit other electrons in the target material emitting lower energy X-ray photons or hit valence electrons producing heat. Thus the white radiation spectrum does have a minimum wavelength or maximum energy related to the kinetic energy of the incident radiation beam, and continues to longer wavelengths or lower energies until all of the kinetic energy is absorbed. The highest intensity of emitted white radiation spectrum is obtained at a wavelength that is about 1.5 times the minimum wavelength.

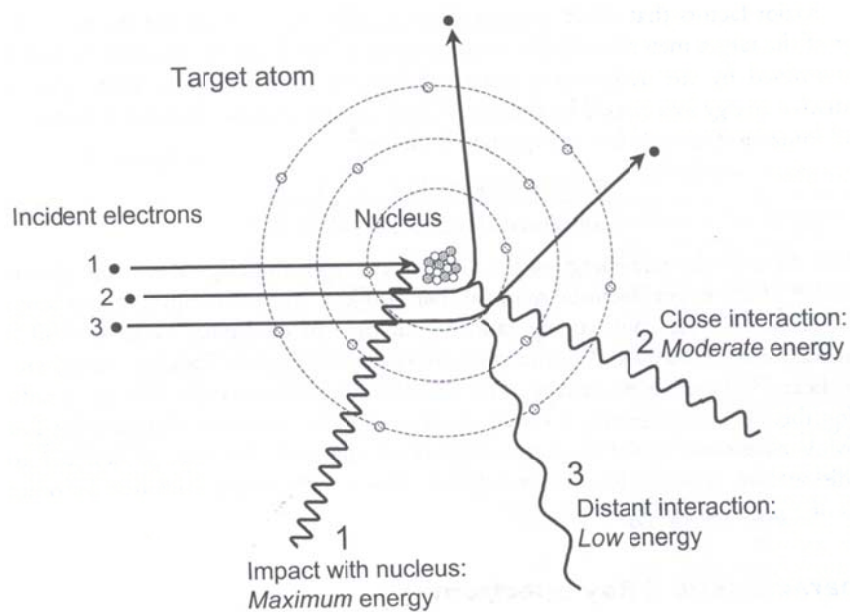


Figure 1-6 Bremsstrahlung radiation arises from energetic electron interactions with an atomic nucleus. In a close approach, the positive nucleus attracts the negative electron, causing deceleration and redirection, thus a loss of kinetic energy that is converted to an x-ray. (reproduced from [13])

Compared to Bremsstrahlung, the characteristic radiation only comprises a minor part of x-ray radiation. Characteristic radiation only occurs when a high-speed electron with energy higher than the binding energy of the target atom collides with one of the inner shell electrons and knocks out this inner electron, leaving a vacancy at this energy level. Then an electron in a higher energy state (outer shell) would move down to fill this vacancy, emitting an x-ray photon. These emitted x-ray photons have energies that are equal to the difference between the binding energies of the filled in electron and the electron that was knocked out. Since the binding energies of different shells are mainly determined by elements' fundamental properties such as the atomic structures, and could be calculated by modern quantum mechanics, this type of radiation is called characteristic radiation. Figure 1-7a depicts the detailed process of characteristic x-ray generation while Figure 1-7b shows a typical x-ray spectrum from tungsten target where the bremsstrahlung radiation base and the characteristic radiation sharp peaks. The ratio between characteristic x-rays and Bremsstrahlung x-rays would increase with the incident electron energies above the threshold energy for characteristic x-ray production. For instance, at 80kVp, characteristic x-ray production only comprises about 5% of the total x-ray output in a tungsten anode tube, whereas it increases to 10% at 100kVp[13].

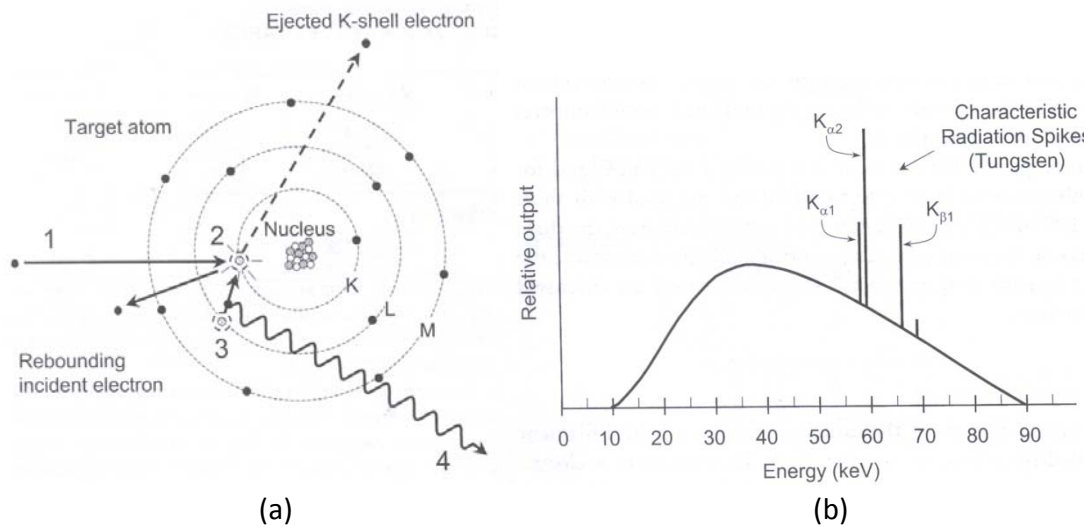


Figure 1-7 a. Generation of a characteristic x-ray in a target atom occurs as following (1) the incident electron interacts with the K-shell electron (2) the K-shell electron is removed (only if the energy of the incident electron is greater than the binding energy), leaving a vacancy in the K shell. (3) an electron from the adjacent L shell (or other higher energy level shells) fills the vacancy. (4) a K_{α} characteristic x-ray photon is emitted with an energy equal to the difference between the binding energies of the two shells. **b.** The filtered spectrum of bremsstrahlung and characteristic radiation from a tungsten target with 90kVp depicts specific characteristic radiation energies from K_{α} and K_{β} transitions. (reproduced from [13])

1-3 Interaction between x-ray and matter

When traversing matter, photons will penetrate, scatter or be absorbed. Interactions between x-ray photons and matter occur in different forms, depending on the incident energy of incoming radiation and physical properties of the matter. In diagnostic radiology and nuclear medicine, three types of interaction mainly play important roles: Coherent scattering, Compton scattering and photoelectric absorption. The remaining types of interactions such as pair production and photodisintegration only occur with high energy photons in the order of MeV level which is beyond the diagnostic range.

The study of these interactions is essential for developing thorough understanding of how medical images are formed and how x-ray detectors work.

1-3-1 Coherent scattering

Coherent scattering mainly occurs with very low energy diagnostic x-rays, around 15 to 30 keV, as used in mammography. In this type of interaction, the incident photon interacts with the entire atom and the target atom's electron cloud immediately radiates this energy, emitting a photon of the same energy but in a slightly different direction, typically a forward direction that is very close to the trajectory of the incident photon as illustrated in Figure 1-8. The scattering angle generally increases along with the incident photon energy.

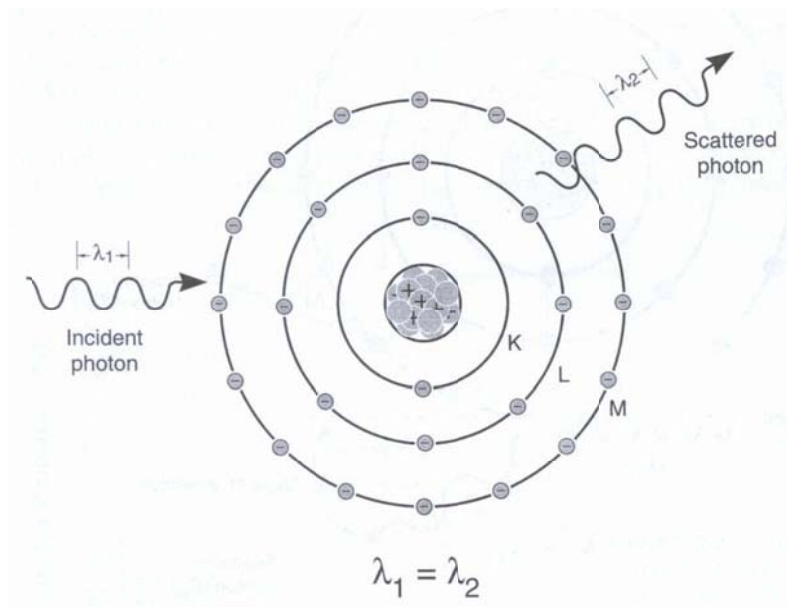


Figure 1-8 Coherent scattering process shows that the incident photon λ_1 interacts with the target atom and the scattered photon λ_2 is then emitted with almost the same energy merely towards a different direction. (reproduced from [13])

Detection of scattered photon is less desirable and essentially problematic for image quality, however this type of interaction generally has low occurrence probability in diagnostic range. Coherent scattering accounts for less than 5% of x-ray interactions with matter above 70keV and about 12% at most at 30keV.

1-3-2 Compton Scattering

Compton scattering occurs when only a portion of the incident photon's energy is absorbed and a photon is ejected with reduced energy. This interaction is most likely to occur between photons and outer shell electrons as depicted in Figure 1-9. The electron is ejected from the atom, and the photon is scattered with some reduction in energy. Compton scattering has ionization effect of the target atom and a division of the incident photon energy between the scattered photon and ejection electron. The increase of x-ray photons' wavelength when colliding with loosely bound electrons in matter was discovered by A.H. Compton in 1923, thus such interaction was named Compton scattering. [2]

With the increase of incident photon energy, both scattered photons and electrons are scattered more toward the forward direction. In x-ray transmission imaging, these photons are much more likely to be detected by the image receptor therefore worsening the image contrast. Moreover the ratio of scattered photons decreases with the increasing of incident photon energy at given scattering angle, thus with lower energy incident photons, for example x-rays used in diagnostic imaging (18 to 150 keV), most of the energy is then transferred to the scattering.

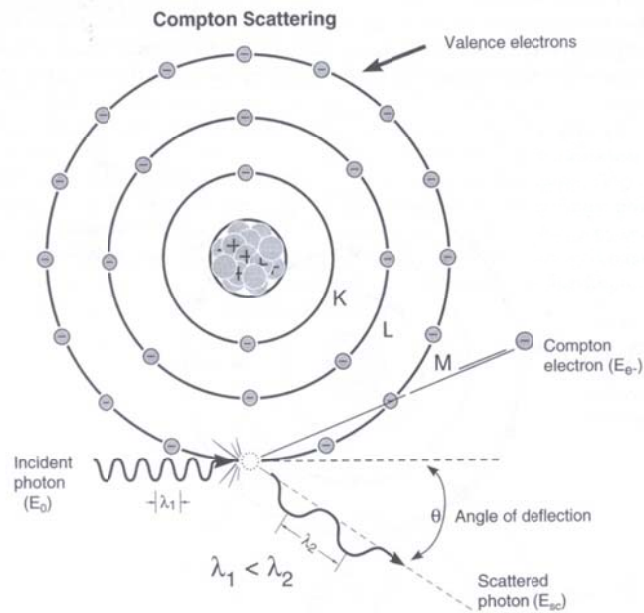


Figure 1-9 Compton scattering. The incident photon with energy E_0 interacts with a M shell electron that results in the emission of the Compton electron E_{e^-} as well as the Compton scattered photon E_{sc} at an angle θ . (reproduced from [13])

The incident photon energy needs to be substantially larger than the target electrons' binding energy for Compton scattering to take place, thus the probability of Compton scattering increases with the incident photon energy.

1-3-3 Photoelectric effect

Another important type of interaction generally observed in diagnostic imaging is called the photoelectric effect[2].

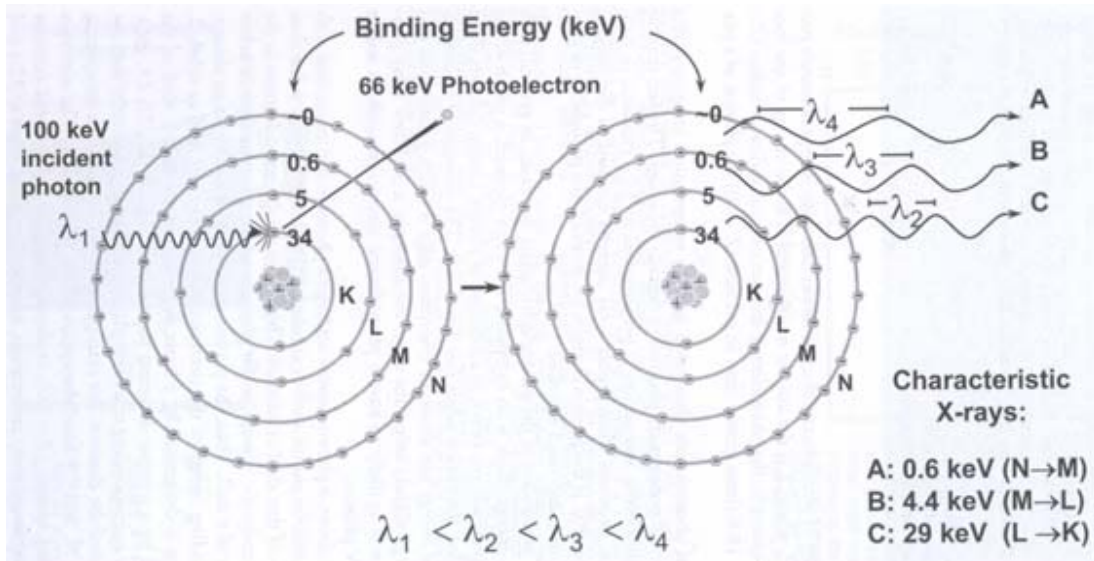


Figure 1-10 The photoelectric effect. Left diagram shows the photoelectric absorption between a 100 keV photon and an iodine atom. The K shell electron is ejected with a kinetic energy equal to the difference between incident photon energy and K shell binding energy. And the vacancy in the K-shell results in the transition of L-shell electron to K-shell, emitting K_{α} characteristic x-ray with energy equal to the difference in binding energies. Furthermore the electron cascade will continue to emit other characteristic x-rays in lower energy. The sum of all these characteristic x-ray energies equal to the binding energy of the ejected photoelectron. (reproduced from [13])

Figure 1-10 illustrated the detail process of photoelectric effect in which all of the incident photon energy is transferred to an electron ejected from the atom. In this case, the energy of the incident photon interacting with the electron must exceed the value of its binding energy E_b . A portion of the energy is lost during the process of overcoming the binding energy of the electron to its atom, while the rest becomes the kinetic energy of the outcome photoelectron.

$$hf_{in} = E_b + KE_e \quad \text{Equation 1-1}$$

The probability of photoelectric interaction per unit mass is approximately proportional to Z^3/E^3 , where Z is the atomic number and E is the energy of the incident photon [14]. Therefore in diagnostic imaging, most interactions between x-ray photons and bones as well as the image receptor are photoelectric effect, while the interaction with soft tissue is mostly Compton scattering.

Unlike Compton interaction, the event of photoelectric effect has some benefits for transmission type of x-ray imaging since there would be no additional non-primary photons to degrade the image quality.

1-4 Attenuation of x-ray

The loss of photons during x-ray beam passing through matter is called attenuation as illustrated in Figure 1-11. As discussed previously, attenuation is caused by both absorption and scattering interactions between incident photons and matter. At low incident photon energy, normally less than 26 keV, photoelectric absorption dominates the attenuation process; while Compton scattering generally is dominant in attenuation with higher energy incident photons interacting with high Z (atomic number) material.

For a monochromatic x-ray beam, the removal of the radiation per unit thickness of material is called the linear attenuation coefficient (μ). Then the number of photons lost Δn during traversing thickness Δx could be expressed as:

$$\Delta n = -\mu \cdot n \cdot \Delta x \quad \text{Equation 1-2}$$

After integration, the expression becomes:

$$I = I_0 e^{-\mu x} \quad \text{Equation 1-3}$$

in which I is x-ray photon number n transmitted through the material, and I_0 is the number of incident photons. The linear attenuation coefficient is generally a function of photon energy, atomic number, material and electron density.[15]

In diagnostic imaging range, photoelectric effect and Compton scattering are the two major contributing interactions. Thus the linear attenuation coefficient could be expressed as the linear sum of two fractions resulted from these two different interactions:

$$\mu = \mu_s + \mu_a = \mu_{\text{compton}} + \mu_{\text{photoelectric}} \quad \text{Equation 1-4}$$

Both μ_{compton} and $\mu_{\text{photoelectric}}$ are related to the material density and photon energy:

$$\mu_{\text{photoelectric}} = \rho \cdot Z^3 \cdot E^{-3} \quad \text{Equation 1-5}$$

$$\mu_{\text{Compton}} = \rho \cdot \rho_e \cdot E^{-1} \quad \text{Equation 1-6}$$

where ρ is the density, Z is the atomic number, E is the photon energy and ρ_e is the electron density of the material.

As the linear attenuation coefficient μ is proportional to the material density, it's more convenient to define μ/ρ , mass absorption coefficient, which then apparently is a constant of the material, and independent of its physical state.

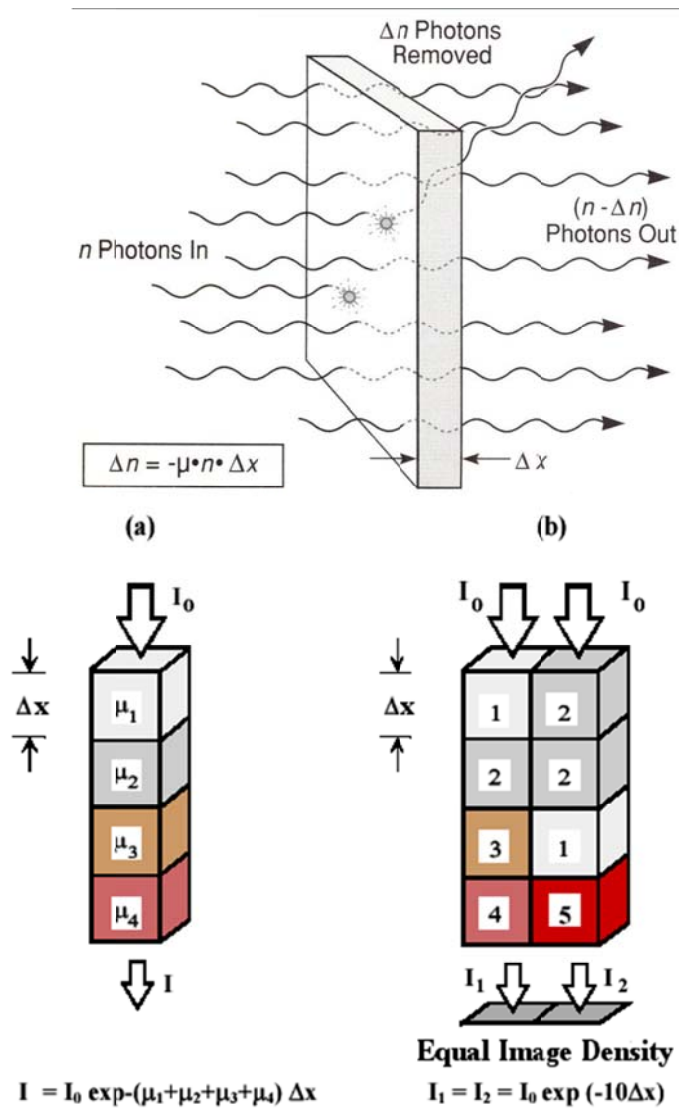


Figure 1-11 Diagram of attenuation resulted from x-ray photons traversing matter with certain thickness. The absorbed and scattered photons, Δn , are proportional to n and Δx . [14]

The model used above is for a material with a single element. Sometimes it is useful to know the mass absorption coefficient of a substance containing more than one element. In that case, the mass absorption coefficient is simply the weighted average of the mass absorption coefficients of its constituent elements. If we assume $w_1, w_2,$ etc. are the mass fractions of elements 1, 2, etc., in the substance and $(\mu/\rho)_1, (\mu/\rho)_2,$ etc., their mass absorption coefficients, then the mass absorption coefficient of the substance is given by [10]

$$\frac{\mu}{\rho} = \sum_{i=1}^n w_i \left(\frac{\mu}{\rho} \right)_i \quad \text{Equation 1-7}$$

It is important to remember that all the above derivations are based on the assumption of a monochromatic incident x-ray beam where in real applications, polychromatic x-ray are generally used where x-ray photons with different energies co-exist in the x-ray beam. The attenuation coefficient depends on the incident photon energy, and decreases as the energy increases. As a result, when a heterogeneous x-ray beam passes through material, low energy photons are preferentially absorbed leaving the transmitted x-ray with more high energy photons. This is so-called “beam hardening” effect as illustrated in Figure 1-12. Low energy (soft) x-ray will not penetrate most tissue in the body; therefore their removal will actually reduce the patient dose while keeping the diagnostic quality.

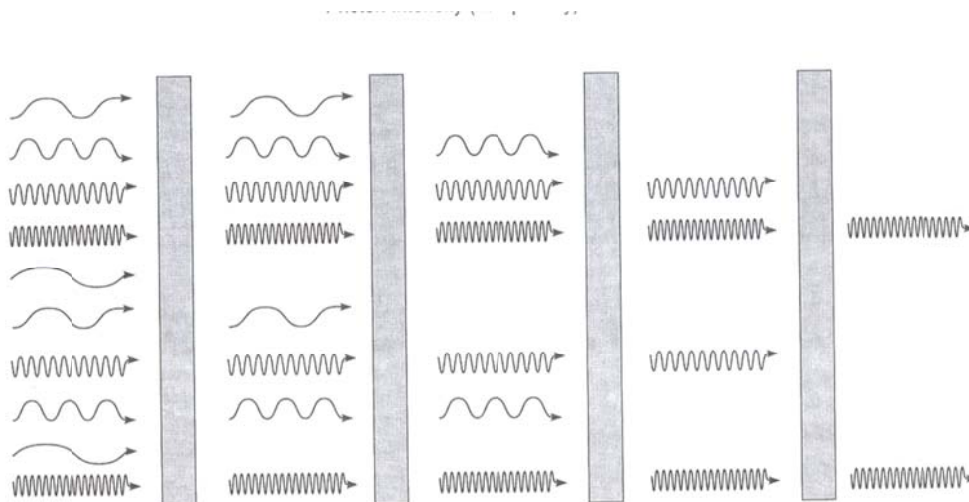


Figure 1-12 Polyenergetic x-ray beam “hardens” resulted from lower energy photons being absorbed as they traverse matter. (reproduced from [13])

1-5 X-ray source technology

As discussed previously, x-rays are produced when highly energetic particles interact with matter and convert the incident kinetic energy into electromagnetic radiation.[13] A device that can accomplish this task generally comprises two main components: A source of charged particles and an external energy source to accelerate them.[16] There are various means of electron generation and acceleration. The most widely adopted method started to be used with the first man-made x-ray tube by Röntgen. X-ray radiation was generated by applying high voltage across a cathode ray tube in Röntgen’s experiment. And until the present day, this is still the fundamental technology of modern x-ray tubes. With the development technology, there have been some alternative means for x-ray generation such as synchrotron x-ray, cold-cathode

field emission x-ray et al; however, the conventional x-ray tube technology still dominates the market.

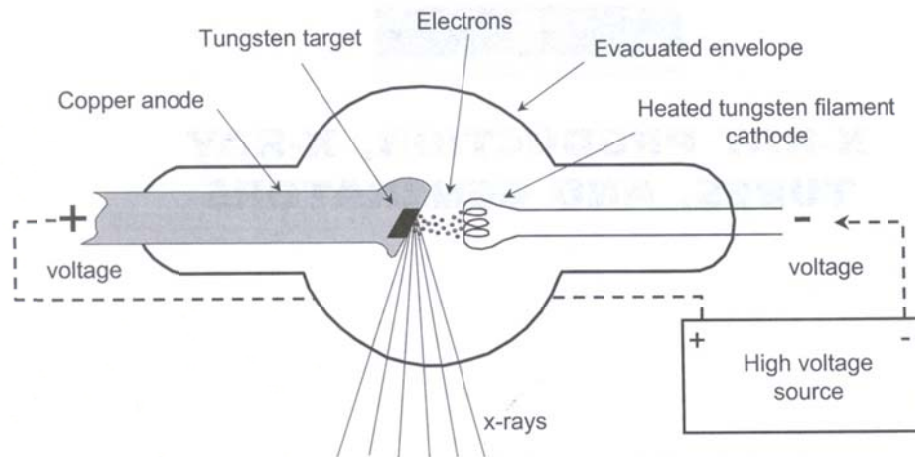


Figure 1-13 Schematics of a stationary anode x-ray tube. (reproduced from [13])

1-5-1 Conventional x-ray tube

The conventional x-ray tube has been widely used as an x-ray radiation generation apparatus for a lot of applications. As depicted in Figure 1-13, the major components in an x-ray tube are cathode, anode, and the vacuum envelope.

The source of electrons is the cathode, which generally is a helical filament of tungsten wire surrounded by a focusing cup, which is electrically connected to the filament circuitry and shapes the electron beam later on. The filament circuit would provide a small voltage (around 10v) to the filament, generating a current which then heats up the filament to as high as 1000°C and releases the electrons through

thermionic emission. Electrons then get accelerated through the vacuum within x-ray tube by the high electric potential applied between anode and cathode and eventually bombard the anode material.

The anode is a metal target electrode normally with high positive potential with respect to the cathode. Electrons striking the anode deposit most of their kinetic energy as heat, with a small fraction emitted as x-rays. For the strength of the electromagnetic interaction between an incoming electron and the nucleus is proportional to the charge of the nucleus, the efficiency should be proportional to the atomic number Z of the anode material[14]. The empirical result is expressed as:

$$\text{efficiency} = 10^{-6} Z \cdot kVp \quad \text{Equation 1-8}$$

This relation can also be calculated by quantum mechanics. This is one important reason why most commercial x-ray tubes use tungsten or other high Z value materials as anodes. The large amount of heat is one of the challenges in designing high power x-ray tubes.

As we see in Figure 1-16, an x-ray beam's intensity is not uniform throughout its entirety. As x-ray radiation is emitted from the target area in a conical shape isotropically, photons directed toward the anode side of the field would transit a greater thickness of the anode thus experience more attenuation than those directed toward the cathode side of the field. Measurements have determined that the intensity in the direction of the anode is lower than the intensity in the direction of the cathode.

The fact that the intensities vary in such a manner causes visible differences in the density produced on the radiographs. This phenomenon is called heel effect and is illustrated below.

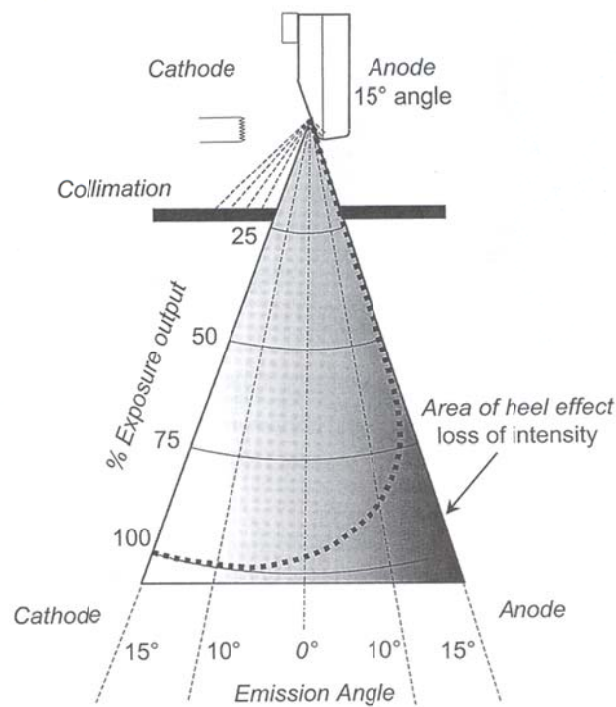


Figure 1-14 Illustration of anode heel effect. (reproduced from [13])

Due to the anode heel effect, it is obvious that a thick target perpendicular to the electron beam would absorb most of the x-ray photons. Therefore in x-ray tube designing, anode normally has a tilting angle. The anode angle is defined as the angle of the target surface with respect to the central ray in the x-ray field, ranging normally from 7 to 20 degrees, with 12-15 degrees being most common. This tilting angle primarily determines the effective focal spot size of the x-ray beam striking on the anode.

Focal spot size is defined in two ways. Actual focal spot size is the area on the anode that is bombarded by the incident electrons and is mainly determined by the cathode length. On the other hand, the effective focal spot size is the length and width of the focal spot as projected down the central ray in the x-ray field. The effective focal spot width is equal to the actual focal spot size width; while the length of the effective focal spot is smaller than the actual focal spot length by a factor of $\sin \theta$, θ being the anode tilting angle. This foreshortening of the focal spot length is called the line focus principle, depicted in Figure 1-15.

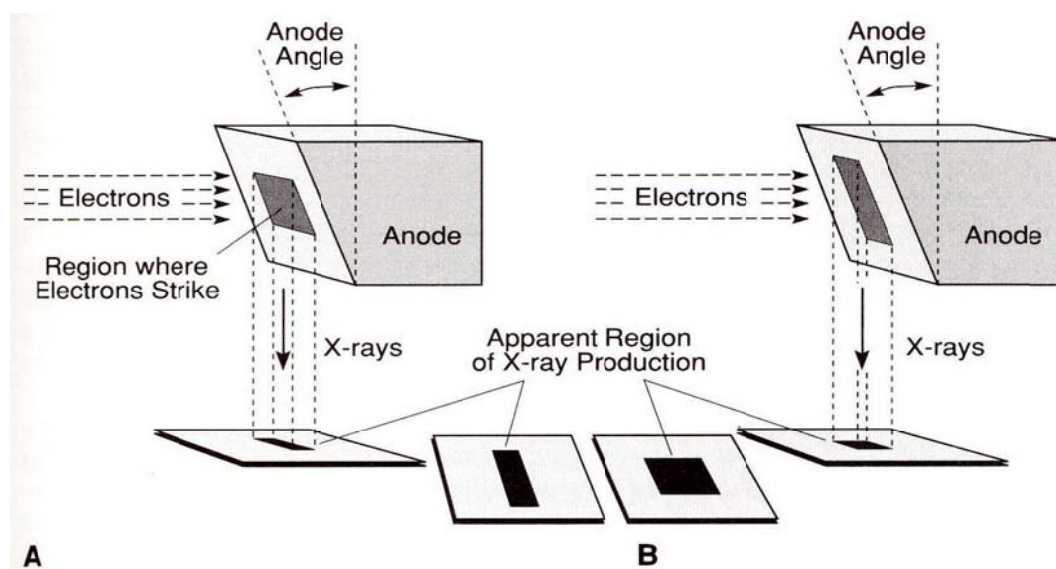


Figure 1-15 the illustration of line focus principle. (a) a square (isotropic) cathode source would produce rectangular effective focal spot after projection. (b) a rectangular electron source could be used to produce an isotropic (square) effective focal spot.[14]

Both the heel effect and the line focus principle are very important in the anode design, as anode with smaller tilting angle with respect to the electron beam would

absorb most of the x-ray photons; while large tilt angle gives bigger effective focal spot size.

1-5-2 Synchrotron X-ray Source

With the development of high energy physics, a new type of x-ray source, synchrotron x-ray, became available. The invention of synchrotron x-ray sources represent an immense leap in performance over conventional x-ray sources [17]. As discussed early in this chapter, when charged particles experiences deceleration or acceleration (either moving in a circle or straight line), x-ray radiation is generated. As illustrated in Figure 1-16, if the speed of charged particles is close to the speed of light, the emitted radiation is confined in a small angle[18].

Compared to a traditional x-ray source, a synchrotron x-ray source has many advantages[17, 19]:

- Super high flux: about hundreds of thousands times higher than conventional x-ray tubes. High spatial resolution: can be as small as sub-micron meter or even nano meter compared with tens and hundreds of micron meter resolution with conventional x-ray source.
- Pulsed x-ray radiation: Essentially desirable patterns of x-ray waveform could be generated.
- Wide energy range of generated radiation: the radiation covers a wide range of energy.

- Capability of monochromatic x-ray generation: when used with monochromator, the output x-ray can be confined in a small range around desired energy. This is very useful in x-ray imaging introduced later on.

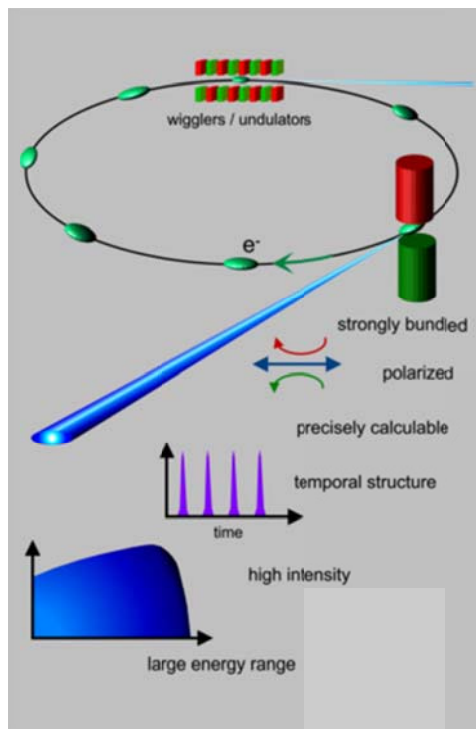


Figure 1-16. Schematics of generation of synchrotron x-ray radiation and its properties.
http://www.bessy.de/guided_tour/en.02.sr.php?docs=2

The advent of synchrotron radiation has opened up comprehensive opportunities for science and technology[20]. The invention of synchrotron x-ray sources represent an immense leap in performance over conventional x-ray sources [17]. However, the generation of synchrotron x-rays needs a high energy physics facility to accelerate the electrons, which obviously is a time-consuming and expensive project. There are only less than 100 such facilities all over the world. Therefore, the application

of synchrotron x-ray is much more restricted than other counterparts, despite all the great properties synchrotron x-ray beam have.

1-6 X-ray Source Based on CNT

X-ray technology has evolved during the past century, with better engineering and much more dedicated electronics. However the way to generate x-ray has not changed much, electrons from a heated filament striking a high voltage target. Such type of electron generation is called thermionic emission. Conventional x-ray sources with thermionic electron source have been widely used in different applications. However, it has some natural disadvantages that need alternative solution, such as heat generation, large device size and slow response time. An electric driven field emission mechanism has been investigated as x-ray source for quite some time. Field emission is a “cold cathode” technology with much less heat generation, but pioneers had difficulties in fabricating and maintaining field emitter material until the emerging of CNT field emission material. X-ray source based on CNT field emission has been done in our group. The novel x-ray source has sub-micro-second temporal resolution and can provide excellent flexibility in scaling. Several imaging systems using it have been built. In the next several chapters, I will introduce my research on the x-ray source based on CNT and the imaging systems.

References

1. H. H. Seliger, *Wilhelm Conrad Rontgen and the Glimmer of Light*. Physics Today, 1995: p. 25-31.
2. K. K. Shung, Michael B. Smith, and B. Tsui, *Principles of Medical Imaging*. 1992, San Diego: California: Academic Press, Inc.
3. D.J. Helfand, *X-rays from the rest of the universe*. Physics Today, 1995. **11**: p. 58-64.
4. L.V. Azaroff, *Elements of X-Ray Crystallography*. 1968, New York: McGraw-Hill.
5. B.D. Cullity, *Elements of x-ray diffraction*. 1978: Addison-Wesley Publishing Company, Inc.
6. J. Als-Nielsen and G. Materlik, *Recent applications of x-rays in condensed matter physics*. Physics Today, 1995. **11**: p. 34-40.
7. W.A.Hendrickson, *X-rays in molecular biophysics*. Physics Today, 1995. **11**: p. 42-48.
8. W.R. Hendee, *X-rays in medicine*. Physics Today, 1995. **11**: p. 51.
9. W.R. Hendee, *Medical radiation physics*. Second ed. 1979, Chicago, London: Year Book Medical Publishers, Inc.
10. W.R. Hendee and E.R. Ritenour, *Medical Imaging Physics*. 4th ed. 2002, New York: Wiley-Liss.
11. E Seeram, *X-ray imaging equipment*. 1985: Charles C Thomas.
12. S.C. Bushong, *Radiologic Science for Technologist*. 1997: Mosby.
13. Bushberg, J.T., *The essential physics of medical imaging*. 2nd ed. 2002, Philadelphia: Lippincott Williams & Wilkins. xvi, 933 p.
14. Wolbarst, A.B., *Physics of Radiology*. 1993.

15. R. Wilks, *Principles of Radiological Physics*. 1981, Churchill Livingstone, Edinburgh, U.K., and New York.
16. E. Seeram, *X-ray imaging equipment*. 1985: Charles C Thomas.
17. G. Margaritondo, *Introduction to Synchrotron Radiation*. 1988: Oxford University Press.
18. Jackson, J.D., *Classical Electrodynamics*. 3rd ed. 1998.
19. R. Garrett, *An introduction to synchrotron radiation*. 2004.
20. R. Lewis, *Medical applications of synchrotron radiation x-rays*. *Phys. Med. Biol.*, 1997. **42**: p. 1213-1243.

Chapter 2 Carbon Nanotube Field Emission and its application

Innovation of new materials with novel properties provides the driving force for technology development. The development of material science has extended our viewpoint from macroscopic to small nanometer scale dimensions. Material in nm scale dimension inherit some of the most remarkable and unique physical and chemical characteristics. Among all those investigations for nanomaterials, carbon nanotube (CNT) related research has been booming for the past two decades.

Carbon, as the most versatile element in the periodic table, is one of the elements people have been using and studying for a long time. Interestingly, the investigation of carbon nanotubes only started about 20 years ago when it was first discovered by Iijima.

For its ideal 1-D nanostructure, the carbon nanotube provides a perfect physical model to investigate the fundamental science at the nanometer scale. Researchers from various areas have been dedicated into understanding its unique physical and chemical properties and using it in different applications. This field is progressing at staggering rates with thousands of publications appearing in literature every year. Focus of this chapter here would be the development and characterization of CNT field emission cathodes, which play a critical role in CNT-based field emission x-ray source.

2-1 Fundamentals of Carbon Nanotube (CNT)

2-1-1 History of the discovery of carbon nanotube

Tubular carbon nanostructures were first observed as early as 1952 by Soviet scientists Radushkevich and Lukyanovich[1]. A paper by Oberlin, Endo and Koyama in 1976[2] clearly showed carbon fibers with nm-scale diameter using a vapor-growth technique. In 1979, John Abrahamson presented evidence of carbon nanotube at the 14th Biennial Conference of Carbon, describing carbon nanotube as carbon fibers formed on carbon anodes during arc discharge[3]. Furthermore, in 1981 another group of Soviet scientists published some results of chemical and structural characterization of carbon nanoparticles produced by a thermocatalytical disproportionation of carbon monoxide, suggesting that carbon multi-layer tubular crystals were formed by rolling graphene layers into cylinders[4]. In 1985, as illustrated in Figure 2-1a, fullerenes were discovered by Rick Smalley and coworkers at Rice University[5], and then in 1990 Smalley proposed the existence of a tubular fullerene[6]. However, it was not until almost 40 years after the discovery of first carbon tubular nanostructure, when Sumio Iijima reported of the accidental observation of carbon nanotubes in the journal of Nature in 1991[7] that created a world-wide interest and excitement, resulting in the development of nanotube field at present. Figure 2-1b shows the very first TEM images of multiwall nanotube discovered by Iijima. Although carbon nanotubes were observed four decades ago, it was not until the discovery of C₆₀ and theoretical studies of possible other

fullerene structures that the scientific community realized their importance. Ever since this pioneering work, investigation of the carbon nanotube has developed into a leading area in nanotechnology, expanding at extremely fast pace. Only 9 papers containing the word “carbon nanotube” were published in 1992, and over 5000 publications were printed in 2004. All these interests in this new form of carbon material were triggered by its unique properties and numerous potential applications.

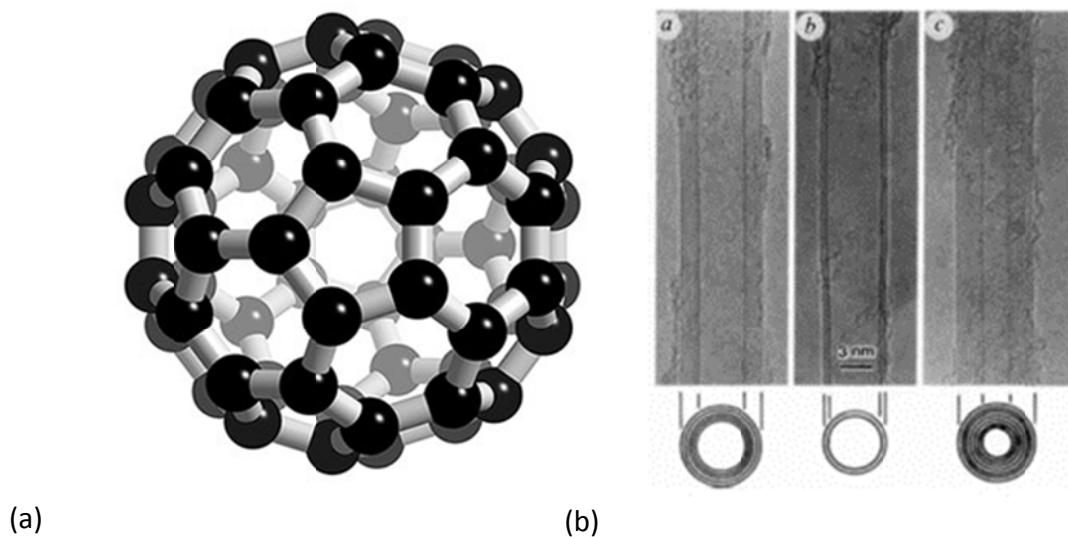


Figure 2-1 a. The structure of C_{60}
b. The very first high-definition TEM image of multiwall carbon nanotube[7]

2-1-2 The Structure of CNT

Basically there are two types of carbon nanotube, single wall (SWNT) and multiwall (MWNT). A SWNT could be seen as a rolled up single graphene sheet despite the fact that the growth mechanism does not suggest it is actually formed in this way. On the other hand, a MWNT is essentially formed by multiple concentric SWNTs. In

order to describe such fundamental characteristics, we introduce two vectors, C_h and T , whose rectangle defines the unit cell as illustrated in Figure 2-2(a). C_h is the vector that defines the circumference on the surface of the tube connecting two equivalent carbon atoms, then a carbon nanotube can be defined by the chiral vector:

$$C_h = n\hat{a}_1 + m\hat{a}_2 \quad \text{Equation 2-1}$$

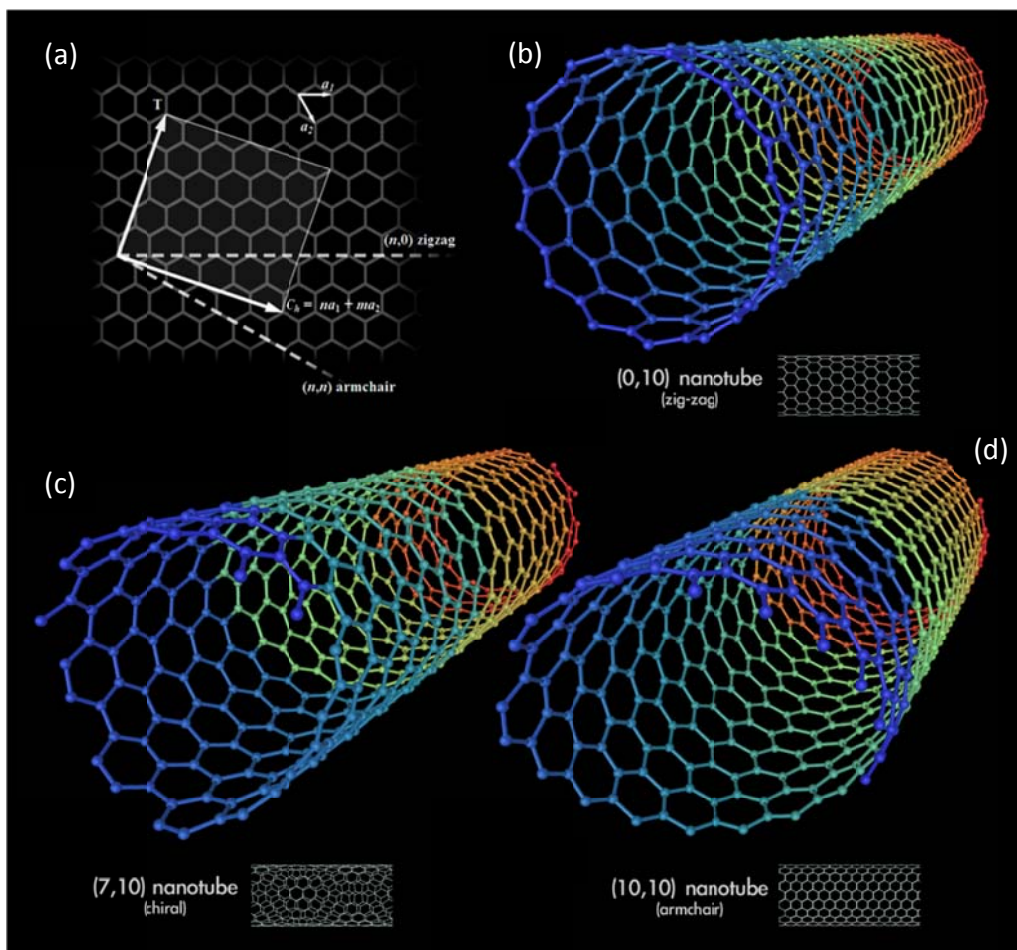


Figure 2-2 (a) The graphene sheet labeled with integers (n, m), which could determine the diameter, chiral angle and type of the nanotube. (b), (c) and (d) are schematics for zigzag, chiral and armchair nanotube respectively[8]

The \hat{a}_1 and \hat{a}_2 compose the chiral vector along with a pair of index (n,m) which denotes the number of unit vectors \hat{a}_1 and \hat{a}_2 respectively .

From Figure 2-2, we noticed that the chiral angle ϑ is defined by the chiral vector and the \hat{a}_1 direction (also known as zigzag direction). The chiral angle is also determined by the indexes n and m:

$$\theta = \tan^{-1} \left[\sqrt{3}m / (m + 2n) \right] \quad \text{Equation 2-2}$$

The chiral angle is used to categorized carbon nanotubes into three different classes differentiated by their electronic properties: the zigzag and armchair nanotubes correspond to $\vartheta=0^\circ$ and $\vartheta=30^\circ$, respectively, where $n=m$. All other nanotubes ($0^\circ < \vartheta < 30^\circ$) are called chiral tubes.

The nanotube diameter can be given in terms of the indices (n, m):

$$d_t = C_h / \pi = \sqrt{3}a_{c-c} (m^2 + mn + n^2)^{1/2} / \pi \quad \text{Equation 2-3}$$

where a_{c-c} is the C-C bond length (1.421Å for graphite sheet). It's obvious that a nanotube can be specified by either the (n, m) indices or d_t and ϑ equivalently.

2-1-3 Properties of CNT

With knowledge of the structure of carbon nanotube, it's easier to understand the unique physical and chemical properties that CNT exhibits.

As CNT can grow from their base or tip continually, with sufficient carbon source and energy they can essentially be fabricated over great length while maintaining the nm-scale tubular structure. Therefore CNT has natural sharp-tip geometry, with aspect ratio of 100:1 or greater.

It has been proved that CNT could be either metal or semiconductors with different energy gaps, depending sensitively on the diameter and helicity of the tubes [9-12]. As discussed previously in the structure of CNT, the chiral angle or indices (n,m) is used to separate CNTs into three classes differentiated by their electronic properties: armchair, zigzag and chiral. Armchair CNTs are metallic; while zigzag and chiral nanotubes can be semiconductors with $n-m=3j$, where j is a nonzero integer, are very tiny-gap semiconductors; and all others $(n-m=3j\pm 1)$ are large-gap semiconductors. MWNTs may have different electronic properties from shell to shell. This unique property of CNT has triggered great interest in the use of CNT in microelectronics applications. Multiple investigations have been done to measure the electrical conductivity of CNTs, suggesting some of the isolated MWNTs exhibit current densities over 10^6 A/cm². [8, 13]

Carbon nanotubes also have exceptional mechanical properties due to the fact that C-C bond is one of the strongest bonds in nature. Because of their flexibility, CNTs can be bent repeatedly up to 90° without breaking or damaging. It has been demonstrated that carbon nanotubes can have large Young's modulus up to 1.8 TPa [14] [15, 16], compared to the 0.2 TPa modules for both Kevlar and stainless steel. The high

aspect ratio, exceptional mechanical properties, tensile strength and low density of CNTs make it a promising new material for strengthening of fibers in extremely strong composite materials.

In addition to above mentioned properties, CNTs also showed extremely good thermal conductivity of as high as $3000\text{ W}/(\text{m K})$ [17] compared to the range of around $300\text{--}400\text{ W}/(\text{m K})$ of metals such as gold and copper, known to be good thermal conductors. At temperatures above 1000°C and below room temperature, the linear dependence of specific heat and thermal conductivity has been reported [18].

2-2 Applications of CNTs in field emission

With extraordinary mechanical properties, unique electrical properties along with chemical and thermal stability make CNTs suitable for many applications [19]. Some of the applications are shown in Figure 2-3.

The ability of CNT-equipped AFM and SPM tips to detect sub-nanometer feature and deep trenches is enabled by the small tip diameter, large aspect ratio, and large tensile strength. Also the strong mechanical properties of CNT make it a great reinforcement material in high-performance composite and fabrics. Its hollow tubular structure has drawn great interest in using it as drug delivery carrier material in the nano-medicine area.

With its electronic properties, semiconductor nanotubes can be used for metal-semiconductor (Schottky) diodes, PN junction diodes, and field-effect transistors (FETs), whereas metal nanotubes can be used for single-electron tunneling transistors. Another potential application where CNT's electronic properties were utilized is conducting plastic and polymer composite material.

Other potential applications of CNT include catalyst support and adsorbents, energy storage and biosensor and chemical sensor et al.

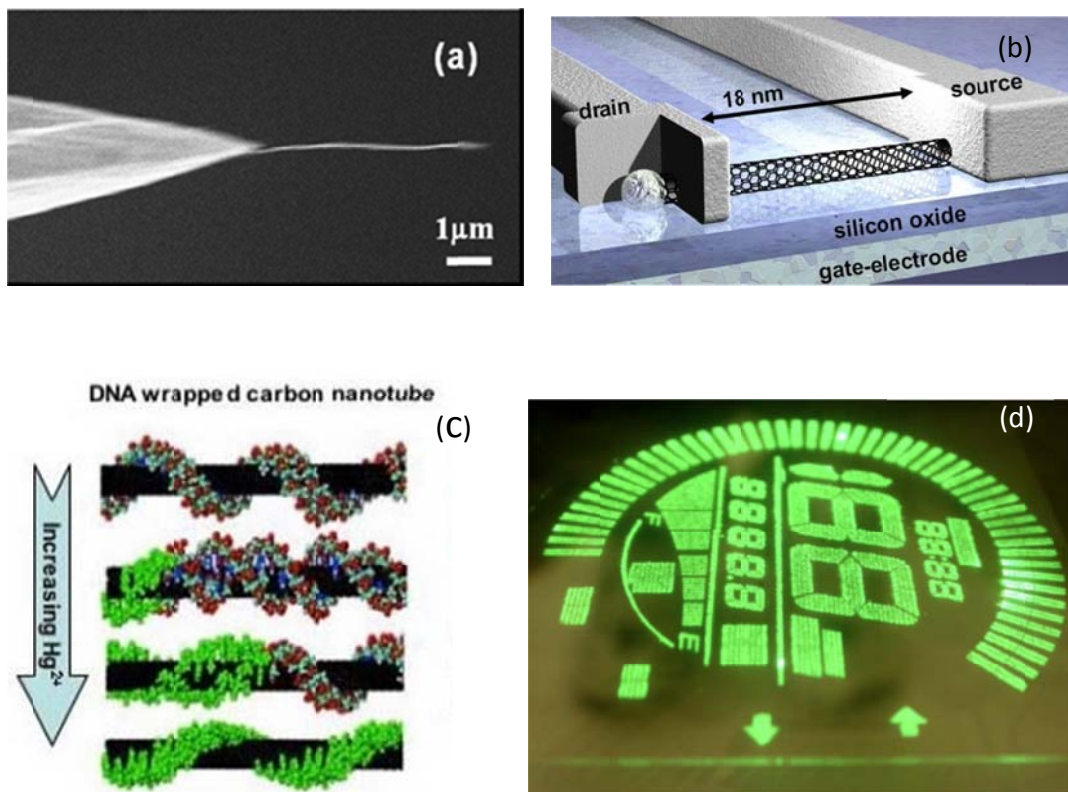


Figure 2-3. Applications based on CNTs. (a): AFM tip equipped with CNT. (b): Infineon Technologies designed this carbon nanotube transistor, and it is one of the smallest ever made. (c) DNA wrapped SWNT used as biosensor in living cells.[20] (d): Field emission display based on CNT (courtesy of Xintek Inc.).

In our research group, we mainly focus on one of the most fascinating applications with CNT, field emission devices, which would be elaborated later in this chapter. The large aspect ratio and unique electrical properties make CNTs the ideal field emitters. Potential applications include vacuum microelectronics, microwave amplifiers, field emission displays, and x-ray tubes.

2-2-1 Thermionic emission

Electrons can be emitted from metallic and semiconducting materials. At very low temperature, most of the electrons reside at energy level lower than the Fermi energy, E_f . Electrons are bounded inside the material because of the surface energy barrier, also known as the work function ϕ , and could only escape to an unbound state referred to as the vacuum level showed in Figure 2-4. There are two main processes [21] for bound electrons to gain extra energy and escape to the vacuum level, either by increasing the temperature to provide extra thermal energy for the electrons to overcome the energy barrier, in this case, we call it thermionic emission; or supplying a strong enough external electric field so that electrons could tunnel through the energy barrier and form field emission. It is also possible for electrons to escape from material and overcome the surface energy barrier given sufficient temperature and external field.

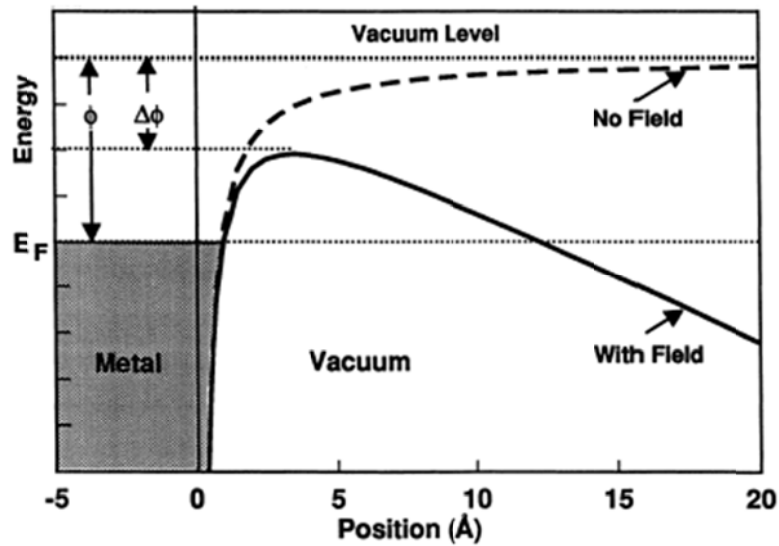


Figure 2-4 Potential energy for an electron in the vicinity of a metal surface with/without applied field. The dashed line shows the energy barrier that an electron must overcome to escape to the vacuum level without external field, while the solid lines shows the reduction of energy barrier both in height and width with an external field applied. [21]

Thermionic emission can be described by Richardson-Dushman equation [22] as shown as:

$$J = \frac{4\pi m e k_B^2}{h^3} T^2 \exp\left(-\frac{\phi}{k_B T}\right) = A_0 T^2 \exp\left(-\frac{\phi}{k_B T}\right) \quad \text{Equation 2-4}$$

where T is the temperature and ϕ is the work function. From the equation, we can tell that $\log(J/T^2)$ has a linear relationship with respect to $1/T$ with negative slope being the work function ϕ .

For thermionic emission, the emission current output increase with the temperature of the cathode material. Being simple in fundamental principle, thermionic emission has been widely used as electron source in various areas such as x-ray tubes,

cathode-ray tubes and other electronic apparatus. However, the same emission principle brings in some natural disadvantages especially when trying to use thermionic emission for extensive time. Over the time the cathode material might degrade due to oxidation or heat induced problems, generally thermionic electron sources require ultra-high vacuum operating environment and high-performance cooling apparatus, therefore difficult to make a compact device out of a thermionic source. Another problem associated with thermionic emission is the limit of switching speed due to the requirement of high temperature. Therefore, without additional electronic devices, thermionic electron source generally has slower response time.

Field emission, on the other hand, nicely fills some of the gaps in the applications that thermionic emission leaves and becomes an alternative electron generation mechanism.

2-2-2 Field emission

Field emission holds different mechanism than thermionic emission. As illustrated in Figure 2-4, with the presence of an external electric field, the surface energy barrier is reduced so that at a relatively short distance from the material surface the energy level in the vacuum is equal to the Fermi Level, with the energy level keeping decreasing as the distance from the surface increases. The amount of reduction can be expressed as:

$$\Delta\phi = \left(\frac{eE}{4\pi\epsilon_0} \right)^{1/2} \quad \text{Equation 2-5}$$

where e is the fundamental charge, E is the electric field strength and ϵ_0 is the permittivity of vacuum. Meanwhile, the width of energy barrier becomes finite therefore the electrons would be able to tunnel through.

The theoretic model built by Fowler and Nordheim[23-25] successfully gave a description of the electron emission with respect to the external field as:

$$J = \frac{e^3 E^2}{8\pi h \phi t^2(y)} \exp \left[\frac{-8\pi(2m)^{1/2} \phi^{3/2}}{3heE} v(y) \right] \quad \text{Equation 2-6}$$

where J is the emission current density $y = \Delta\phi/\phi$, h is the Planck's constant, m is the electron mass, and $t(y)$ and $v(y)$ are the Nordheim elliptic functions; to the first approximation $t^2(y) = 1.1$ and $v(y) = 0.95 - y^2$. Substituting these approximations in Equation 2-6, together with Equation 2-5 for y and values for the fundamental constants, it could be essentially rewritten as:

$$J = 1.42 \times 10^{-6} \frac{E^2}{\phi} \exp \left(\frac{10.4}{\phi^{1/2}} \right) \exp \left(\frac{-6.44 \times 10^7 \phi^{3/2}}{E} \right) \quad \text{Equation 2-7}$$

where J is in units of A/cm^2 , E is in units of V/cm^1 and ϕ in units of eV.

It has been reported that to achieve current densities of 10^2 - $10^3 \text{ A}/\text{cm}^2$, electric fields of 3 - $6 \times 10^7 \text{ V}/\text{cm}$ are needed[26] from flat surfaces, which is not practical in

experimental conditions. Therefore generally field emission only becomes feasible when there are protrusions with high curvature on the surface, and the local electric field on the tip is enhanced by several orders of magnitude. The local electric field F could be expressed as

$$F = \beta V / d \quad \text{Equation 2-8}$$

Where V is the electric potential applied to generate the electric field over a distance of d , and β is called the field enhancement factor, which can be as high as 1200[27], and in some cases over 10,000[28]. It can be easily proved that the sharper the tip, the larger the field enhancement factor, and the lower applied voltage required.

Combining the above equations, for a sharp tip emitter with emission area A , we can get total emission current:

$$I = JA = aV^2 \exp(-b\phi^{3/2} / V) \quad \text{Equation 2-9}$$

where the constants $a = 1.42 \times 10^{-6} A\beta^2 \exp(10.4 / \phi^{1/2}) / d^2 \phi$, $b = 6.44 \times 10^7 \phi^{3/2} d / \beta$

This is one of the most important equations in electron emission theory and has found many and varied applications. The plot $\ln(I/V^2)$ versus $1/V$ is a straight line and this curve is called Fowler-Nordheim (FN) plot. From this equation, we can clearly see that the emission current increases exponentially with the applied voltage. Also, given certain applied voltage, emitters with higher field enhancement factor β will have substantially better performance.

2-2-3 Carbon nanotube in field emission

Before carbon nanotube plays an important role in field emission, early pioneers have made much effort to fabricate field emitters feasible for various applications, such as Spindt-tip emitters [25] for field emission display (FED) [23, 25] and metal tip based x-ray tubes [29, 30] et al. However, those earlier attempts suffered two major drawbacks: low stability and short life-time. From the field emission theory, we know that work function and external field strength would determine the emission current. Work function is generally associated with the material's atomic structure and chemical properties, researchers have tried different materials, mostly metal and semiconductors for field emitters.

Spindt and colleagues attempted to evaporate metal (Molybdenum) into small apertures [25] to achieve high field enhancement rate, while others tried to etch silicon into sharp tips [21]. Figure 2-5 demonstrates the microfabrication procedure of a Spindt type metal tip field emitter along with the SEM image of the cross-section.

In spite of the some reasonable field emission results from those emitters, their sharp tip geometry as well as the work function were too vulnerable to heating, chemical reaction, material evaporation and ion bombardment [31]. As depicted in Figure 2-6, it's clear that the sharp tip of this essentially pyramid shape of Spindt-tip could easily be altered when arcing happened, which greatly reduced the field enhancement factor hence the field emission performance.

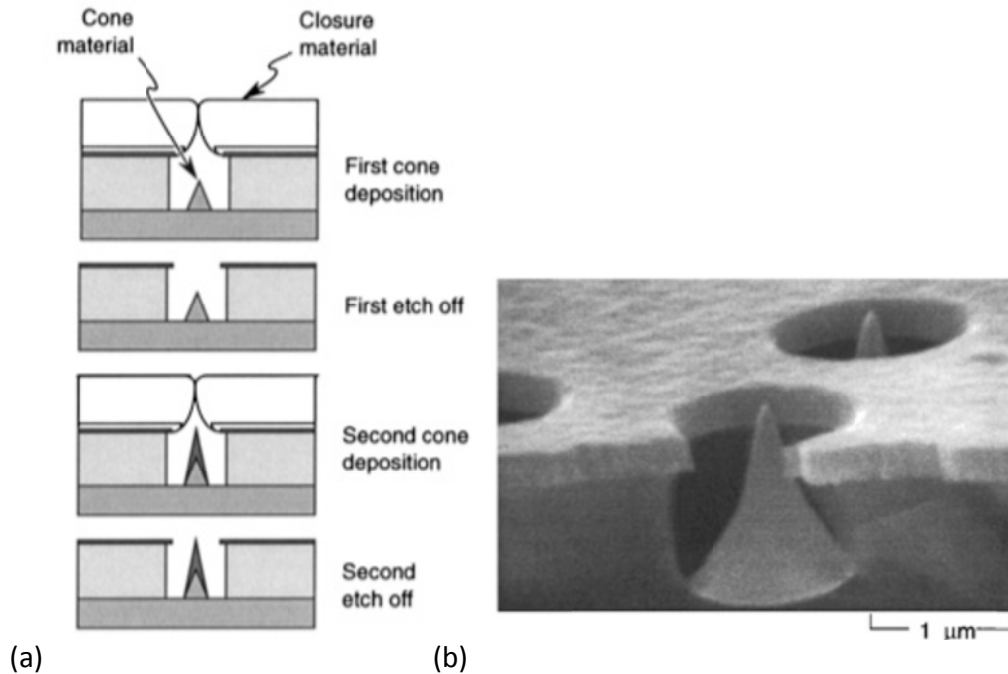


Figure 2-5 (a) Microfabrication procedure for a Spindt type metal tip (b) the SEM image of the cross section of a Spindt tip

With the discovery of the carbon nanotube, researchers realized that it was a great candidate for field emitters. It has atomically sharp tip with field enhancement factor much higher than any of those previous trials, thus even when arching or other reaction affected the original tip, it wouldn't reduce the field enhancement factor much as depicted in the right scheme of Figure 2-6. Meanwhile, with such high aspect ratio and field enhancement factor, CNTs require lower threshold electric field to emit, which reduce the high voltage associated arching and other problems. Comparison of different field emitters is shown in Error! Reference source not found.. Furthermore, CNTs are chemical and mechanically stable compared to other material.

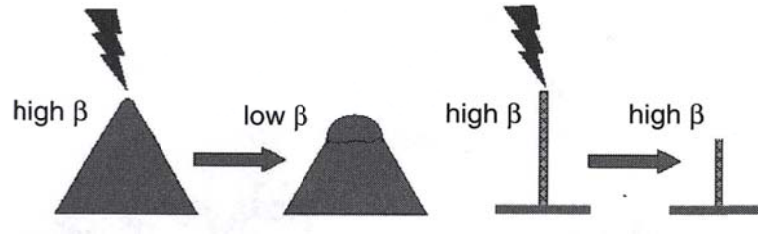


Figure 2-6 Schematics of arcing damage to Spindt-type emitters (left) and to CNT emitters (right) [19].

Cathode Material	Threshold Field (V/ μm) for 10 mA/cm ²
Mo tips	50-100
Si tips	50-100
p-type diamond	160
Defective CVD diamond	30-120
Amorphous diamond	20-40
Cesium-coated diamond	20-30
Graphite powders	10-20
Nano-diamond	3-5 (unstable > 30 mA/cm ²)
Carbon Nanotubes	1-2 (stable >4000mA/cm ²)

Table 2-1 Threshold field required for a 10 mA/cm² emission current density for common emitters. [32, 33]

As the emission current of a CNT field emitter is determined by the external field, the removal of applied voltage would instantly shut off the field emission. Therefore, CNT field emission sources are most valuable in applications require fast switching

speed as well as accurate timing control. A good example is x-ray generation, especially in the medical area where x-ray exposure to the patients' needs to be cautiously controlled. In x-ray medical imaging area, such as computed tomography, where x-rays needs to be fired at high speed and a certain pattern, CNT field emission source would definitely be desirable.

2-3 Fabrication of CNT field emission cathode

In order to fully utilize the excellent field emission properties of CNTs in various applications, it's necessary to find a way to integrate CNTs into devices and systems. Depending on different purposes, CNTs generally could be used as point electron source or area electron source. Point electron source normally contain only one or a few CNTs and could be used as electron gun in electron microscope; whereas area electron source on which a film with CNTs is deposited in a certain area. For applications requires higher emission current, such as x-ray tube and field emission display, area source is preferred. The concentration of my Ph.D. study is the application of CNT field emission source in medical imaging. In the following part the fabrication and application of the CNT area electron source will be discussed in more details.

2-3-1 Electrophoresis Deposition (EPD) of CNT electron source

There have been numerous methods of fabricating CNT area electron source such as spray deposition[34], self-assembly, [35, 36]screen printing[37] et al. In our group, the most commonly used technique is Electrophoresis Deposition (EPD) [38]for CNT area cathode fabrication. EPD is a high throughput and automated industrial process that has been widely used for coating particles [39]. This method is a liquid phase process utilizing the molecular polarizability of small particles in an electric field enabling efficient deposition of homogeneous CNT coatings on conducting substrates with fine control of the film thickness and morphology. As depicted in a metal surface and the substrate for CNT deposition is connected the opposite electrodes respectively. Both electrodes are immersed in the alcohol or water based CNT suspension with salt or other ion source additives as “charger”. With a DC electric field applied between the two electrodes, the “charger” particles facilitate CNTs selectively attached to the exposed area pre-defined to form a homogenous layer of coating. Salt and electrical polarity could be chosen to define the direction of CNT deposition, for example, if $MgCl_2$ is used as “charger”, then the CNTs would migrate to the negative electrode, whereas NaOH would facilitate the CNTs to move towards positive electrode. Normally, a layer of glass was pre-deposited before the CNT layer to help the adhesion between CNTs and the target substrate.

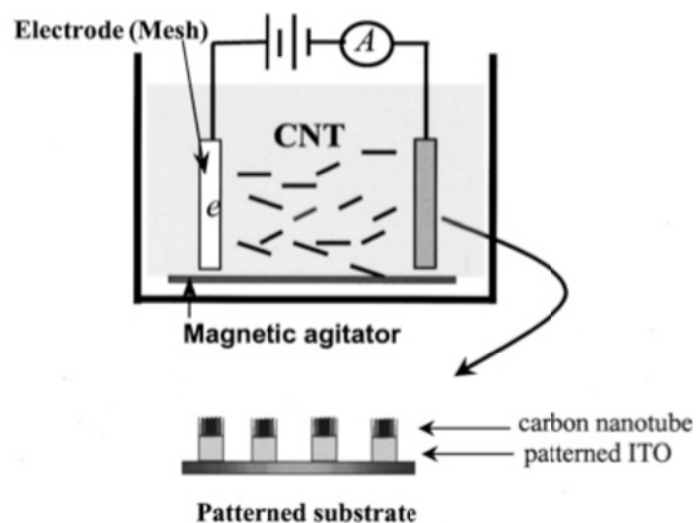


Figure 2-7 Schematic diagram of EPD set-up. CNTs are attracted to the negative electrode and bond to the conducting parts of the substrate and form a pre-defined area coating. [40]

2-3-2 Fabrication of CNT cathode

In order to help the adhesion of CNT coating and the substrate, a glass layer is deposited first, then the CNT layer. In our experiment, a commercial glass powder SCB-13 is used to facilitate the CNT adhesion

The suspension for glass and CNT deposition are made by following the recipes, respectively:

Glass: Fe : MgCl_2 : ethanol : H_2O = 400mg : 120mg : 12mg : 400ml : 10ml

CNT: ethanol : H_2O : MgCl_2 = 10mg : 400ml : 8ml : 5mg

Before the EPD process, the suspension is sonicated for 5min to disperse the precipitated particles. The Mg^{2+} chargers will bundle with glass particles or the CNTs

after sonication. As depicted in Figure 2-7, a metal surface and the target substrate are connected to the positive and negative electrode of the power supply respectively, while being immersed in the suspension. Only a pre-defined area on the target substrate is exposed and in contact with the suspension, therefore the pattern and shape of CNT film could be easily controlled. With the help of the DC electric field between two electrodes, the Mg^{2+} chargers which have been bundled with the particles (glass or CNTs) in the suspension already would carry the particles to move towards the deposition sites. After electrophoresis deposition, the cathodes are further annealed at around $500^{\circ}C$ in 10^{-6} Torr vacuum for an hour. The annealing temperature is close to the transaction temperature of glass particles used so that the glass grits would melt and form a firm bondage between the CNT roots and the substrate. After annealing the CNTs on the topmost surface become vertically with one ends firmly embedded in the composite matrix formed by the glass, the other ends protruding out as depicted in Figure 2-8(b). An activation process is also implemented before testing the CNT samples. A specialty tape is used to mechanically remove loose ends of the CNTs on the surface, as well as “lift up” the CNTs left on the surface with stronger bonding. Therefore most of the CNTs on the film will be protruding up, which is a preferred morphology for field emission applications, as shown in Figure 2-8(c).

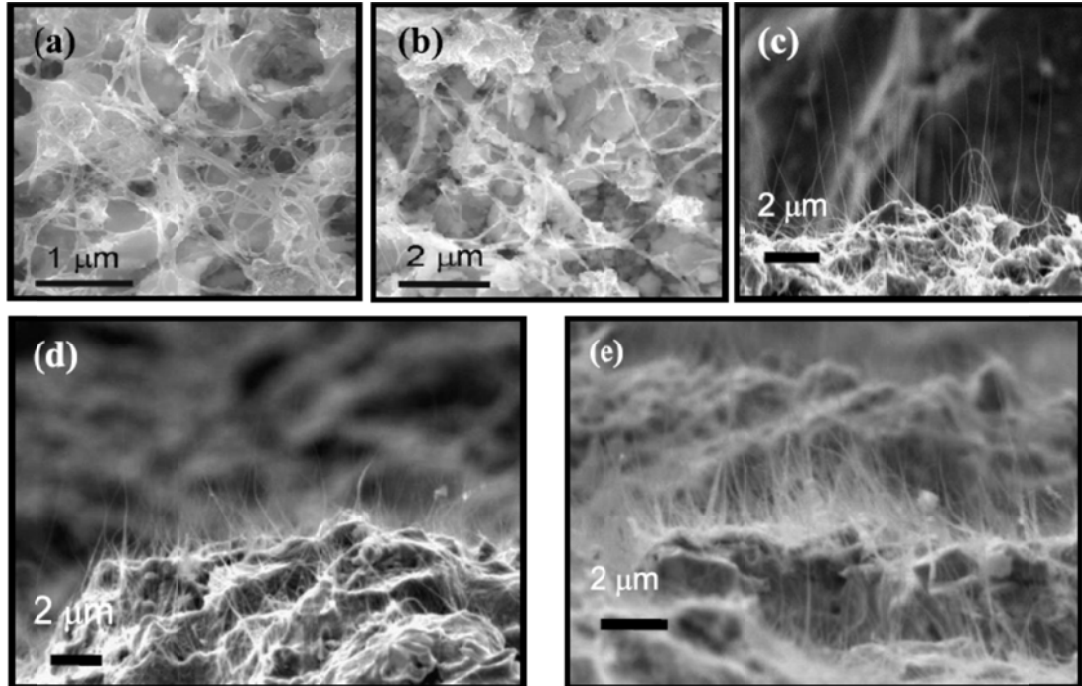


Figure 2-8 SEM images showing the top surface of the composite CNT film both: (a) before and (b) after vacuum annealing. The CNTs are randomly oriented on the surface. (c) Corss-sectional SEM image of the CNT cathode after the activation process. The surface CNTs are now vertically aligned in the direction perpendicular to the substrate surface. Corss-sectional SEM images of two cathodes fabricated under the same conditions except different CNT concentrations in the EPD suspension. Cathode in (e) was made in a suspension with $4 \times$ the CNT concentration than the cathode in (d).[41]

Another advantage of EPD method is that the density and film thickness of the as deposited films are controllable. Density of the film depends on the concentration of the EPD suspension. Figure 2-8(d) and (e) clearly demonstrates the increase of CNT packing density with the increase of suspension concentration, the exact amount is hard to determine though. The film thickness depends on the EPD experimental conditions such as the DC voltage, current and deposition time. Average thickness of our deposited film under same conditions is around $15 \mu\text{m}$ with less than 10% variation. It is also noticed that the film is slightly thicker around the edge than center, with variation of

about 5-10 μm over around 2000 μm distance due to the electric field being concentrated and enhanced around the edge of the exposed deposition sites.[41]

As described above, the EPD method provides much flexibility of field emission cathode design by controllable deposition area and patterns, along with approximate control of the film density and thickness.

The size, shape the packing pattern of CNT films can be controlled by only exposing the desirable area to the EPD suspension while blocking the rest. Our earlier attempts of cathode generation used shadow masks and polished cylindrical metal substrates shown in Figure 2-9(a). A Teflon cap with pre-defined size of opening was used to cover the substrate by mechanically tight contact with the deposition substrate, in this case a polished metal surface. However, this method works only reasonably for relatively larger sized cathodes (down to 1mm in diameter). Over the time, it would distort the post-deposited shape over the time due to the loose sealing of the substrate, thus the EPD suspension could leak into the blocked area, creating irregular shape around the edge.

For applications requiring smaller cathode size and more accurate film shape control, such as micro-focus x-ray generation for medical imaging, the shadow mask method becomes less desirable. Therefore, an alternative method was used in which microfabrication techniques such as photolithography were integrated.

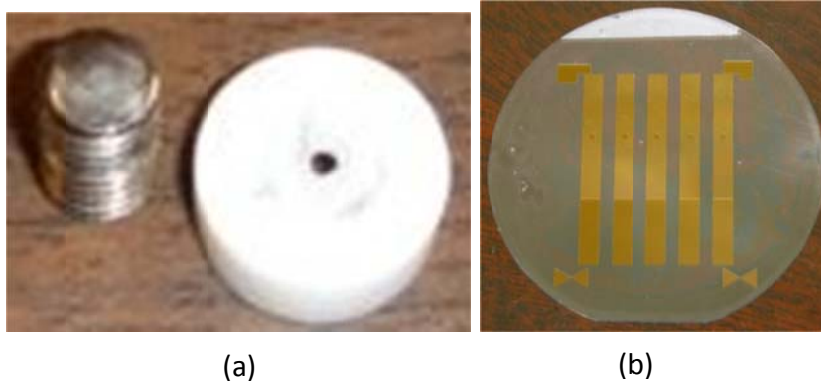


Figure 2-9 (a) Cylindrical metal substrate and shadow mask made of Teflon. (b) a pre-cut 2" silicon wafer with cathode pattern deposited by metal sputtering and photolithography

Two inch Silicon wafers with a $5\mu\text{m}$ silicon dioxide layer are chosen as the substrate for insulation purpose based on the required voltage required for our application. Figure 2-9(b) shows a precut silicon substrate containing five cathodes on the same wafer.

In order to fully utilize the size of the 2" standard wafers in round shape, a specific pattern of 5 cathodes were designed and deployed as shown in Figure 2-9(b). Copper is chosen as the conducting lines for its high conductivity, and another layer of Chromium is sputtered between the Copper pattern and the silicon to enhance the adhesion.

A thin layer of SU-8 photoresist is spin-coated on the silicon wafers in the first step. The wafers are then exposed under a UV light with pre-designed pattern. After the development of SU-8 layer, only the area dedicated to the conducting lines is exposed. Then a thin layer of Cr and Cu is sputtered on the wafer. With the lift-off of

the photoresist, we have a silicon based EPD substrate with metal conducting lines. Afterwards, another layer of SU-8 coating is applied with only CNT deposit sites exposed after the development. Since SU-8 is not alcohol soluble, therefore it blocks the entire substrate except CNT deposition sites and now we have a photomasked substrate ready for the electrophoresis deposition. The detail fabrication procedure of these photomasked substrates is shown in Figure 2-10. Before the electrophoresis deposition, we use the dicing saw to cut the substrates into desirable final shape as illustrated in Figure 2-11(a).

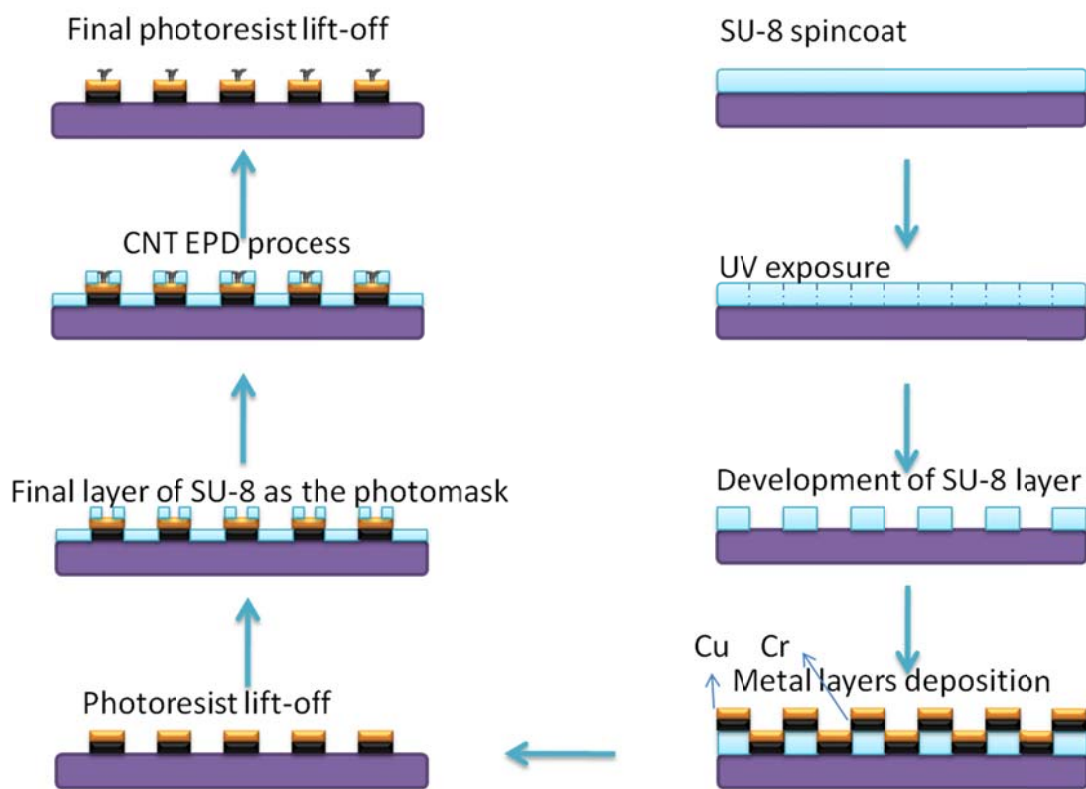


Figure 2-10 The fabrication procedure of photomasked silicon based EPD substrates

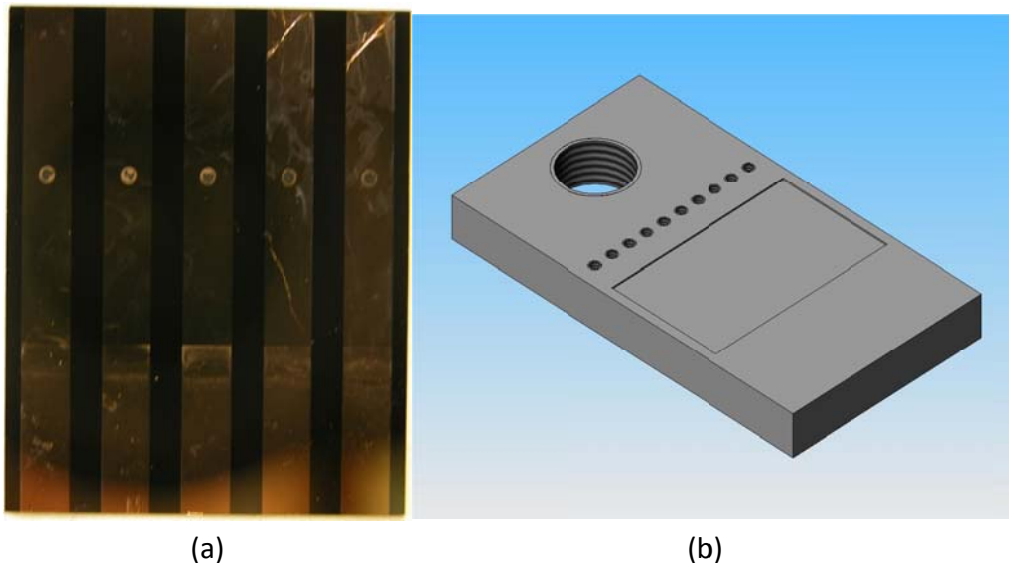


Figure 2-11 (a) the post-cut silicon based substrate with five CNT cathodes deposited. Copper stripes are used as conducting material for both EPD process and the field emission. Cathode is 1mm circular shape. The spacing between CNT cathodes is 5mm. (b) a specially designed EPD sample holder for the substrates in (a). It holds two substrates at a time so that a total number of ten CNT cathodes could be produced simultaneously.

A special substrate holder shown in Figure 2-11(b) is designed to accommodate two of such substrates simultaneously so that multiple cathodes could be produced at the same time. After the EPD process, a final lift-off process is implemented to remove the photomask. The cathode then is vacuum annealed at 500 °C for an hour, and the activation taping procedure is done before using the cathodes in experiments. This type of parallel fabrication suits the best for applications require multiple cathodes within a compact space. The consistency of the field emission performance between cathodes is better for the EPD conditions are exactly the same. Glass substrates with pre-deposit conducting lines are used later in my project to replace silicon wafer for better insulation between cathodes and the lower cost.

2-3-3 Field emission characterization for the Si-based cathode

Before integrating the prepared cathodes into another more complicated system, we need to characterize the field emission stability and performance. The field emission current characterizations of these film cathodes were measured using a simple parallel-plate configuration.

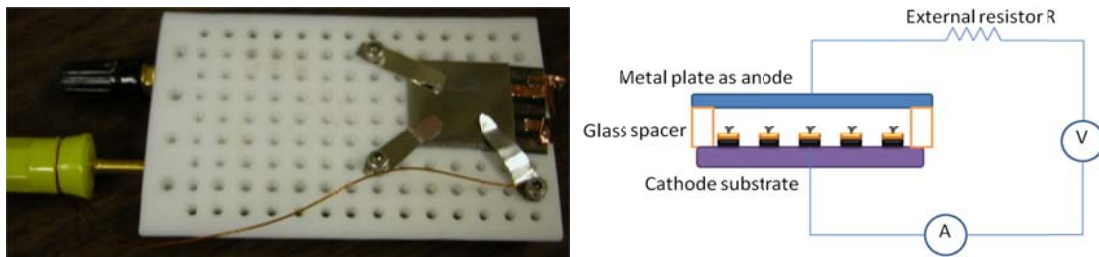


Figure 2-12 Left: the customized field emission sample holder for the silicon based 5-cathode substrate. It can measure three cathodes' performance at one time. **Right:** the simplified field emission scheme. A metal plate is served as anode with an external resistor connected as protector, while the cathode substrate is connected the ammeter for emission current measurement.

The illustration in the right of Figure 2-12 is a simplified scheme of our field emission testing set up. A metal plate is served as anode, and the electric field is applied between the anode and CNT cathodes over the gap distance controlled by the glass spacers. The anode surface is highly polished and well cleaned to avoid vacuum breakdown. The entire set-up is sealed inside a vacuum chamber with 10^{-7} Torr base pressure. The left figure shows a customized field emission sample holder for the silicon

based cathodes which could connect three individual cathodes and take the measurements.

With the integration of photolithography technique along with the parallel fabrication, multiple cathodes would have well defined areas and shapes, in the meantime; they share identical EPD conditions which would provide higher uniformity in the CNT deposition.

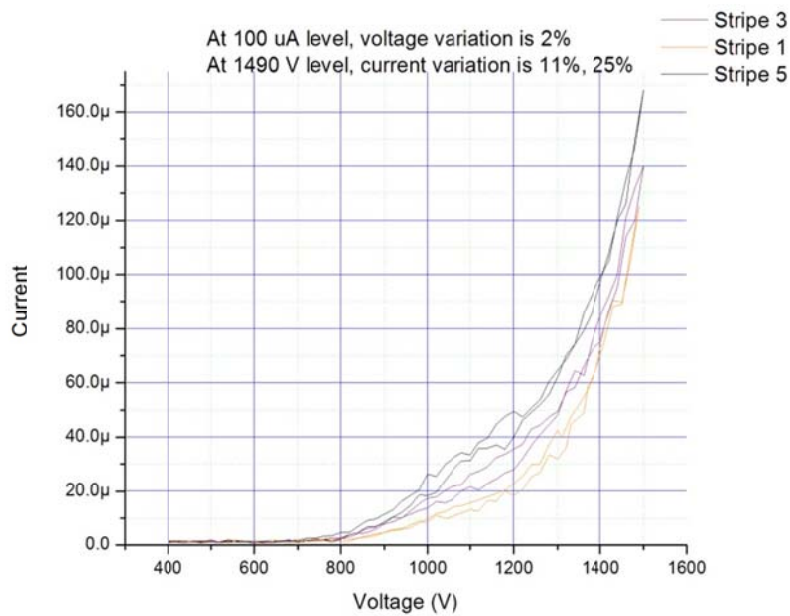


Figure 2-13. Field emission I-V curves of three cathodes on the same silicon substrate demonstrate good uniformity

Figure 2-13 illustrates the field emission I-V curves of three cathodes from the same silicon substrate with 1mm diameter round shape. 10 kV voltage is pulsed at 100 Hz with 10% duty cycle over 1mm distance with 100 kΩ external resistor. Despite the

fact that overall uniformity in field emission is decent, we can still notice the variance in field emission performance from different cathodes. To generate the same 100 μA current, variation of voltage among these three cathodes is about 5%. When applying the same 1490 v voltage, the current variation is 11%. With the maturing of our cathode fabrication technique, cathodes with much better performance and uniformity have been achieved.

References

1. Radushkevich, L. and V. Lukyanovich, Soviet Journal of Physical Chemistry, 1952(26): p. 88-95.
2. Oberlin, A., M. Endo, and T. Koyama, *Filamentous Growth of Carbon through Benzene Decomposition*. Journal of Crystal Growth, 1976. **32**(3): p. 335-349.
3. Abrahamson, J., B.L. Rhoades, and P.G. Wiles, *Structure of Carbon-Fibers Found on Carbon-Arc Anodes*. Carbon, 1980. **18**(1): p. 63-63.
4. Izvestiya Akademii nauk SSSR. Metals, 1982(3): p. 122-17.
5. Kroto, H.W., et al., *C-60 - Buckminsterfullerene*. Nature, 1985. **318**(6042): p. 162-163.
6. Smalley, R.E. *Formation and properties of C₆₀ and the fullerenes*. in *National Institute of Standards and Technology*. 1990.
7. S. Iijima, *Helical Microtubules of Graphitic Carbon*. Nature, 1991. **354**: p. 56-58.
8. Dai, H.J., *Probing electrical transport in nanomaterials: Conductivity of individual carbon nanotubes (vol 272, pg 523, 1996)*. Science, 1996. **272**(5270): p. 1861-1861.
9. R. Saito, et al., *Electronic structure of chiral graphene tubules*. Applied Physics Letters, 1992. **60**(18): p. 2204-2206.
10. Mintmire, J., B.I. Dunlap, and C.T. White, *Are fullerene tubules metallic?* Phys. Rev. Lett, 1992(68): p. 631.
11. Hamada, N., S.I. Sawada, and A. Oshiyama, *New one-dimensional conductors: graphitic microtubules*. Phys. Rev. Lett, 1992(68): p. 1579.
12. Filho, A.G.S., et al., *Stokes and anti-stokes Raman spectra of small diameter isolated carbon nanotubes*. Phys. Rev. B, 2004. **69**: p. 1154.
13. Frank, S., et al., *Carbon nanotube quantum resistors*. Science, 1998. **280**(5370): p. 1744-1746.

14. Lu, J.P., *Elastic Properties of Single and Multilayered Nanotubes*. Phys. Rev. Lett., 1997. **79**(7): p. 1297-1300.
15. Treacy, M.M., T.W. Ebbesen, and J.M. Gibson, *Exceptionally high Young's modulus observed for individual carbon nanotubes*. Nature, 1996. **381**: p. 678-680.
16. Wong, E.W., P.E. Sheehan, and C.M. Lieber, *Nanobeam Mechanics: Elasticity, Strength and Toughness of Nanorods and Nanotubes*. Science, 1997. **277**(26): p. 1971-1975.
17. Kim, P., et al., *Thermal transport measurements of individual multiwalled nanotubes*. Physical Review Letters, 2001. **87**(21): p. -.
18. Hone, J. and e. al., *Thermal conductivity of single-walled carbon nanotubes*. Physical Review B, 1999. **59**: p. 2514-2516.
19. Meyyappan, M. and e. al., *Carbon Nanotubes: Science and Applications*. 2005.
20. Heller, D.A., et al., *Single-walled carbon nanotube spectroscopy in live cells: Towards long-term labels and optical sensors*. Advanced Materials, 2005. **17**(23): p. 2793-+.
21. D. Temple, *Recent progress in field emitter array development for high performance applications*. Materials Science and Engineering, 1999. **R24**: p. 185-239.
22. V.H. Binh, N. Garica, and S.T. Purcell, *Electron field emission from atom-sources*. Advances in imaging and electron physics, 1996. **95**: p. 63-153.
23. I. Brodie and C.A. Spindt, *Vacuum Microelectronics*. Advances in Electronics and Electron Physics, 1992. **83**: p. 1-106.
24. I. Brodie and P.R. Schwoebel, *Vacuum microelectronic devices*. Proceeding of the IEEE, 1994. **82**(7): p. 1006.
25. C.A. Spindt, et al., *Physical properties of thin-film field emission cathodes with molybdenum cones*. Journal of Applied Physics, 1976: p. 5248-5263.
26. Gomer, R., *Field Emission and Field Ionization*. 1961, Cambridge, MA: Harvard University Press.

27. Baxendale, M., *The physics and applications of carbon nanotubes*. Journal of Materials Science: Materials in Electronics, 2003. **14**(10): p. 657-659.
28. Huang, J.Y., et al., *Giant field enhancement at carbon nanotube tips induced by multistage effect*. applied physics letters, 2005. **87**(5): p. -.
29. H.E. Crooks, J.Sangster, and G.M. Ardran, *The fexitron 848 portabel x-ray apparatus*. Radiology, 1972(456): p. 311.
30. G.S. Hallenbeck, *Clinical evaluation of the 350-KV chest radiography system*. Radiology, 1974. **117**: p. 1-4.
31. P. Schagen, *Alternatives to thermionic emission*. Brit. J. Appl. Phys., 1965. **16**: p. 293-303.
32. W. Zhu, G.P. Kochanski, and S. Jin, *Low-field electron emission from undoped nanostructured diamond*. Science, 1998. **282**: p. 1471-1473.
33. P.M. Ajayan and O. Zhou, *Applications of Carbon Nanotubes*, in *Carbon Nanotubes : Synthesis, Structure, Properties, and Applications (Topics in Applied Physics, 80)*, M.S. Dresselhaus, G. Dresselhaus, and P. Avouris, Editors. 2000, Springer-Verlag: Heidelberg. p. 391-425.
34. Bower, C., O. Zhou, and W. Zhu, *Fabrication and field emission properties of carbon nanotube cathodes*, in *Material Research Society Symposium Proceedings*. 2000.
35. Shimoda, H., et al., *Self-assembly of carbon nanotubes*. Advanced Materials, 2002. **14**(12): p. 899-901.
36. Oh, S.J., et al., *Room-temperature fabrication of high-resolution carbon nanotube field-emission cathodes by self-assembly*. applied physics letters, 2003. **82**(15): p. 2521-2523.
37. Jung, H., et al., *Carbon nanotube field emitters for display applications using screen printing*. Prim 5: The Fifth Pacific Rim International Conference on Advanced Materials and Processing, Pts 1-5, 2005. **475-479**: p. 1889-1892.
38. Gao, B., et al., *Fabrication and electron field emission properties of carbon nanotube films by electrophoretic deposition*. Advanced Materials, 2001. **13**(23): p. 1770-1773.

39. O. Van der Biest and L.J. Vandeperre, *Electrophoretic Deposition of Materials*. Annu. Rev. Mater. Sci., 1999. **29**: p. 327-352.
40. W.B. Choi, et al., *Electrophoresis deposition of carbon nanotubes for triode-type field emission display*. Appl. Phys. Lett., 2001. **78**(11): p. 1547.
41. Calderón-Colón, X. and O. Zhou, *Fabrication, characterization and integration of carbon nanotube cathodes for field emission x-ray source*. 2009, University of North Carolina at Chapel Hill: Chapel Hill, N.C. p. 1 electronic text.

Chapter 3 Design of multi-beam micro-CT scanner

For years researchers and scientists have dedicated to finding alternative ways for x-ray generation in order to overcome some of the disadvantages from thermionic sources such as high operating temperature, slow response time et al. Field emission as a “cold cathode” technology, nicely fall into people’s sight. The concepts of field emission x-ray sources were suggested in the mid-1950s. Unfortunately, all of the early experimental systems suffered from either high extraction field or low emission current due primarily to the limitations of the electron field emitters [1, 2]. CNT has been widely considered as one of most prospective electron emission materials because of their large aspect ratio, low threshold electric field and capability of providing large and stable field emission current[3]. Interests around using CNT for x-ray source started to arise [4, 5]. The CNT source is most appreciated in applications that require high switching speed and accurate x-ray exposure control. More recently investigations on using CNT field emission x-ray sources for high resolution medical imaging purposes[6, 7], and CNT based electron beam radiation sources for radiobiological studies[8] have drawn some public attention.

3-1 Overview of computed tomography (CT) and Micro-CT

Computed tomography (CT) is one of the most important breakthroughs in the entire field of radiology [9, 10]. It enables the acquisition of 3D internal structural and anatomic information within object in a completely non-invasive way. Nowadays CT has become an important probing and diagnostic tool for investigations in biological, medical, material, and industrial applications [11-20].

Computed tomography (CT) first became feasible with the development of modern computer science and technology back in the 1960s, however some of the ideas and concepts it is built upon could be traced back at the beginning of 20th century. In 1917, the Bohemian mathematician J. H. Radon proved the feasibility of “reconstructing” material distribution or property in an object layer with knowledge of the integral values among any number of lines passing through that layer[21]. The first experiments on medical application of this type of reconstruction, however was done by a South African physicist A. M. Cormack without the knowledge of those previous studies between 1957 and 1963. In 1972, English engineer G.N. Hounsfield successfully surprised the entire medical world by developing the first CT scanner, again, without the knowledge of the earlier findings mentioned above[9]. And he received the Nobel Prize in medicine in 1979 along with Cormack for this breakthrough. In 1974, Siemens became the first traditional manufacturer of radiological equipment to market a head CT scanner. And soon after that, in the late 70s, 18 companies started to offer CT equipment. At present CT is one of the most important methods of radiological diagnosis. Based on recent

statistics, by 2002 there were approximately 5000 CT units are installed in U.S. hospitals, at a cost of up to a million dollars per unit [11]

Computed tomography systems have been through several major generations for the past four decades. Parallel beam geometry was the basic design concept for the first generation CT scanners including the very first EMI brain scanner. A highly collimated pencil beam and one or two detectors swept across the object in a translational fashion at each imaging position to collection transmission data as illustrated in Figure 3-1(a). Then the x-ray source and detector pair rotated around the object for another degree to the next imaging position to repeat the translational projection image acquisition until 180° coverage is reached. First generation CT scanner normally would require 4.5 to 5 minutes to acquire the entire dataset which restricted the screening throughput. The second generation scanners use multiple pencil beams coupled with a leaner detector array, resulting in a small-angled fan beam geometry whose apex originates at the x-ray tube depicted in Figure 3-1(b). The fan beam translates across the object to collect a set of transmission data. Afterwards, both source and object still needs to rotate to the next imaging position, with a rather large angle compared to the first generation though. The larger rotational increments and increased number of detectors shorten the scanning time to the range from 20s to 3.5 minutes. As showed in Figure 3-1(c), the third generation scanners are still based on the fan-beam geometry, with a fan angle large enough to cover the whole object. Therefore the rotational motion required for data acquisition is further reduced. The fourth generation scanners are equipped 600 or more detector units as a stationary ring

around the object. X-ray tube with fan-beam rotates within the detector ring. More recently, in the pursuit of shorter scanning time, multislice or volume CT scanners has been developed. The data from these scanners are collected in volumes rather than individual slices. In the scanning process, the object is transported through the gantry as the x-ray tube rotates, forming a spiral geometry.

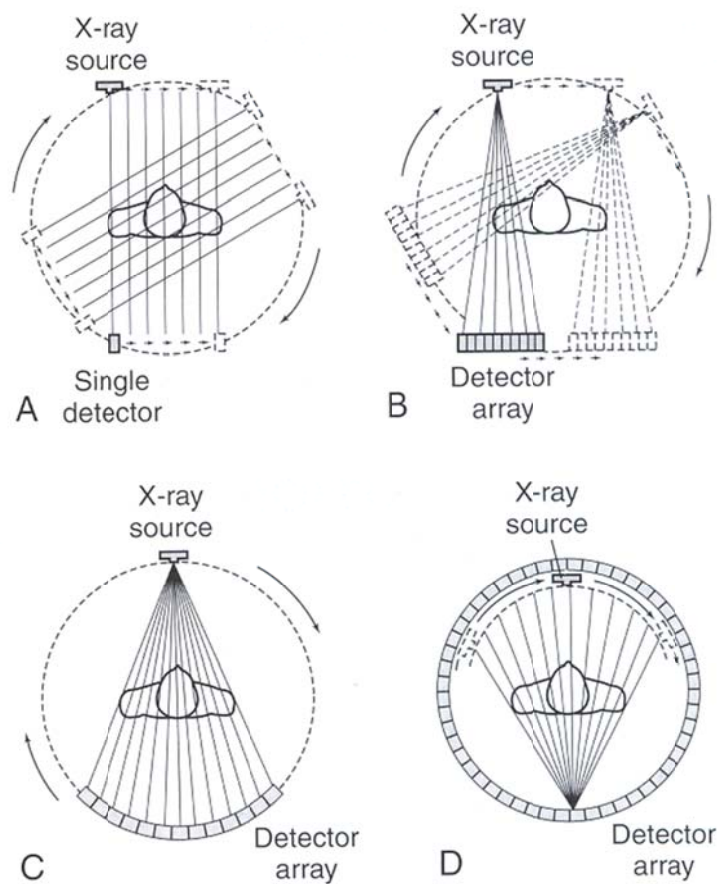


Figure 3-1 The geometries of the first four generations of CT scanners. **A.** Evolution of the CT scanner: (a) The first-generation of scanner using a pencil x-ray beam and a single detector. (b) The second-generation of scanner with a fan x-ray beam and multiple detectors. (c) The third-generation of scanner using a fan x-ray beam and detector array. (d) The fourth-generation of scanner with a fan beam and a stationary circular detector array.

CT technology has become a widely used diagnostic and probing tool in all sorts of areas. However, the rather large spatial resolution of clinical CT scanners could not meet the needs for high-resolution application, for instance, small animal imaging.

The spatial resolution of a CT scanner is determined by the focal spot size of x-ray source and detector element size. As micro-focus x-ray tubes with micrometer level focal spot become available, Micro-computed tomography (micro-CT) technique has been developed to yield tomographic images of small objects [15, 18, 19].

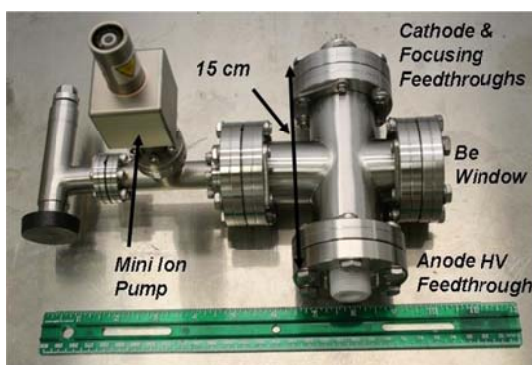
It is actually a scaled down version of medical CT scanner but with much higher spatial resolution, typically in the order of 10s of micrometers [15, 18-20]. Micro-CT has become a powerful diagnostic tool for high-resolution imaging of bone structures and soft tissues of small animals, [14, 15] materials analysis, and inspection.

3-2 Micro-CT imaging system with single-beam CNT micro-focus x-ray tube

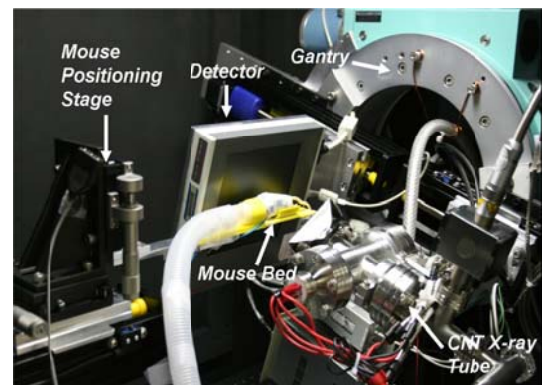
Simply speaking, X-ray computed tomography is an imaging modality that provides anatomical data by measuring the attenuation of x-ray beam as it passes through an object. In order to reconstruct two-dimensional images of a slice within the object, x-ray attenuation projection data need to be acquired from multiple angles. Therefore the x-ray source equipped in a CT system affects its imaging capability directly. Conventional thermionic x-ray tubes are currently widely used for x-ray generation in

most of the commercial CT scanners. As discussed in Chapter 2, the thermionic technology suffers several inherent limitations [22], which would essentially affect the imaging quality of a CT system. The slow response time limits the *temporal resolution* of the x-ray source while high operating temperature results in short lifetime and large device size and complication.

On the contrary, due to the instantaneous field emission nature, CNT field emission x-ray source has made high temporal resolution feasible [5, 23]. With our EPD fabrication technique, our CNT source also provides great flexibility in both source and system design, so that higher spatial resolution and novel system geometry could be achieved. These CNT sources have been successfully integrated into a micro-focus x-ray tube, based on which a dynamic single-beam micro-CT system.[24-26]



(a)



(b)

Figure 3-2 (a) A micro-focus x-ray tube with CNT field emission x-ray source. It could stably generate as high as 2 mA tube current and 100 μm effective focal spot x-ray beam. [24](b) A dynamic single-beam micro-CT scanner equipped with CNT micro-focus x-ray tube. It can provide 10 ms temporal resolution at 81 μm spatial resolution. This system has the capability of live animal free breathing gated CT for both respiratory and cardiac imaging.[26]

Shown in Figure 3-2(b), this single beam micro-CT system consists of a compact CNT field emission micro-focus tube (shown in Figure 3-2(a)), a flat panel x-ray detector (C7940DK-02, Hamamatsu), a small-diameter goniometer (Huber 430, Germany) and a stationary mouse bed, a physiological triggering system (BioVet, Spin Systems) and the central controlling PC. Both the x-ray tube and detector rotates around the stationary object to acquire transmission data from multiple angles. As the CNT field emission current is driven by electric field rather than heat, it could be fairly precisely modulated by varying the pattern and amount of external field. Therefore, by coupling the physiological signal (respiratory and cardiac) from the mouse with pulsed x-ray beam and detector reading, the single-beam micro-CT system enables the feasibility of prospective gated imaging for a free breath mouse. Some sample reconstructed images from this system for a cardiac disease mouse model are shown in Figure 3-3.

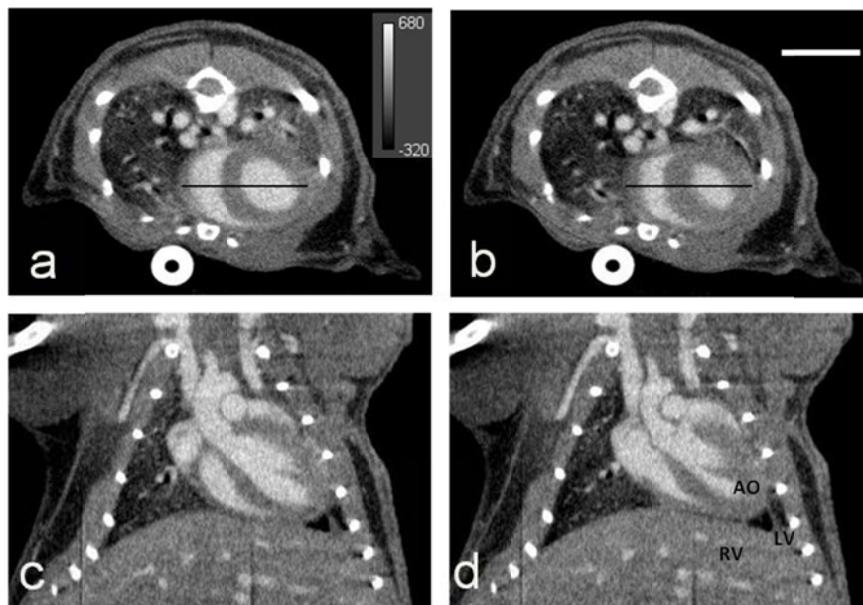


Figure 3-3 Axial (a, b) and coronal (c, d) slice images of a wild-type mouse at 0 msec (a, c) and 55 msec (b, d) after the R wave.

As described above, this system uses a single x-ray beam in a step-and-shoot mode; the total scanning time for 400 projections is around 400s. If operated in gated mode, scanning time is essentially extended to 15-30 minutes depending on the respiratory and heart rates of the mouse.[26]

3-3 Design of a Multi-Beam Micro-CT system based on CNT field emission technology

3-3-1 The evolution of CT geometry for faster scanning

High screening throughput and faster scanning speed is always desirable for CT. With the improvements in x-ray source and informational technology, the scanning speed has already increased [21, 27]. As introduced in previous section, over the 40 years of CT development, it has evolved several generations, and each evolution comes with improvement in scanning speed. From the 1st generation's pencil beam translate and rotate scanning scheme to the 2nd generation's fan-beam, the scanning time to acquire a full dataset decreases from around 5 minutes to 20s. With larger fan-angle beam that covers the whole body, the 3rd generation CT scanner could finish a whole scan in 1 to 3 seconds. Fourth generation scanners equips with a stationary multi-detector ring and only needs to rotate the x-ray tube, with a similar fan-beam scheme, the scanning time is also very short.

In the mid 1980's, the invention of the power slip ring facilitated the invention of spiral (helical) scanners with scan time less than a second [28]. Unlike the previous generations, in helical CT, projections are continuously acquired while the patient is translated at a constant speed. There is no acceleration or deceleration of patients during the scan, the nondata acquisition period existing in step-and-shoot mode is essentially eliminated; therefore the scanning time is further cut. Spiral/multislice CTs are generally regarded as the fifth generation of CT scanners.

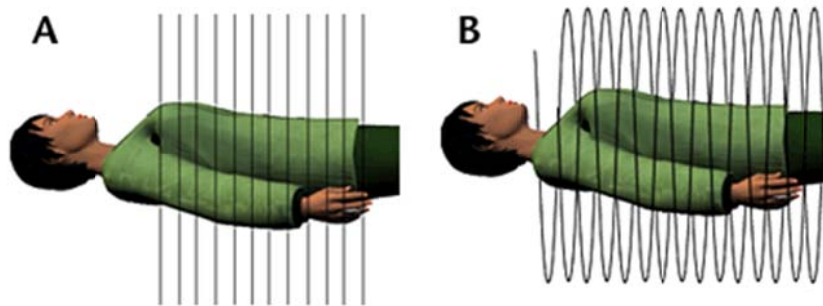


Figure 3-4 (a) Conventional CT scans take pictures of slices of the body, then translate the patient. These slices are a few millimeters apart. (b) The newer spiral (also called helical) CT scan takes continuous pictures of the body in a rapid spiral motion, so that there are no gaps in the pictures collected.. Reproduced from (imaging.cancer.gov)

With the advancement of technology, people have managed to use better components, better electronic integration to shorten the CT scanning time. However, the mechanical motions required for CT scan have been the bottleneck for cutting the scan time further down. More recently, the development of dual-source CT [29] (shown in Figure 3-5) has already provided a gantry rotation speed of 0.33s but it has been

expected that the gantry rotation time less than 0.3 s will be extremely difficult to obtain due to the mechanical limit of material.

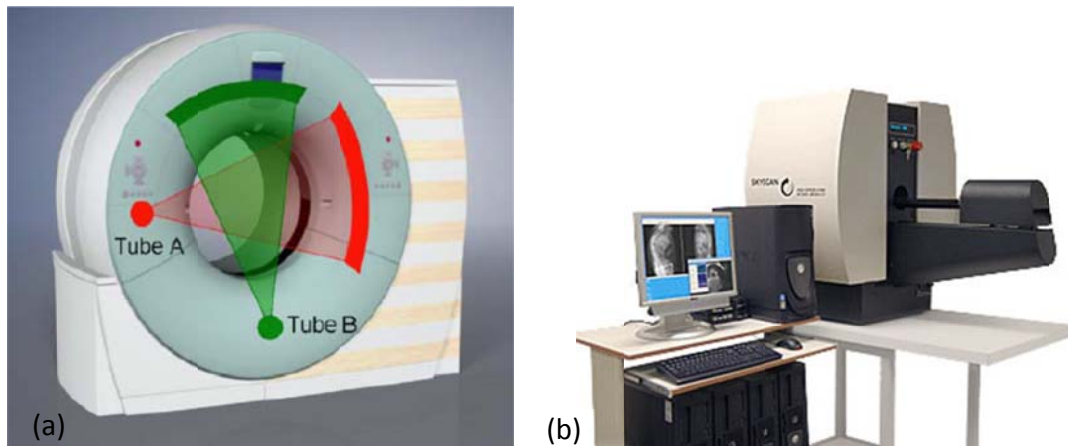


Figure 3-5 (a) The DSCT scanner from Siemens. This scanner consists of two x-ray tubes and two sets of detectors with 90° offset particularly designed for cardiac CT imaging. Shortest gantry rotation time is 0.33s. (b) Skyscan 1180 high throughput dual source micro-CT

As it is getting more and more difficult to keep increasing the gantry rotation speed, researchers have proposed and investigated several novel ways to remove the mechanical motion involved in CT scanning to increase the data acquisition rate and dynamic imaging capability.

Some of the prototype devices have been developed including the Dynamic Spatial Reconstructor (DSR) [30], the electron-beam CT (EBCT) [31], and scanning beam digital x-ray (SBDX) [32, 33].

As illustrated in Figure 3-6(a), the Electron Beam CT (EBCT) utilizes an electromagnetic field to steer an intense electron beam produced by a linear accelerator along the target rings positioned around the patient to generate a scanning x-ray beam

from different viewing angles without any mechanical motion [34]. An alternative way is to use a large number of x-ray sources positioned around the object so that projection images from different directions are obtained by energizing each tube. Dynamic Spatial Reconstructor (DSR) developed at the Mayo Clinic in the early 1980s is a good representation for such proposal [35].

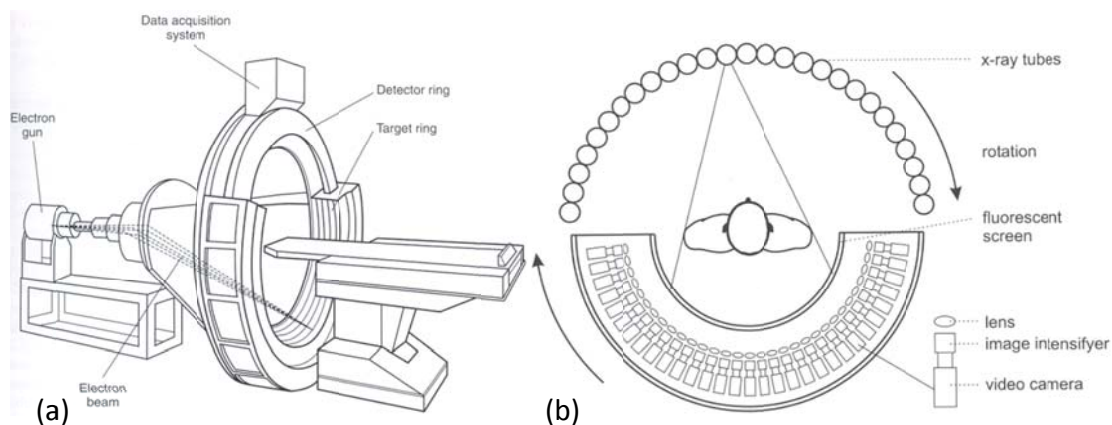


Figure 3-6 Alternative concepts for fast volume scanning (a) EBCT permits single scans in the range of 30 to 100 ms without mechanical motion. (b) DSR allowed volume scanning in cone-beam geometry with 1 s rotation time. (reproduced from [36])

3-3-2 Design of multi-beam micro-CT scanner

Although those abovementioned devices have been demonstrated to have superior high temporal resolution over conventional single x-ray source device, their further developments were hindered by either the cost, size, and maintenance related issues (for DSR) or limited viewing angle due to difficulty of steering high energy electron beam using electromagnetic field (for EBCT and SBDX). Another method to

generate a scanning x-ray beam is to use as many x-ray sources as needed in a geometry that provides sufficient angle coverage for tomographic imaging.

With our novel CNT field emission x-ray source, we can fully take advantage of low operating temperature, instantaneous response time, and great design flexibility. Here we presented the very first step towards the development of a stationary gantry-free micro-CT scanner. To evaluate the feasibility, a prototype multi-beam micro-CT (MB μ CT) scanner using a small segment of a CNT x-ray source array was constructed. The source comprises 20 discrete CNT based field emission pixels. Each CNT pixel has its own electronic control circuitry and can be addressed independently. The multi-beam x-ray source array can be programmed to generate a scanning x-ray beam. The micro-CT scanner using this source array is able to capture up to 20 projection images from different viewing angles without any mechanical movement of the system. After one linear scan from 20 pixels, the object would rotate 36° to the next imaging position until it finishes a full 360° rotation within only 10 steps.

3-3-3 System overview

The geometry of this scanner is shown in Figure 3-7. The angular resolution of the system is equal or less than 2°, with 36° coverage from the entire linear source. The total length of the 20-pixel cathode array is 10 cm with a pitch of 5mm between two adjacent pixels. The shortest source-to-object distance (SOD) to be 14.5cm. For the linear array, the actual distance between the x-ray focal point and the object varies from beam to beam. The source-to-detector distance (SDD) was set to 21.7 cm to achieve a

system magnification factor of 1.5. For this prototype MB μ CT scanner, rotation of the object is still required in order to acquire a full set of projection images for reconstruction, because of the limited number of x-ray beams in the current system. The source with 20 beams in the current geometry has an angular coverage of 36°. A total of 10 rotation steps are needed to fulfill a 360° CT scan.

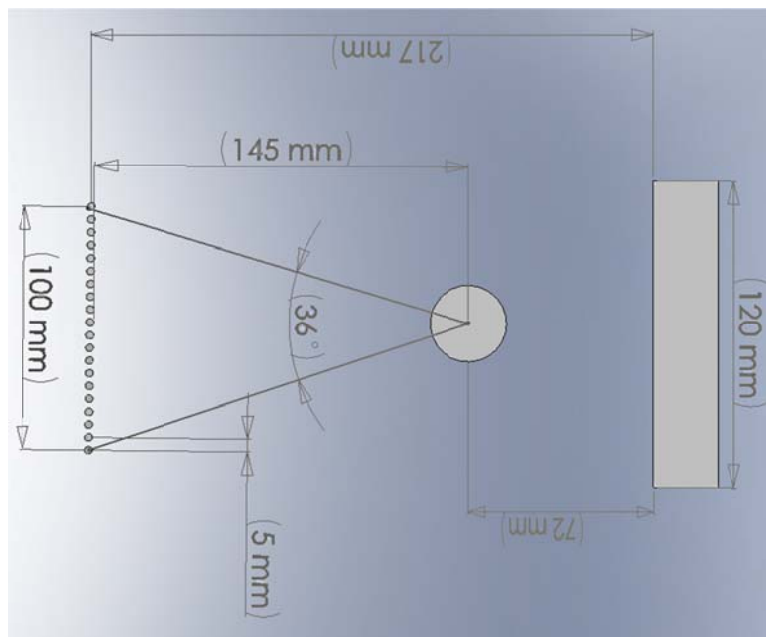


Figure 3-7 imaging geometry of the multi-beam micro-CT system

The MB μ CT scanner comprises a linear CNT field emission source array housed in a vacuum chamber for x-ray generation, a 3-axis rotary table for rotating the object, a 2-axis flat panel x-ray detector assembly, and a user control interface written in LabView (National Instruments Corp). The entire multi-beam x-ray source array was sealed inside a 6-way vacuum chamber at a base pressure of 10^{-8} Torr. A large 6" beryllium window was installed to accommodate the x-ray beam exit of the spatially distributed x-ray

source. The circuitry can individually control the on/off status of the connection between each pixel and earth ground through a home-made LabView interface from the control console computer. This software interface also integrates a feedback loop to stabilize emission current, as well as performing the image acquisition function.

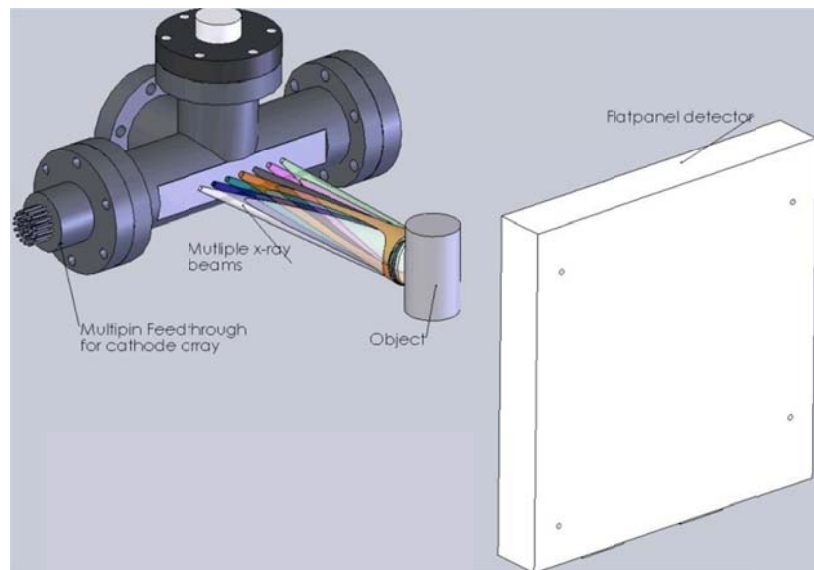


Figure 3-8 Schematic drawing of the multi-beam x-ray imaging system with a 20-beam MBFEX x-ray source array, a rotation stage, and a flat panel x-ray detector.

3-3-4 Multi-beam field emission x-ray source design

The most essential part of the MB μ CT system is the CNT field emission based multi-beam x-ray source. The x-ray source embedded in this system essentially comprises of two parts, a 6-way vacuum chamber with 6" inner diameter and the in-vacuum CNT based multi-beam source assembly. Due to the space limitation of the standard chamber, a total length of 10cm in source array is used. In order to achieve

reasonable angular sampling between x-ray projections from adjacent sources, a 5mm cathode-to-cathode spacing is used, considering the engineering difficulties with fine space.

The cathode array contains 20 individual addressable CNT field emission cathodes deposited on a single piece of glass substrate using the micro-fabrication and CNT deposition techniques introduced in Chapter 2 [37, 38]. A two-stage Einzel lens structure was adopted for the design of electron lens to focus electron beam to a small focal spot on x-ray anode. Molybdenum is chosen as target material for spectrum optimization.

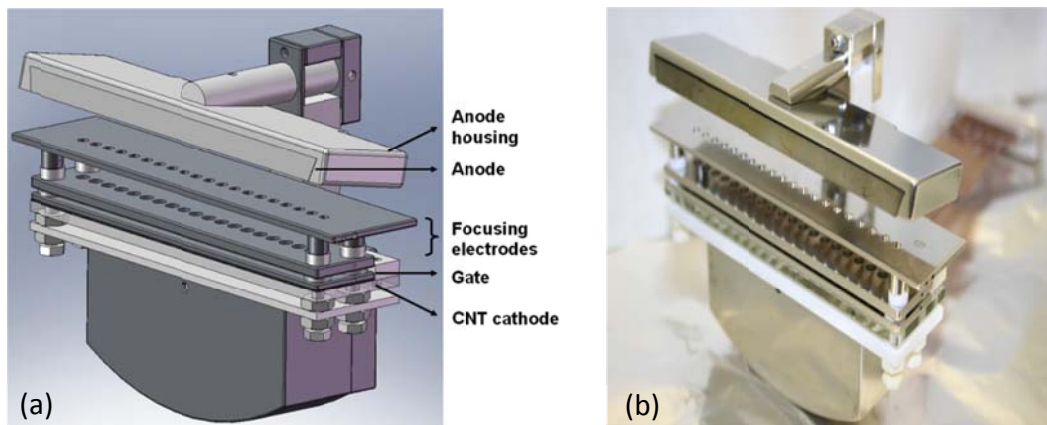


Figure 3-9 (a) The CAD drawing of the newly designed multi-beam x-ray tube assembly which includes a Molybdenum x-ray anode housed in a stainless steel assembly with 12° tilting angle, a Einzel focusing lens, an electron extraction gate electrode and an 20-beam integrated CNT field emission cathode array (b) The as-fabricated multi-beam x-ray source assembly. The metal surfaces were highly polished and all the materials were HV compatible to improve source stability during high voltage operation.

As shown in Figure 3-9(a), the MBFEX x-ray source has a simple linear source array configuration in order to simplify the system design although a curved source

structure maybe more desirable for imaging purpose [39]. The linear x-ray source comprises of a CNT field emission cathode array as the electron source. In the electron beam path downstream of the CNT cathode, the rest of the x-ray source assembly includes a gate extraction electrode, a two-stage Einzel electron focusing lens, and a Molybdenum x-ray anode. Tungsten mesh (100-mesh) is used as gate to extract the electrons from the cathode. The diameter of the tungsten wire is 0.001", thus the opening of the mesh is 81% of the total area. Several pieces of glass chips with 150- μm thickness are place between the cathode and the gate as the spacer.

The following power supplies connected to the four electrodes of the MBFEX source array, respectively, are: Matsusada AU80P15 (80 kV/15 mA) for anode, Glassman PS/FC03P40 (3kV/40 mA) for gate electrode, Stanford Research PS350 (2.5 kV/10 mA) for both focusing electrodes. A Keithley 2000 multimeter was used to record the cathode field emission current. Each of the 20 CNT cathodes is connected to a metal-oxide-semiconductor field-effect transistor (MOSFET) switching circuit. The design of the molybdenum x-ray anode adopted the line focusing principle introduced in Chapter 1 with a 12 degree tilting angle. Figure 3-9(b) shows the 20-beam x-ray source array assembled before it was put inside the vacuum chamber. The 20-beam MBFEX source was sealed in a high voltage compatible 6-way cross vacuum chamber operated at 10^{-9} Torr vacuum. A 400 μm thick 6" Beryllium window was installed on the front side of the vacuum chamber as the x-ray beam exit port. In order to generate x-ray radiation, field emission electrons are extracted from the CNT cathode unit by applied gate electric field and traveling through the focusing lens structure and hit the anode. The electric

potential applied on the focusing electrodes would provide focusing power to form a fine electron focal spot on the anode surface and generate x-ray radiations.

The key component of this newly developed MBFEX source is an integrated CNT field emission cathode array with 20 field emitting units. The previously reported MBFEX source simply used multiple standalone cathodes arranged together to form a cathode array [7, 40, 41]. In that case, each cathode unit was fabricated separately with its own electron emission cathode and corresponding electron emission extraction and focusing electrodes. The assembled cathode array is simply a scaled-up version of its single unit counterpart. The standalone cathode array design approach works for simple multi-beam x-ray system design needs only small number of x-ray beams (e.g. less than 10) and relative low x-ray source packing density. For a more complex system requiring up to hundreds of x-ray beams, such as the proposed multi-beam scanners for tomosynthesis and computed tomography applications, as the number of x-ray units (beams) goes up, the standalone design approach becomes cumbersome and sometimes even infeasible due to the increasing complexity of system design. On the other hand, for applications requiring high spatial resolution such as micro-CT imaging of small animal, there is a demand on MBFEX source with much higher x-ray source packing density (as small as few mm in source pitch) which cannot be easily achieved with the current MBFEX source design based on simple assembly of standalone single x-ray source unit. More important for the current MBFEX source fabrication, each standalone cathode unit is fabricated independently. In terms of consistency of cathode performance, any small uncontrollable variation during the complex fabrication

procedure could cause significant change of cathode emission property eventually. Each electron emission cathode needs to be further assembled with the rest of cathode assembly (gate and focusing electrodes). This assembling procedure may introduce more uncertainties and errors, e.g. misalignment of cathode, gate and focusing structures. Overall those intrinsic issues could hinder the implementation of the MBFEX technology, especially for applications that a large number of cathode units are required.

With the recent development of CNT cathode deposition and micro-fabrication techniques, it is possible to achieve an integrated cathode array design with more compact device size, higher packing density and more consistent cathode emission property. Here we demonstrated the feasibility of a novel cathode array design by fabricating a 20-beam CNT field emission cathode array on a single piece of glass chip substrate. As shown in Figure 3-10(a), a glass substrate with dimensions of 113mm×28mm was used as the cathode substrate. A total of 20 parallel Ag lines for conducting electrical current were printed on the glass substrate with a center-to-center distance at 5mm. The Ag lines serve the purpose of providing the individual control of field emission current from each CNT cathode unit. The printing procedure was optimized to achieve strong adhesion between the Ag layer and the substrate.[42]

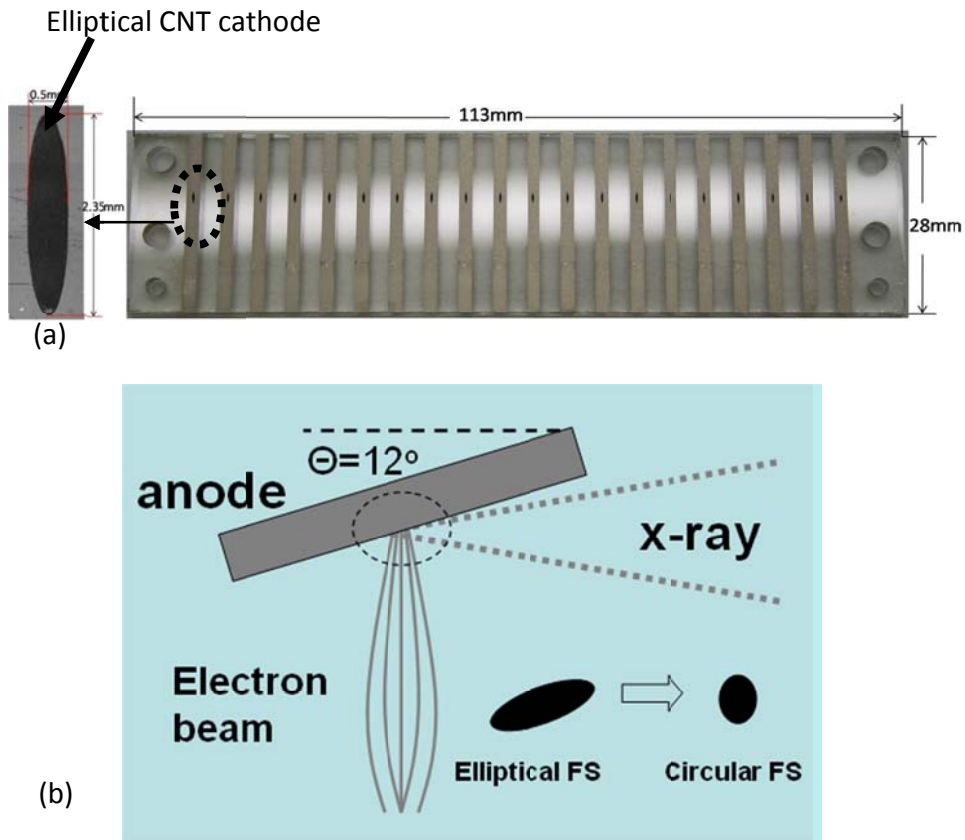


Figure 3-10. (a) The CNT cathode array has 20 CNT field emission cathode deposited on a single glass chip substrate. (b) Line focus principle: the emitting cathode was designed to have an elliptical shape in order to achieve a desired isotropic focal spot for x-ray imaging.

The corresponding 20 CNT field emitting cathodes were patterned on the predetermined location on the Ag conducting lines. The CNT emitters were deposited using the previously reported photolithography and electrophoresis process [37]. Each cathode was in an elliptical shape, with a long axis of 2.35mm and a short axis of 0.5mm. The specific geometry was designed to achieve an isotropic effective x-ray focal spot on anode. As shown in Figure 3-10(b), with an anode tilting angle θ at 12 degree, the effective focal spot projected along the beam direction from the real elliptical focal spot on the anode will have a circular shape. The as-fabricated CNT cathode array was then

annealed in vacuum and mechanically activated before it was used for the field emission test later on.

With such integrated cathode array design, important geometric parameters such as cathode shape, cathode location and cathode pitch can be predefined and well controlled during the fabrication process, which is important for the alignment between the cathode, gate and focusing electrodes. Better system alignment generally translated to finer focal spot and higher electron beam transmission rate, which is desirable for an x-ray tube. Compared to standalone cathode design, the integrated design also greatly simplified the wiring and assembly of the x-ray source. This new design of cathode also allows higher cathode packing density, which is important for applications such as micro-CT imaging where a great number of beams are required to achieve higher spatial resolution.

To achieve better system imaging resolution, a finer focal spot is always preferred. Based on a series of computer simulations on electron optics using a commercial software package Vector Fields 10.5 (Cobham Technical Services), a two-stage focusing electrode structure was introduced to achieving the focusing power required for micro-CT imaging application. As shown in Figure 3-11(a), the two-stage focusing design was based on so-called Einzel focusing structure, a concept widely used in electron microscopy and other electron optical applications. In our previous investigation, such design has been successfully applied to a single-beam micro-focus x-ray source to achieve a fine focal spot suitable for small animal imaging[43]. For the

current MBFEX source design, the focusing structure needs to be further optimized because of the high x-ray source packing density thus much smaller cathode pitch (5 mm) of the cathode array. For the current prototype multi-beam system, the targeted focal spot size was around 100 μm , which would result sufficient system resolution for small animal imaging in pre-clinical research.

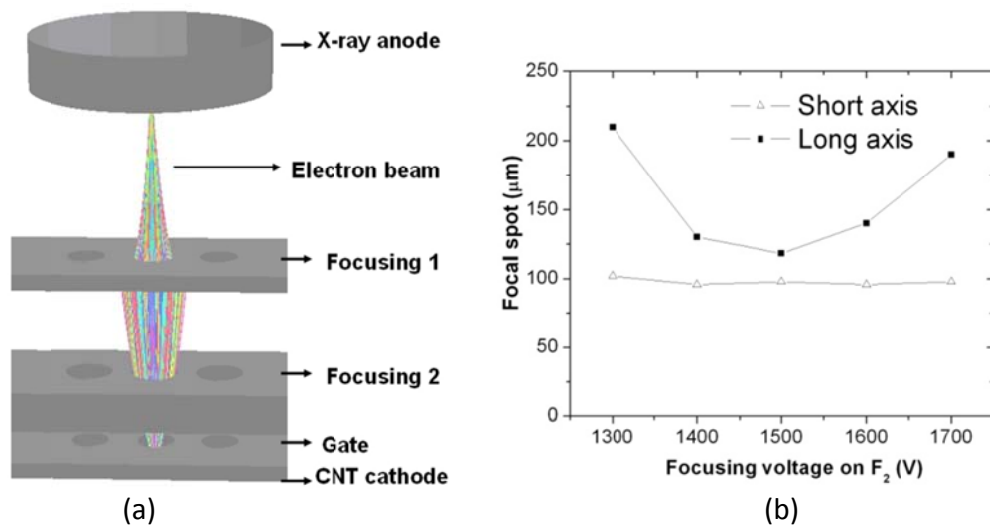


Figure 3-11 (a) The newly designed two-stage Einzel lens for the integrated MBFEX source array. (b) The simulation results of focal spot size as a function of focusing voltage applied on focusing electrode 2.

As the simulation results shown in Figure 3-11(a), the optimized two-stage Einzel focusing lens would provide a demagnification factor of around 5 when electron beam reached the anode surface. Considering the 12° anode tilting angle, 2.35mm × 0.5mm elliptical cathode would provide a desirable 100 μm circular effective focal spot size, as discussed before. Part of the simulation results were demonstrated in Figure 3-11(b). The size of the focal spot, represented by its long and short axes, was clearly a function of applied focusing voltages on the focusing lenses. Based on the simulation results, by

tuning the focusing voltages, it is possible to achieve isotropic focal spot size around 100 μm .

3-3-5 System control circuitry and software interface

In our imaging application, accurate timing control and synchronization of the detector and the 20-beam x-ray sources is essential. A MOSFET based timing control circuitry is made for the purpose. The circuitry couple with a FPGA (field-programmable gate array) data acquisition board (model: NI PCI-7830R) and our homebrew software interface has achieved that.

The control circuitry and its general working principle are showed in Figure 3-12. The MOSFETs (STMicroelectronics, model: STP4N150) used in this circuit have a voltage rating of 1500V. During imaging acquisition mode, gate, focusing 1, focusing 2, and anode electrodes are maintained at constant potentials. Each of the 20 CNT cathodes are connected to the Drain side of the MOSFET, while the Gate sides of which are connected to the FPGA card through a ribbon cable. Sources of these MOSFETs are grounded.

FPGA card is then controlled by the software to send out TTL signals in desirable waveform and sequence. When TTL trigger signal is set at low state, the conduction channel between the source and the drain of the MOSFET is closed. CNT cathode is potential floated relatively to the common ground, thus no electron could be emitted and no x-ray generation. On the other hand, when the TTL trigger signal is set at high

state, the cathode is grounded and forming a complete circuitry. With a constant applied gate voltage, the electric field between gate and cathode then extracts electrons out of the CNT cathode. Electrons are then shaped into desirable beam by the focusing electrodes and striking the anode with x-ray generated. The delay time (between switching of the TTL signal and the conduction channel) of the MOSFET is 35-45 ns, which should not affect our normal imaging application with tens of milliseconds x-ray exposure period.

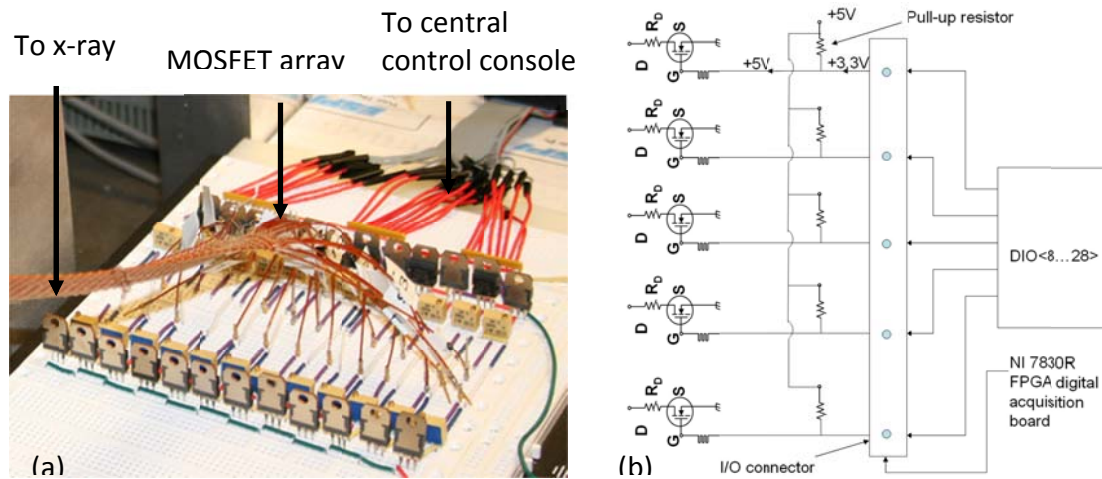


Figure 3-12(a) The MOSFET based control circuitry used for triggering x-ray generation and (b) its working principle

The FPGA card also provides an external trigger signal for the X-ray detector (Hamamatsu C7921A-02) which is used to synchronize its image acquisition cycle with the pulsed x-ray. In external triggering mode, the x-ray detector requires a continuous TTL signal from the ExtTrigg cable, about 450 μ s delay after a rising edge of the TTL signal triggers a frame acquisition. The readout time T_r , the period to acquire a whole

frame, depends on the acquisition mode. For normal and 2 by 2 binning modes, the readout time is 243ms and 122ms, respectively. After acquiring a frame, the detector waits until the next rising edge from the trigger cable to start next frame acquisition. The time between the end of a frame acquisition and the beginning of the next frame acquisition is defined as integration window T_{int} . The readout time T_r and the integration time T_{int} constitute one imaging cycle. During the read out time, the detector cannot grab an image, therefore x-ray pulses should be switched on within the integration window T_{int} only to reduce artifacts.

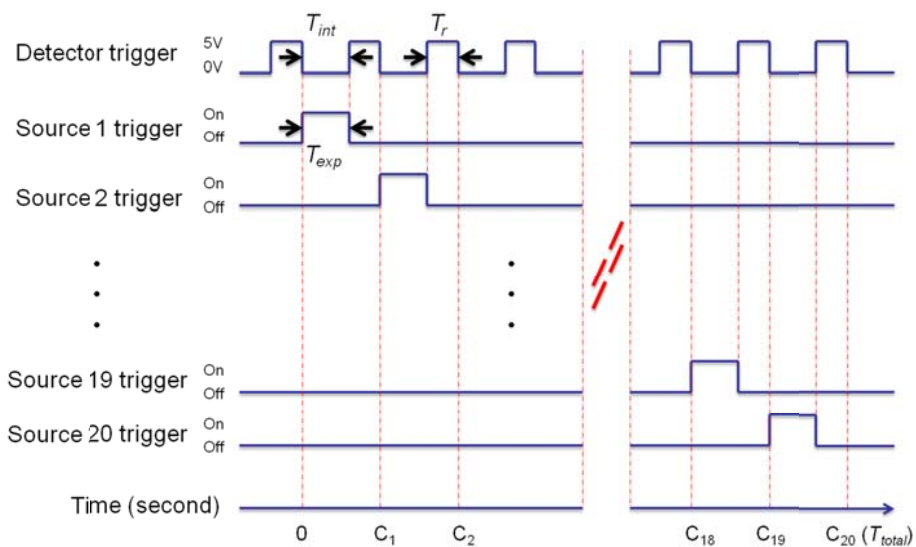
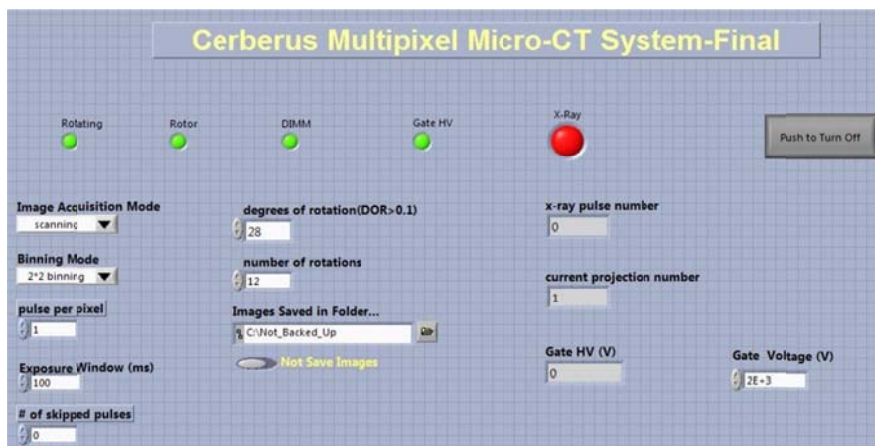


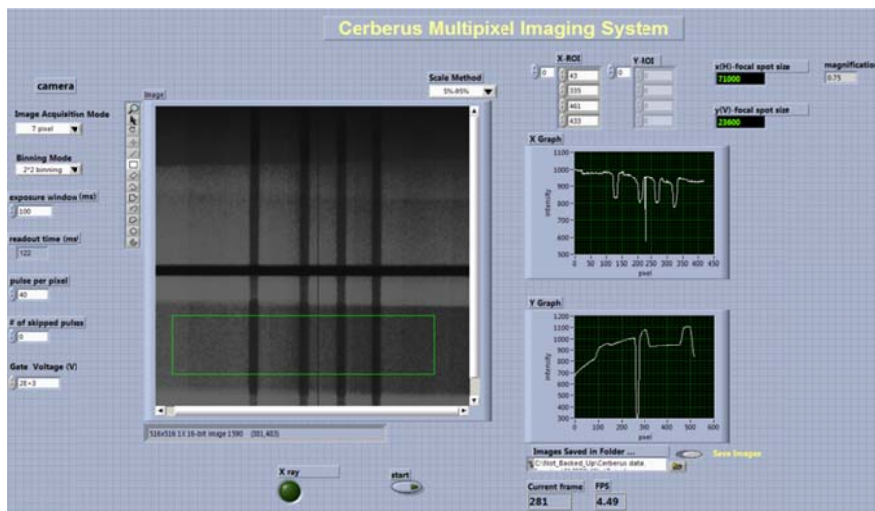
Figure 3-13 Timing diagram for sequential scanning beam generation from the multi-beam micro-CT system

Figure 3-13 shows the timing diagram for sequential scanning beam generation for the multi-beam micro-CT system. In this mode, 20 x-ray pulses are generated one after another, with synchronization of the detector cycle. The FPGA DAQ board can

send up to 56 TTL signals simultaneously with 1 μ s resolution; it enables the multiplexing imaging mode on the system as well. In multiplexing mode, several x-ray beams are switched on simultaneously at one imaging cycle following in a certain pattern. The x-ray beams from different angle irradiate the object at the same time, forming a composite image. The composite image could then be decoded to recover individual images from those beams.



(a)



(b)

Figure 3-14 (a) Software UI in CT mode with integrated rotor control and two imaging modes (b) Software UI in a multiplexing planar imaging mode with a cross-wire phantom. 4 x-ray beams are switched on simultaneously

All the major components, such as x-ray sources, rotary table and detector, in this system are connected and controlled by the homebrew software UI written in LabVIEW as shown in Figure 3-14.

References

1. G.M. Ardran and E. Crooks, *Field emission 350kVp chest x-ray system*. Radiology, 1974: p. 277.
2. H.E. Crooks, J.Sangster, and G.M. Ardran, *The fexitron 848 portabel x-ray apparatus*. Radiology, 1972(456): p. 311.
3. Y. Cheng and O. Zhou, *Field emission from carbon nanotubes*. C.R. Physique, 2003. **4**: p. 1021-1033.
4. H. Sugie, et al., *Carbon nanotubes as electron source in an x-ray tube*. Appl. Phys. Lett., 2001. **78**: p. 2578.
5. G.Z. Yue, et al., *Generation of continuous and pulsed diagnostic imaging x-ray radiation using a carbon-nanotube-based field-emission cathode*. Appl. Phys. Lett., 2002. **81**(2): p. 355.
6. Liu, Z., et al., *Carbon nanotube based microfocus field emission x-ray source for microcomputed tomography*. Applied Physics Letters, 2006. **89**(10): p. 103111.
7. Zhang, J., et al., *Stationary scanning x-ray source based on carbon nanotube field emitters*. Applied Physics Letters, 2005. **86**(18): p. 184104.
8. Bordelon, D.E., et al., *A nanotube based electron microbeam cellular irradiator for radiobiology research*. Review of Scientific Instruments, 2008. **79**(12): p. -.
9. G.N. Hounsfield, *Computerized transverse axial scanning tomography:1. Description of system*. Br J Radiol, 1973. **46**: p. 1016-1022.
10. A.M. Cormack, *Reconstruction of densities from their projections with applications in radiological physics*. Phys. Med. Biol, 1973. **18**: p. 195-207.
11. W.R. Hendee and E.R. Ritenour, *Medical Imaging Physics*. 4th ed. 2002, New York: Wiley-Liss.

12. K. K. Shung, Michael B. Smith, and B. Tsui, *Principles of Medical Imaging*. 1992, San Diego: California: Academic Press, Inc.
13. S.C. Bushong, *Radiologic Science for Technologist*. 1997: Mosby.
14. M.J. Paulus, et al., *High resolution x-ray computed tomography: an emerging tool for small animal cancer research*. *Neoplasia*, 2000. **2**(1-2): p. 62-70.
15. K. Machin and S. Webb, *Cone-beam x-ray microtomography of small specimens*. *Phys. Med. Biol*, 1994. **39**: p. 1639-1657.
16. A. Hirakimoto, *Microfocus X-ray Computed Tomography and It's Industrial Applications*. *ANALYTICAL SCIENCES*, 2001. **17**: p. supplement.
17. M.D. Bentley, et al., *The use of microcomputed tomography to study microvasculature in small rodents*. *AJP Regulatory Integrative Comp Physiol*, 2002. **282**: p. R1267-R1279.
18. E. Maire, et al., *On the application of x-ray microtomography in the field of materials science*. *Adv. Eng. Mater.*, 2001. **3**: p. 539.
19. A. Sasov and D. Van Dyck, *Desktop microscopy and micrtomography*. *Journal of Microscopy*, 1997. **191**: p. 151-158.
20. B.P. Flannery, et al., *Three-dimensional x-ray microtomography*. *Science*, 1987. **237**: p. 1439.
21. C.L. Morgan, *Basic principles of computed tomography*. 1983, Baltimore: University park press.
22. P. Schagen, *Alternatives to thermionic emission*. *Brit. J. Appl. Phys.*, 1965. **16**: p. 293-303.
23. Y. Cheng, et al., *Dynamic X-ray radiography using a carbon nanotube field emission x-ray source*. *Rev. Sci. Inst.*. 2004. **75**: p. 3264.
24. Wang, P., et al. *Design and characterization of a portable field emission microfocus x-ray tube for micro-CT"*. in *SPIE*. 2009.

25. Cao, G., et al., *A dynamic micro-CT scanner based on a carbon nanotube field emission x-ray source*. *Physics in Medicine and Biology*, 2009. **54**(8): p. 2323.
26. Cao, G., et al. *A dynamic micro-CT scanner with a stationary mouse bed using a compact carbon nanotube field emission x-ray tube*. 2009: SPIE.
27. E. Seeram, *Computed tomography*. second ed. 2001: W.B. Saunders.
28. E. K. Fishman and R. B. Jeffrey Jr, *Spiral CT : principles, techniques, and clinical applications*. Second ed. 1998, Philadelphia: Lippincott-Raven.
29. Flohr, T.G., et al., *First performance evaluation of a dual-source CT (DSCT) system*. *European Radiology*, 2006. **16**(2): p. 256-268.
30. R.A. Robb, et al., *High-speed three-dimensional x-ray computed tomography: The Dynamic Spatial Reconstructor*. *Proceedings of the IEEE*, 1983. **71**(3): p. 308.
31. M.J. Lipton, et al., *Cardiac imaging with a high-speed Cine-CT Scanner: preliminary results*. *Radiology*, 1984. **152**(3): p. 579-82.
32. M.A. Speidel, et al., *scanning-beam digital x-ray (SBDX) technology for interventional and diagnostic cardiac angiography*. *Medical Physics*, 2006. **33**(8): p. 2714.
33. T.G. Schmidt, et al., *A prototype table-top inverse-geometry volumetric CT system*. *Medical Physics*, 2006. **33**(6): p. 1867.
34. D.P. Boyd and C. Haugland, *Recent progress in electron beam tomography*. *Med. Imag. Tech.*, 1993. **11**: p. 578-585.
35. E.L. Ritman, R.A. Robb, and L.D. Harris, *Imaging physiological functions: experience with the DSR*. 1985, Philadelphia: Praeger.
36. Seeram, E., *Computed tomography : physical principles, clinical applications, and quality control*. 3rd ed. 2009, St. Louis, Mo.: Saunders/Elsevier. xix, 536 p.
37. S.J. Oh, et al., *Liquid-phase fabrication of patterned carbon nanotube field emission cathodes*. *Appl. Phys. Lett.*, 2004. **87**(19): p. 3738.

38. Calderón-Colón, X. and et al., *A carbon nanotube field emission cathode with high current density and long-term stability*. *Nanotechnology*, 2009. **20**(32): p. 325707.
39. Private communication with Dr. D. Lalush.
40. Qian, X., et al., *Design and characterization of a spatially distributed multibeam field emission x-ray source for stationary digital breast tomosynthesis*. *Medical Physics*, 2009. **36**(10): p. 4389-4399.
41. Frutschy, K., et al. *X-ray multisource for medical imaging*. 2009: SPIE.
42. XinNano Materials Inc., *Unpublished research data*.
43. Zejian Liu, et al., *Carbon nanotube based microfocus field emission x-ray source for microcomputed tomography*. *Appl. Phys. Lett.*, 2006. **89**: p. 103111.

Chapter 4 Preliminary characterization and other imaging applications of multi-beam micro-CT

In previous chapters, I started with the background introduction to both X-ray generation and CNT field emission technology, and then the motivation and design of a multi-beam micro-CT scanner. Through the discussion, we conclude that CNT field emission x-ray source has unique properties which could overcome some of the intrinsic disadvantages of the conventional thermionic source. The electric field driven CNT field emission source provides fast switching time and precise timing control for x-ray imaging. The design flexibility of CNT source has encouraged us to develop imaging systems with novel geometries.

4-1 System Integration

The multi-beam micro-CT (MB μ CT) system is assembled following the design introduced in Chapter 3. The 20-beam integrated CNT field emission source array is fabricated with EPD and carefully processed with vacuum annealing and activation described previously. All the parts in the in-vacuum assembly have been cautiously cleaned and polished for the removal of loose particles and protrusions on the surface.

Both mechanical and electric polishing procedures are applied to the stainless steel parts. The Molybdenum target is carefully polished and cleaned with a special chemical solution. All the metal parts then go through a Hydrogen annealing process for degassing purpose. A tungsten mesh is spot-welded on a stainless steel surface as an electron extraction gate. The mesh needs to be welded while maintaining the surface flatness to avoid shorting between the gate and cathode substrate due to the small spacing.

Then the cathode substrate, glass spacers and three layers of electrodes are stacked together with insulating spacers in between to maintain the spacing required for electron beam focusing based on our simulation. Four ceramic bolts are used to help secure the stacked electrodes. A specially designed multi-beam electronic connection unit is used to connect individual CNT cathodes to the external MOSFET based control circuit through a multi-pin feedthrough. As shown in Figure 4-1(a), 20 spring-loaded pins are installed in a ceramic bar. The ceramic bar has 20 holes matching the spacing of those silver conducting lines on which the elliptical CNT cathodes are deposited. The pins are installed in the matching holes so that each of the pin sits right on top of a cathode line. When the connection unit is fastened to the glass cathode substrate by 2 ceramic bolts at two ends, all 20 pins would be pressed down and form tight contact with the cathode lines. The connection unit is then wired to the multipin feedthrough via a UHV rated ribbon cable as shown in Figure 4-1(b). At this point, 20 CNT cathodes become individually addressable through the wiring between the connection unit and external circuit.

A mobile turbo pumping station is used to maintain the vacuum environment for the x-ray application. The vacuum system is baked at 250°C for at least 3 days to remove water vapor and other gas particles from the parts. 10^{-8} - 10^{-9} Torr vacuum is achieved stably for the system.

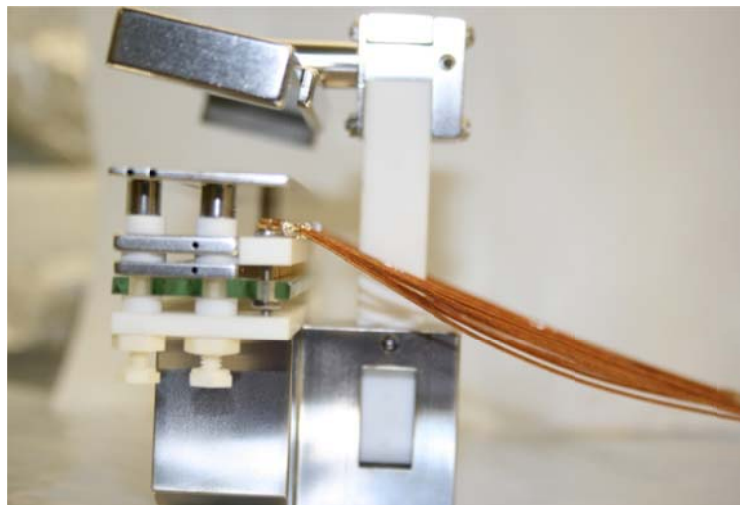
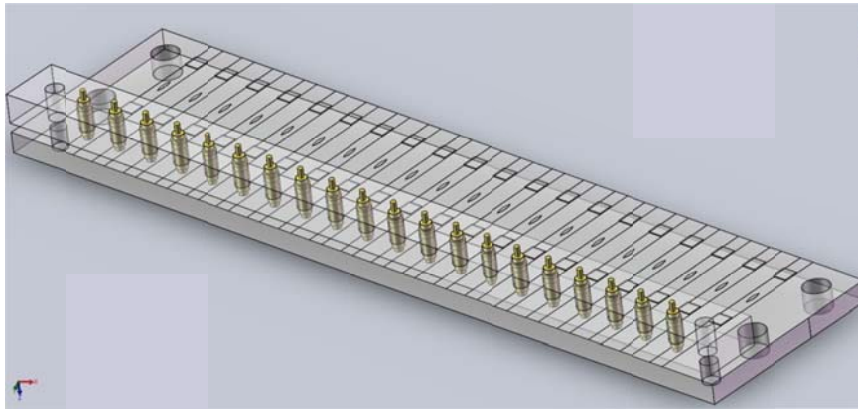


Figure 4-1 (a) specially designed multi-pin connection unit for cathode individual control (b) the connection unit is connected to the external circuit via a UHV rate ribbon cable

A customized 3-axis rotation stage is used for the object. The x-ray detector is then mounted on a 2-axis translation stage for more flexibility. Figure 4-2 demonstrates the assembled multi-beam micro-CT system.

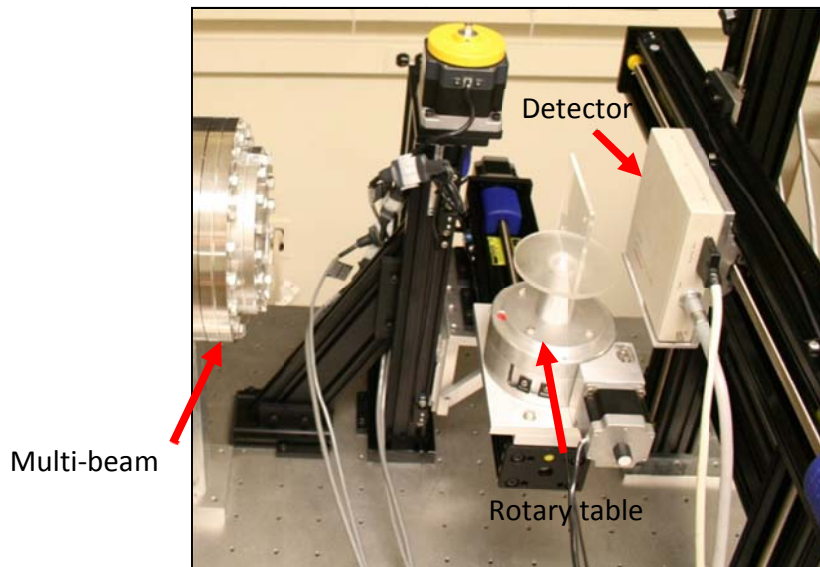
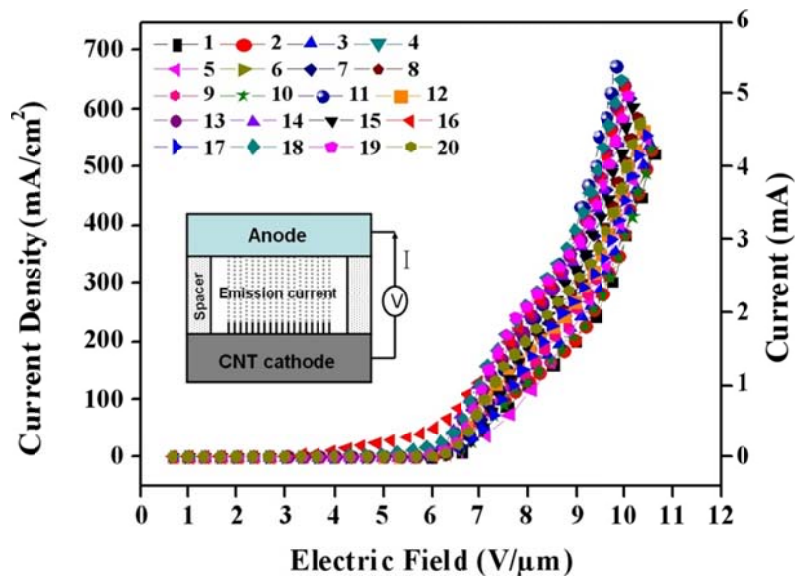


Figure 4-2 The overview of the assembled MB μ CT system.

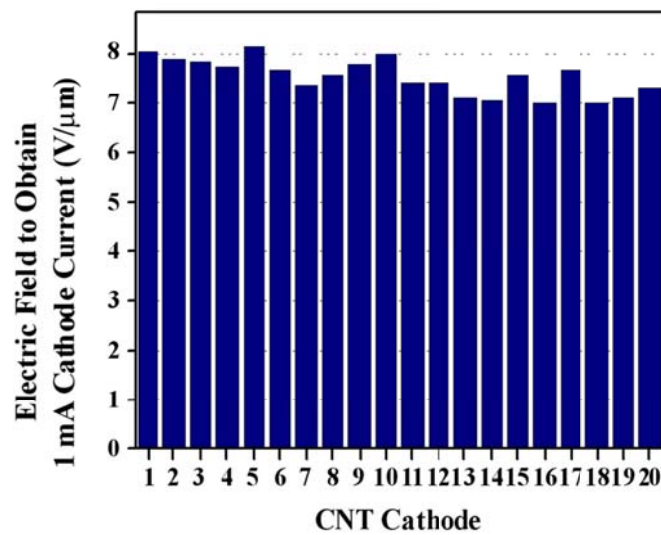
4-2 Preliminary characterization

In order to prepare the multi-beam system for the potential imaging application, a few preliminary characterizations have been carried out and results being shown in the following sections.

4-2-1 MBFEX field emission performance and current regulation



(a)



(b)

Figure 4-3 (a) Measured field emission current as a function of applied electrical field from 20 CNT cathodes deposited on the glass substrate. The measurement was done under standard parallel plate geometry (inset). (b) Required electric fields to obtain 1 mA cathode current from all 20 CNT cathodes.

In Figure 4-3(a), field emission results from all 20 cathodes measured in a typical diode emission mode were demonstrated in a standard parallel plate configuration (Figure 4-3(a) inset). The threshold extraction electric fields to obtain 1 mA CNT cathode

current is $7.5 \pm 0.4 \text{ V}/\mu\text{m}$. The much improved uniformity of field emission property (with roughly 5% variation of threshold electric field) was largely attributed to the fact that all of the CNT emitting cathodes were deposited on the same cathode substrate and the fabrication procedure was then essentially identical for all the 20 CNT cathodes. Even under well controlled cathode fabrication conditions, the cathodes on the as-fabricated cathode array would still have some differences in field emission performance more or less, thus different gate voltages were needed to achieve uniform emission currents from individual cathodes. A ballast resistor based compensation loop was introduced into the field emission circuit to minimize the variation and achieve uniform field emission properties from all the cathodes[1]. An adjustable serial resistor (0-10M Ω range) is integrated in the circuit between individual cathode and the common ground. A customized resistor array is built which could be used as a detachable module of the entire control circuit, as shown in Figure 4-4.

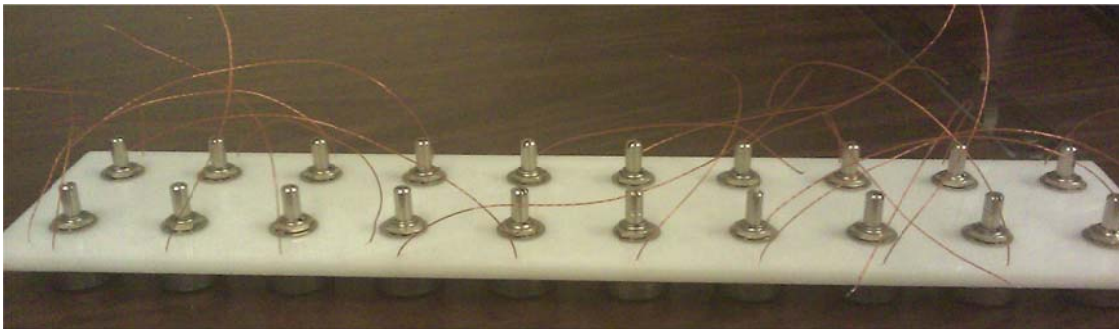


Figure 4-4 The adjustable serial resistor array is used to modulate emission currents from different cathodes and increase the uniformity of the generated x-ray flux.

Before the imaging application, an initial current screening result is acquired. Field emission performances (I-V curve) from multiple cathodes is measured and recorded with LabVIEW software shown in Figure 4-5 .

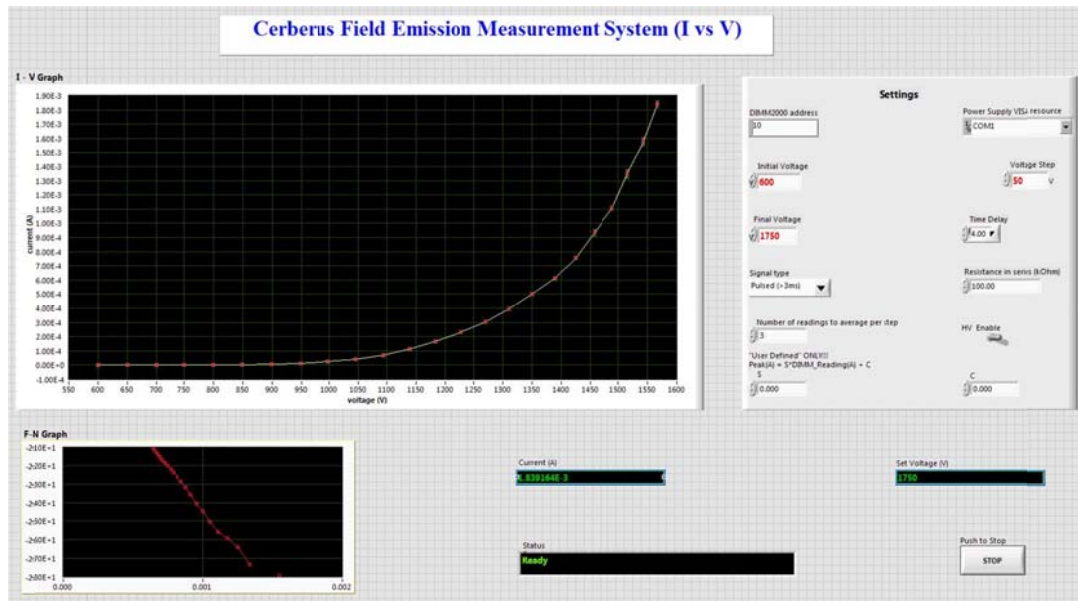


Figure 4-5 Homebrew field emission measurement program for multi-beam micro-CT system. User can switch on different beams and generate different waveform of x-ray pulses within the program. It could also record the data and display the I-V curve and F-N plot in real time.

After the initial screening, a target current level and gate voltage is chosen. The criterion for the target value is such that most of the beam could reach the value with only minor adjustments. Then the serial adjustable resistors are manually conditioned to help regulate currents to the target current value. The common gate voltage needs to be maintained at the target value during this adjustment.

Figure 4-6(a) showed a relatively large variance in field emission performances from a subset of CNT cathodes before the resistor adjustment was applied, while Figure

4-6(b) depicted a much narrower distribution in emission currents at certain gate voltage after the current regulation.

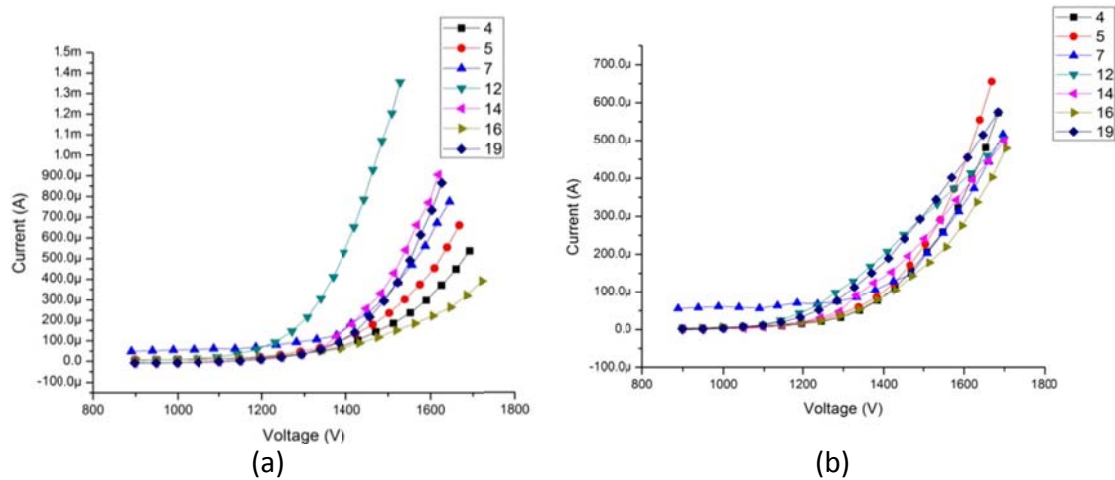


Figure 4-6 (a) Initial spread of field emission I-V curves from different CNT field emission cathodes. (b) Relative uniform field emission characteristics from the same batch of CNT cathodes after applying a ballast resistor based compensation loop.

4-2-2 Control circuit timing test

In the control circuit, a FPGA data acquisition board is responsible for the synchronization of detector external trigger signal and the x-ray pulses. During imaging application, the LabVIEW software sends command based to the installed FPGA card and opens up several channels of Digital Input/Output (DIO) depending on the type of imaging mode. Then TTL pulses are generated through DIOs and transmitted to a connection block used to communicate between the external MOSFET circuit and FPGA card. MOSFETs get corresponding TTL signals and start to switch the CNT source and generate x-ray beams in the desirable pattern.

The timing scheme discussed in Chapter 3 requires accurate synchronization between detector and x-ray source, so that the x-ray exposure at each frame only falls into the detector integration window.

A Tektronix TDS3014B digital 4-channel oscilloscope is used to verify the timing control precision of the MOSFET based circuitry from different channels. Results are shown in Figure 4-7.

Figure 4-7(a) illustrates the synchronization between detector integration window and two x-ray pulsed signals. An imaging cycle of 160 ms is defined here, with 60ms in integration time and 100ms for detector read. Channel 1 and 2 represents x-ray trigger while channel 3 is the detector external trigger. The diagram clearly shows that the x-ray pluses are only switched on (TTL high state) when the falling edge of the detector TTL trigger signal comes, indicating the completion of detector read-out in the previous imaging cycle.

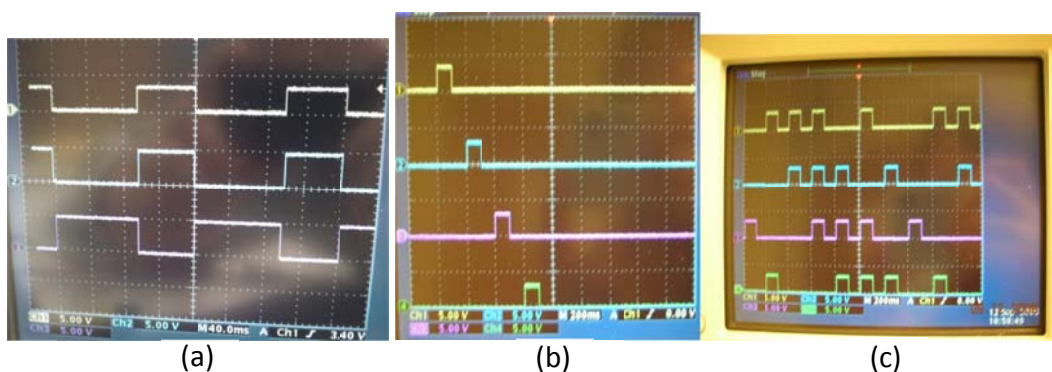


Figure 4-7 (a) timing diagram showing 2 x-ray triggers (channel 1 and 2) synchronize precisely with the detector integration window (channel 3). (b) Channel 1-4 shows the triggers for first 4 x-ray beams are switched on sequentially. (c) Channel 1-4 shows the first 4 x-ray beams in a multiplexing scanning mode, clearly multiple beams are switched on simultaneously in a single imaging cycle.

Figure 4-7(b) represents a scanning beam generation scenario. Channels 1 to 4 indicate the first 4 x-ray beams in the 20-beam source respectively. A 100ms, 50% duty cycle pulse is programmed to generate from beam 1 to 20 one after another without interruption.

A multiplexing scanning scheme is showed in Figure 4-7(c), in which channel 1-4 still represent the first 4 x-ray beams. In such timing scheme, one or more x-ray beams are switched on simultaneously within one imaging cycle based on a certain mathematical sequence. From Figure 4-7(c), we can conclude that our multi-beam micro-CT system is capable of generating multiplexing beams.

Overall our MOSFET based controlling circuit has enabled precise synchronization between x-ray pulse generation and detector imaging cycle. With this mechanism, our multi-beam micro-CT scanner become a more powerful tool and test platform for potential imaging applications.

4-2-3 Focal spot size characterization

In our system design phase, a 100 μm effective focal spot size is targeted for the CNT MBFEX in order to provide sufficient system resolving power for micro-CT imaging. As a result of its multi-beam geometry, uniform focal spot size among different beams is much appreciated for better image quality.

Following the European standard EN12543-5[2] a customized cross-wire phantom (1 mm tungsten wires) was used for our focal spot measurement. The focal

spot size of the x-ray tube was obtained based on the penumbra of the cross-wire phantom image along two orthogonal directions. The electrical potential applied to the focusing electrodes was adjusted to achieve optimal focusing voltage conditions. As shown in Figure 4-8(a), LabVIEW program was compiled to automatically calculate the focal spot size from the captured cross-wire phantom image. Magnification factor in this experiment was about 7. Based on the simulation results showed previously, several focal spot size measurements were taken with respect to different electric potential on both focusing electrodes. We could reach optimized focal spot sizes at about $107\pm 5\ \mu\text{m}$ in vertical direction and $118\pm 6\ \mu\text{m}$ in horizontal direction. Here the focal spot size in vertical direction originates from the long axis of elliptical cathode, while the focal spot size in horizontal direction is from the short axis. The electric potentials to achieve such optimal focal spot size were around $1700\pm 88\ \text{V}$ on first focusing electrode (focusing electrode 1), and $2150\pm 71\ \text{V}$ on the top focusing electrode (focusing electrode 2). The small variation of focusing voltages required to achieve optimal focal size of different cathodes were primarily due to the slightly varied cathode assembly characteristics. The experimental results generally agreed with the simulation results showed in Chapter 3. But we also noticed the offset of focusing voltages between simulation and experimental results. Further analysis indicated that it was mainly due to the simplified computer model used for simulation and slightly different boundary conditions applied in the model.

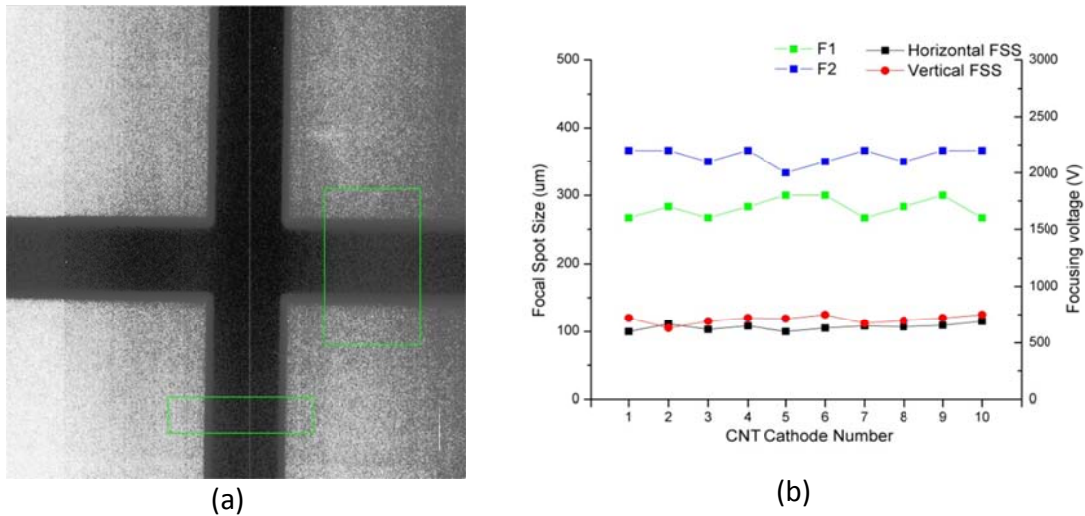


Figure 4-8 (a) The LabVIEW control software UI in a focal spot size measurement, area in green line stands for the area chosen for line profile and FSS calculation. A standard Tungsten cross wire phantom was used for the focal spot measurement. **(b)** The experimentally measured optimal focal spot sizes of different emitting cathodes under their corresponding focusing voltage settings. Focal spot sizes around $100\mu\text{m} \times 100\mu\text{m}$ were achievable for all the emitting cathodes by tuning the corresponding focusing voltages.

4-3 Mouse imaging with the multi-beam micro-CT system

To demonstrate the feasibility of the novel imaging geometry, we have done some pilot studies with this new imaging system. Our first attempt is a demonstration of multi-beam CT scanning scheme with a mouse carcass.

LabView based control software (Figure 4-9 shows the graphic user interface) has been developed to control the x-ray generation of the multi-beam x-ray source array. It also synchronizes the x-ray source array, rotary table, and x-ray detector for imaging acquisition during CT scan. In order to generate a scanning x-ray beam, the LabView software controls an FPGA board (National Instruments PCI-7830R) to generate TTL signals from multiple digital I/Os with a certain sequence. The generated TTL signal

transmits to the circuitry board where the MOSFET array is connected to individual CNT field emission pixel inside the vacuum chamber via the multipin feedthrough. The gate of each MOSFET corresponds to a specific digital I/O. Therefore, when a 5V TTL signal from a certain digital I/O hits the gate of MOSFET, it is switched on, forming a complete electric circuit with the corresponding pixel.

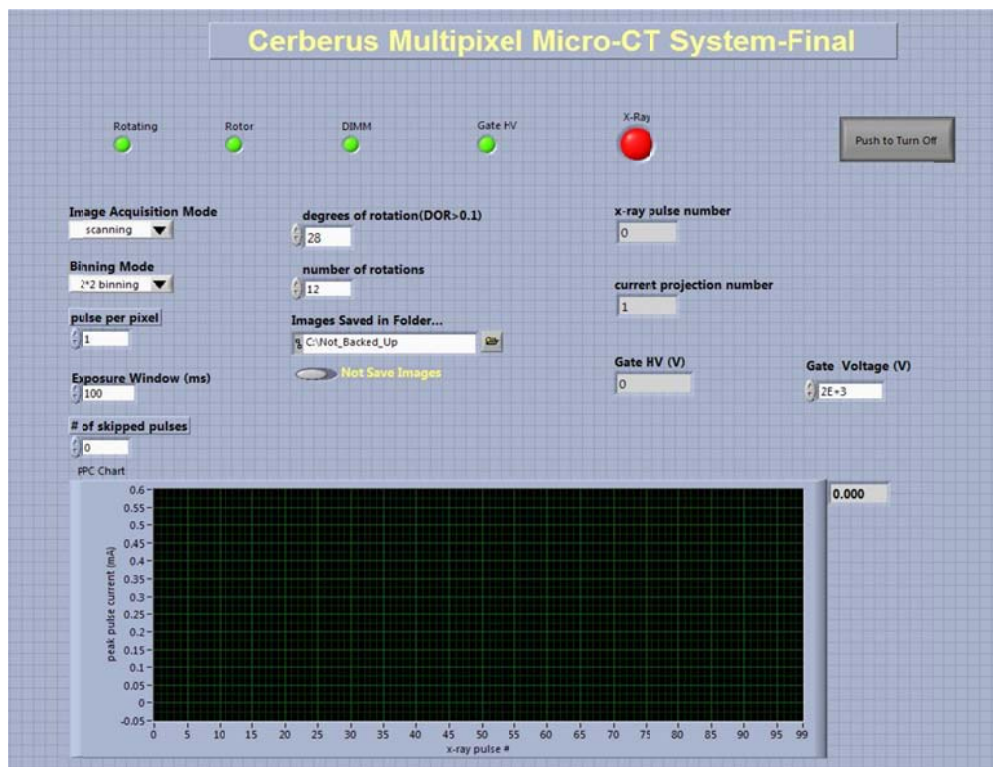


Figure 4-9 The LabView based control software for the prototype MB μ CT scanner.

In Figure 4-10, we illustrated the basic CT imaging flow chart for the MB μ CT imaging system. Following our micro-CT scanning protocol, each CNT field emission pixel will be sequentially triggered to generate an x-ray beam and a scanning beam will irradiate the imaging object from different projection angles. After the sequential

scanning from all 20 x-ray pixels, the object will be rotated for about 28° to prepare for next scan. It only takes 12 rotation steps to cover the entire 360° angle and to be able to supply enough data for tomographic reconstruction.

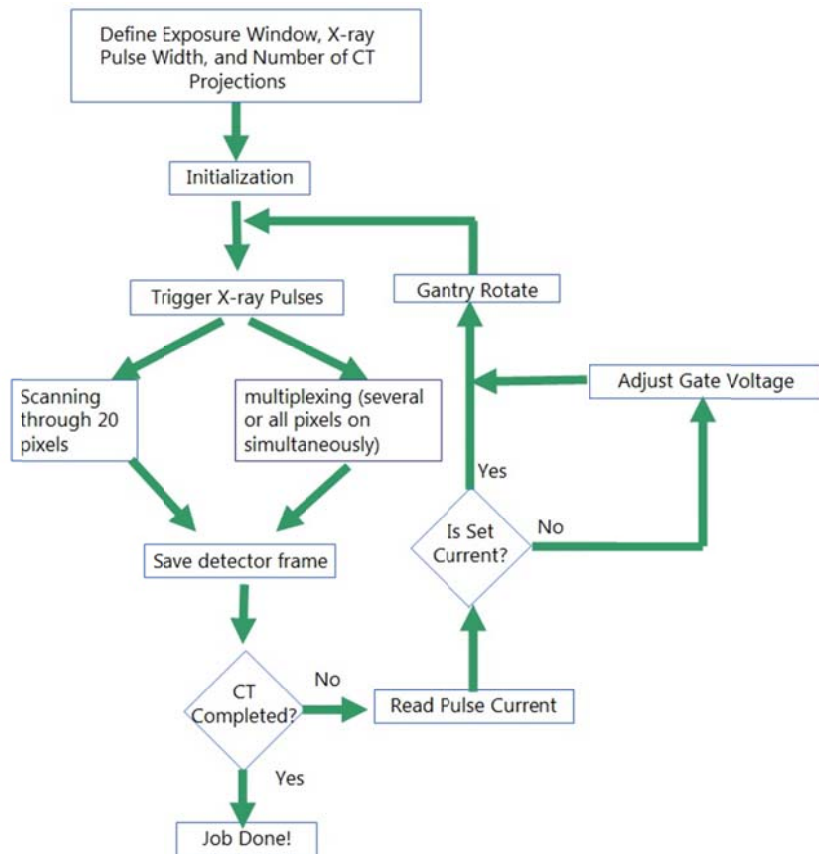


Figure 4-10 Image acquisition flow chart for the MB μ CT imaging system.

In order to test the imaging capability of this prototype system, a dead mouse was scanned using the 20-beam MB μ CT scanner. The overall imaging configuration used for this particular testing was slightly different with our standard CT imaging protocol due to a smaller x-ray detector (Hamamatsu C7921CA) used for this particular

experiment. In order to make sure that the detector was able to capture all the projection images generated by the multi-beam source array, we reduced the distance between the imaging object (mouse) and x-ray detector to 3 cm. The SOD was set at 17.5 cm and the mouse was aligned with central line of the 20-beam x-ray source array. The SDD was 20.5 cm for the scanning.

In order to acquire the entire set of projection images, the mouse was rotated by a total number of 12 times with 28° per step. At each fixed mouse position, the 20-beam x-ray source array was electronically triggered to generate a scanning x-ray beam and the mouse was irradiated from 20 different viewing angles sequentially. The x-ray area detector running at 8 FPS at 2×2 binning mode with $200\mu\text{m} \times 200\mu\text{m}$ pixel size was used to record the image. It was synchronized with the field emission triggering signal and a total of 20 projection images were recorded. The raw data were processed using a MATLAB based program written in house. During the CT scan, the anode voltage V_a was fixed at 40 kV. The gate voltage was set at 2 kV while the focusing voltage at 1.5 kV based on the results of the field emission measurements done previously.

In Figure 4-11, we showed three sets of projection images generated by the CNT x-ray pixel 1, 6, 13 and 16. Each set of images was corresponding to a certain rotation position of the mouse (0° , 112° , and 224° respectively). The projection images demonstrated good bone delineation and soft tissue contrast. The images also showed reasonable spatial resolution of the MB μ CT scanner, although it was partially because of the short distance between mouse and x-ray detector (low magnification).

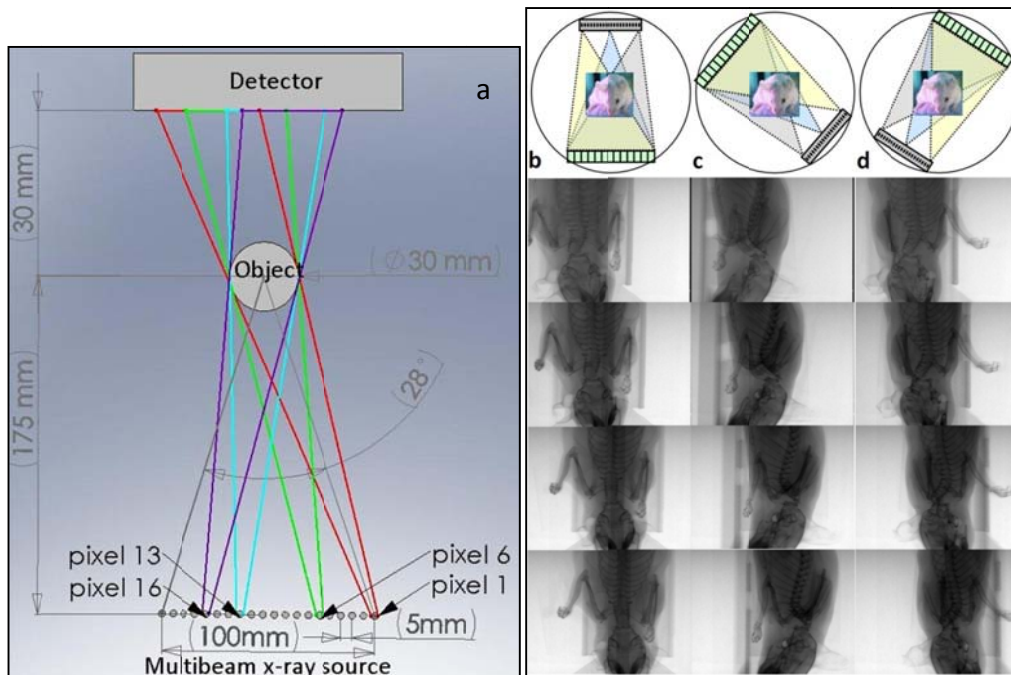


Figure 4-11 Projection images recorded at 0° (a), 112° (b), and 224° (c). (d) Illustration of the difference in projection angle from 4 pixels. Each image in individual group demonstrate different projection angle

We have completed a testing CT scan of a mouse using the prototype MBμCT scanner. However we fully realized the complexity of this multi-beam system. The current imaging system still needs to be refined and further studied in a lot of ways. For example, the geometry of the imaging system needs to be carefully calibrated prior to any CT reconstruction. Unlike conventional CT scanners with circular scanning path, the MBμCT scanner essentially has a polygon shape scanning trajectory. In order to accommodate this special scanning geometry, the corresponding CT reconstruction algorithm needs to be modified. For example, the image generated by different x-ray pixel will have different SOD and incident angle. Those need to be considered and corrected in the reconstruction process. The reconstruction program used for this

MB μ CT scanner is currently under development. Some of the results from our collaborators have been published recently[3].

Our current scanning protocol has an angular step at about 2° for a CT scan. The higher angular sampling density, for example angular step at 1° can be easily achieved by performing two consecutive scans with 1° offset for the second scan. In this case, it will take 20 steps instead of 10 steps to get a 360° full scan.

The reduction of scanning time due to fewer rotations has been tested in our experiment. Based on our current system with a Velmex 4800 series rotary table at rotation speed of 25°/s, we estimated that for a typical scan of 400 projection images, the time spent on rotation can be reduced from 60s to about 15s. We calculated the projected scanning time for the MB μ CT scanner according to its scanning configuration and the maximum tube current generated by the CNT field emission cathode (10mA based on the cathode size). On the other hand, the scanning speed of the current prototype system was also limited by its slow x-ray detector readout cycle (8 FPS at 2×2 binning). Once equipped with a high speed x-ray detector, it should be able to reach a scanning time around 20 seconds (including 15 seconds needed for 20 rotations). The future development of a full scale stationary MB μ CT will allow a scan time around 5 seconds attributed to its ideal motion-free feature.

4-4 Multiplexing imaging investigation

Upon reaching the mechanical limit of gantry rotation speed, novel geometry for CT scanner is needed to surpass the bottleneck and achieve higher throughput.

Previously we have introduced the design and preliminary characterization of a multi-beam micro-CT scanner. With its multi-source setup, other novel imaging methodology naturally became a very interesting topic to investigate.

4-4-1 Multiplexing with CNT field emission x-ray

Multiplexing/demultiplexing has been widely used in telecommunication industry for more than 3 decades. By definition, multiplexing (MUXing) is a process where multiple analog or digital signal streams are combined into one mixed stream over a shared transmitting media; on the other hand, demultiplexing (DEMUXing) is the reverse process to separate superimposed signal streams out. This concept has not been introduced to radiography until the emergence of our distributed x-ray source array based on carbon nanotube field emission technology. With our technology, individual x-ray emitting pixels are easily deposited in any desired geometry, forming a multi-beam x-ray source array which would be digitally controlled. Field emission x-ray source has a natural advantage in being digitalized as a result of its instantaneous response to the extraction electric field. Electrons would emit instantaneously upon the appearance of extraction field, and emission would stop once the electric field is removed. Therefore, it's convenient for us to use digital pulse train to trigger electron emission from the multi-beam source to generate x-ray pulses in desired pattern. Also, the x-ray beams coming out from different emitting pixels will penetrate the object in iso-center with

different angles, thus information of the object at different projection angles can be acquired on detector, similar to conventional CT scanner. The difference is that mechanical movement is not needed to acquire projection images from different angles. The transition from mechanical to electronic greatly reduced the amount of time needed for enough angular sampling.

To further improve the data acquisition speed, multiplexing provides a possible solution where images from multiple angles could be acquired simultaneously and then separated by DEMUXing afterwards. There are many types of MUXing such as frequency-division MUXing (FDM), time-division multiplexing (TDM). We have investigated FDM in previous research where the signals are modulated by different frequencies[4]. In this study we mainly focus on binary multiplexing where the signals are modulated by a series of sequence determined by Hadamard code showed as Figure 4-12. The “1” status corresponds to x-ray beam on, while the “0” status corresponds to x-ray beam off. In each recorded time frame, there would be 4 x-ray beams on simultaneously and a superimposed projection image of the object being acquired by the detector. After the entire 7 sequences, projections from 7 different beams, essentially 7 different angles would be recovered, or DEMUXed. We have verified that with N beams in a source array, binary MUXing would have a factor of $(N+1)/2$ gain in speed compared to sequential mode given the constant dose case.[5]

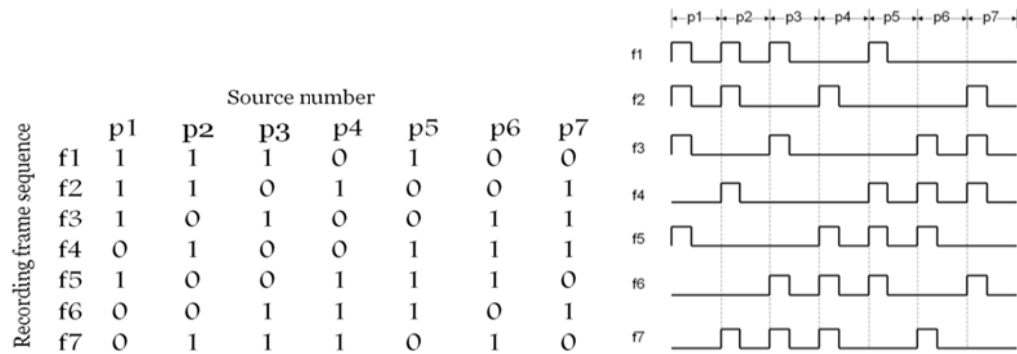


Figure 4-12 seven element Hadarmad coding matrix and corresponding pulse generation sequence in the right.

4-4-2 Noise characteristic in the multi-beam micro-CT system

The major concern for MUXing is noise propagation from multiple channels during the image superimposition and separation. Advantages in speed are gained at compensation of the loss in signal-to-noise ratio generally. It is then very important to study the relative ratio between the gain and the loss.

Simply speaking the noise on an x-ray imaging system comprises of two major contributors: quantum noise from the x-ray photons and electronic noise from the electronic components. Electronic noise could be further categorized in a couple of sub-groups such as pixel dark current noise, pixel reset noise (kT/C), amplifier noise and fixed-pattern noise et al[6, 7]. The major source of electronic noise is the dark current generated in detector electric circuitry, therefore electronic noise is mainly related to the detector integration time. With a fixed image read-out time, electronic noise could be modeled as a constant component, while the quantum noise could be considered as

a proportional component as x-ray photons hitting on the detector obey Poisson distribution. From earlier simulation[8], in the mixed noise scenario where proportional noise and constant noise co-exist, it is believed that the performance of MUXing compared to sequential imaging relates to the ratio between these two types of noise, denoted as P. Mathematical analysis for Hadamard encoding showed that, for a proportional noise model (i.e. Poisson), it would generally not perform as well as a sequential mode; while on the other hand, in a constant noise scenario (i.e. only constant background noise on detector), multiplexing could outperform sequential mode. The critical point for any N at which the Hadamard S-matrix exists $p = \frac{N-1}{N+1}$, N being the number of beams in the array. When the P ratio is higher than this critical point, sequential mode performs better than Hadamard multiplexing; whereas at a smaller P value compared to the critical point, Hadamard multiplexing could outperform sequential mode.

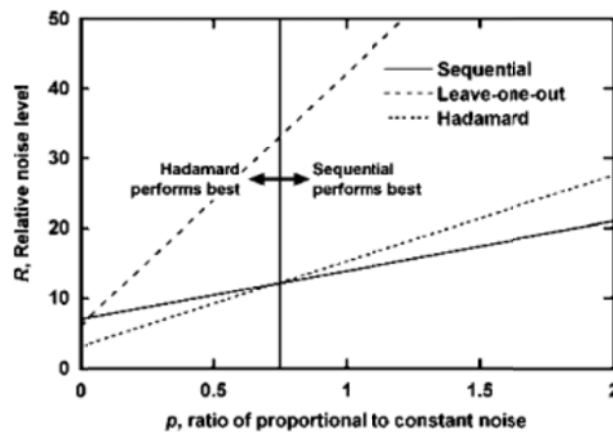


Figure 4-13 Relative noise level versus proportional-to-constant noise ratio in a seven-source system from simulation results.[8]

In our study, seven x-ray beams are used, thus the crossover point is at p value of 0.75.[8] The key information needed in our study is the relative relationship between electronic noise and quantum noise in a specific setting.

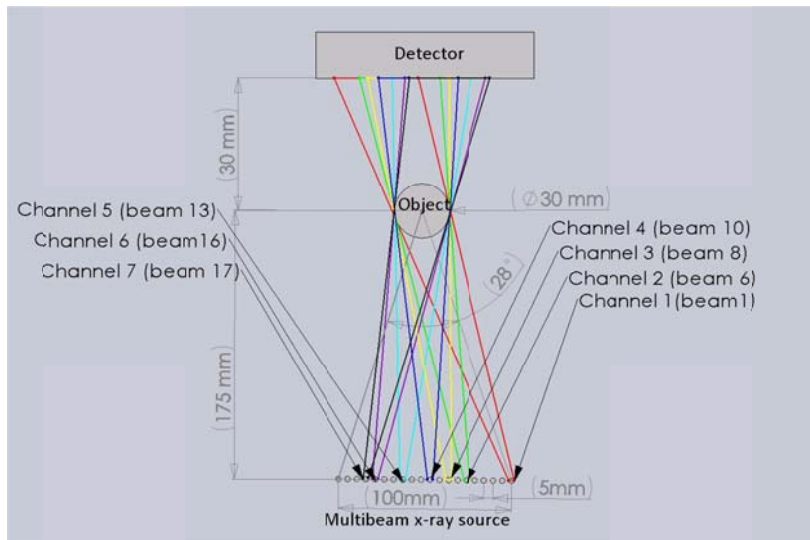


Figure 4-14 illustration of the experimental geometry settings for 7-beam binary multiplexing

We took advantage of our innovative multi-beam micro-CT system based on carbon nanotube field emission technology. Imaging geometry used in this pilot study is as follow: the central source-to-object distance (SOD) is 17.5cm. For the linear array, the actual distance between the x-ray focal point and the object varies from beam to beam. The source-to-detector distance (SDD) was set to 20.5 cm to achieve a system magnification factor of 1.2. The details for this experimental setting are depicted in Figure 4-14. Beam 1, 6, 8, 10, 13, 16 and 17 were chosen based on the field emission measurements as illustrated in Figure 4-15.

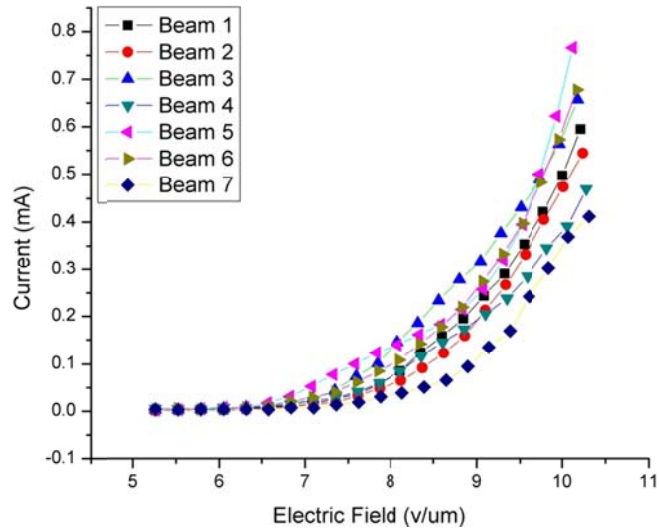


Figure 4-15 Field emission measurements for the chosen 7 beams

In the central console, a LabVIEW based software controls the generation of the pulse signal and also retrieves all the data collected by the entire set of instruments. The planar imaging acquisition software controls the digital pulse generation in two different modes: sequential, binary multiplexing. When in sequential mode, the software switches on each digital I/O sequentially from 1 to 20 and generates a TTL signal based on the required x-ray exposure window and the detector read-out cycle. In binary multiplexing mode, several digital I/Os are switched on simultaneously in a certain sequence based on (1 status) the Hardamard matrix, while the rest of them remain off (0 status).

A mouse carcass is scanned with the geometry mentioned above in multiplexing mode in order to test the feasibility. Current from each of the 7 beams are regulated at about 0.5mA with a constant gate voltage of 2000 V. At 30 kV anode voltage, 100 ms of

x-ray exposure from the beam switched on at each multiplexing scenario is used to generate one composite multiplexed image. Essentially the object is irradiated 4 times from each of the 7 beams in order to acquire the 7 multiplexed images. To have a rather fair comparison, we used 4 exposures per view in the sequential mode.

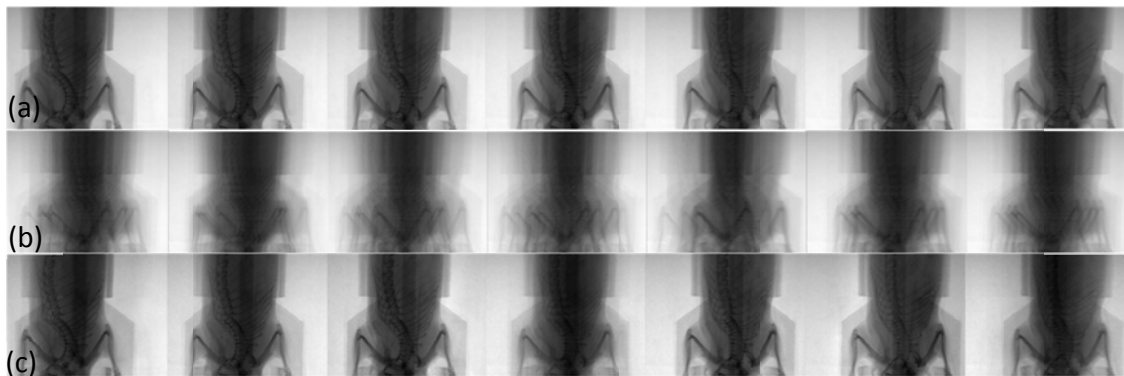


Figure 4-16 7-beam binary multiplexing with a mouse carcass with the geometry introduced above. (a) Sequential Projection images from 7 X-ray beams from MB μ CT, the horizontal translation of mouse body clearly depicts the difference in projection angles from 7 beams (b) Superimposed projection images from 4 beams simultaneously illuminating the same mouse based on a certain sequence (C) Demultiplexed images from the decoding of the superimposed images

After the data acquisition, a MATLAB program is used to demultiplex the composite images and recover the information originating from the 7 individual beams. The results are shown in Figure 4-16.

The experiment essentially confirms that the scanning scheme for binary multiplexing works with the multi-beam micro-CT system. With constant dose mode, in this case 400ms X-ray exposure in each beam, 7-beam binary multiplexing scheme can finish a data set 4 times faster than the sequential mode.

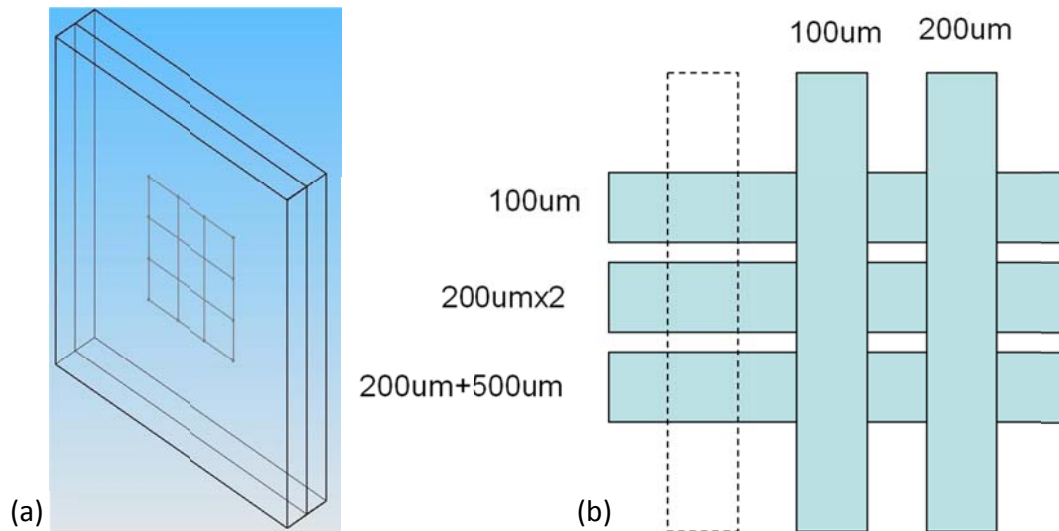


Figure 4-17 (a) the customized signal-to-noise ratio phantom consists of two acrylic plates and an insert of crossed aluminum foil (b) the crossed aluminum foil insert. With different folds of aluminum foil, the area is divided into several smaller regions with different x-ray attenuation.

We then carried on another experiment in a more quantitative perspective. To ease the analysis complexity, a simple phantom designated for SNR measurement was built with two $12\text{ cm} \times 12\text{ cm} \times 0.5\text{ cm}$ acrylic plates and a crossed aluminum foil insert as shown in Figure 4-17. Different folds of aluminum foil provided different attenuation across the entire FOV, while maintaining uniformity in smaller regions. Then we used a 1mm tungsten cross-wire phantom as an indicator of different projection angles.

Since detector constant noise is related to its frame rate, therefore, we kept a constant 0.2 fps throughout the experiment. The x-ray exposure time varied from 50ms to 800ms with 25ms step. 2480 frames of dark images were acquired in the same fashion where there was no x-ray exposure. 4 exposures from each of the 7 beams with

30keV x-ray were captured for further analysis. There were totally 28 groups of data sets with 31 projection images in each set reflecting variation in x-ray exposure time.

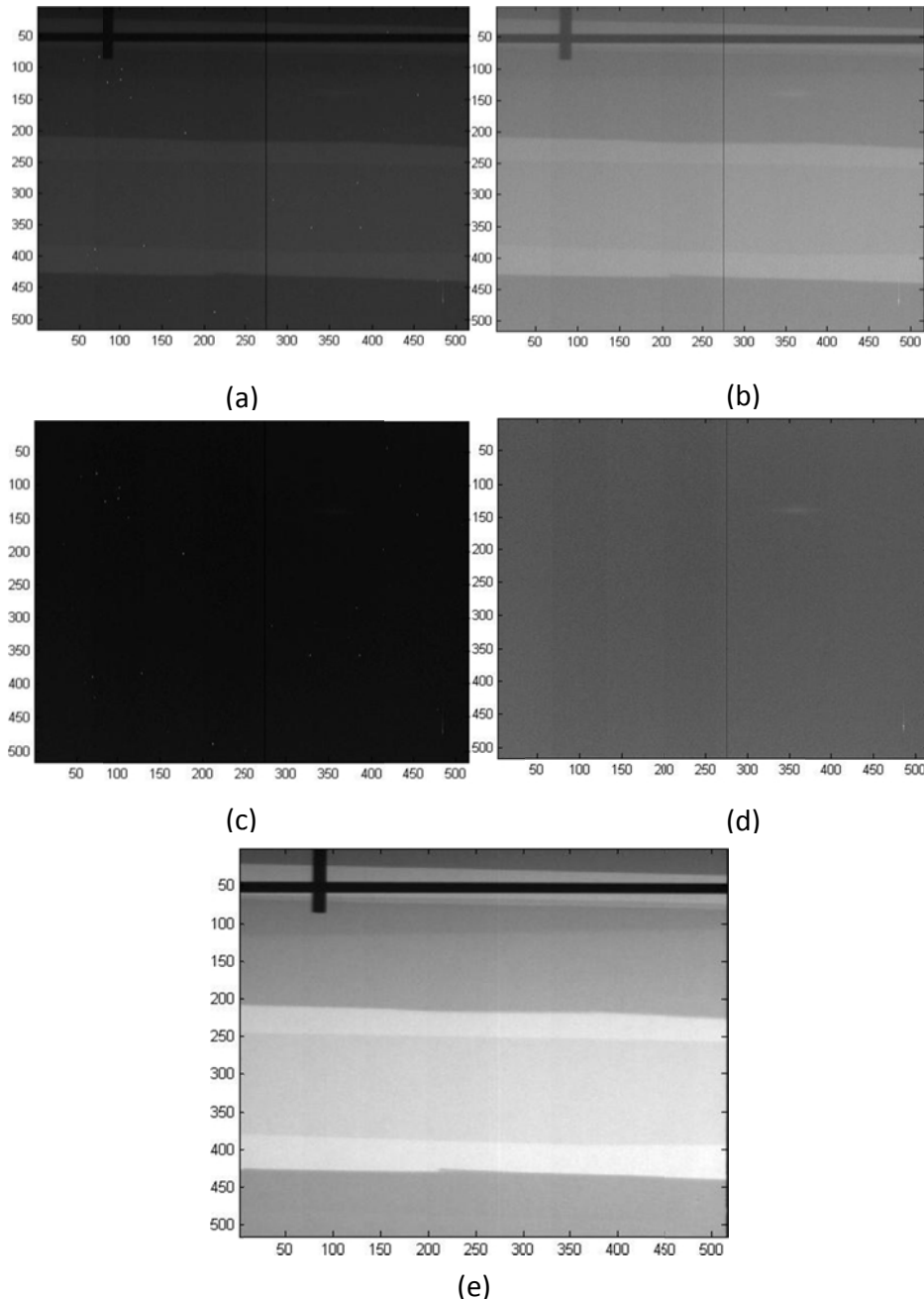


Figure 4-18 illustration of the implication of dark frame subtraction. 5-a is raw image with phantom in the FOV, while 5-b is the raw dark image. There were quite a few bright spots and a dead line in the FOV. After correction, 5-a and 5-b became 5-c and 5-d respectively, with obvious reduction of bright pixels. Then we subtracted 5-d from 5-c and have our final image of 5-e

During the quantitative analysis, we noticed that the intrinsic fluctuation on this specific detector is relatively large and there were quite a few non-uniformities such as bright spots and dead pixels with intensities varying in temporal domain as well, which would greatly alter the analysis results. In order to fully utilize the acquired data, a correction algorithm was introduced to remove those. A threshold value was carefully set to exclude any abnormal leap or drop in intensity such as bright spots and dead pixels et al over the entire FOV. Both dark and raw images were corrected with the same algorithm. Then average of the entire dark image data was taken and used as a reference image which then was subtracted from each raw image after correction. A 30 pixel \times 30 pixel region was chosen within uniform attenuated area in each projection view and use it as the ROI for analysis. The dark frame correction and subtraction process is shown in Figure 4-18.

4-4-3 Results and Discussion

We noticed that some noise sources are independent of the signal level. They are: the output amplifier noise, camera noise and clock noise. They can be combined in a single equivalent noise source. The level of this source is called readout noise, and is a characteristic of the camera. It can be expressed in electrons, or in the camera output units (ADU). Here we set up a simple model to investigate the noise of a pixel value on CMOS detector. The read-out value from a pixel is:

$$s_r = s_0 + G(S_d + S_p) \quad \text{Equation 4-1}$$

Where s_r is the total signal we can read-out from the detector in ADU, s_0 is a fixed bias introduced by detector electronics, S_d is the number of dark electrons and S_p is the number of x-ray photons hitting on the detector after the attenuation of the object. G is a coefficient describing how many ADUs/electron the camera produces, for convenience we simply call it gain.

As described previously, there are two types of noise contribute to the standard deviation of the ADU measured from the detector, we can simply take it as the mixed noise in the raw image σ_r , and the read-out noise is σ_0 , while the quantum noise is σ_p . By applying the law of error propagation to Equation 4-1, we have

$$\sigma_r^2 = \left(\frac{\partial s_r}{\partial s_0} \right)^2 \sigma_0^2 + \left(\frac{\partial s_r}{\partial (S_d + S_p)} \right)^2 \sigma_p^2 \quad \text{Equation 4-2}$$

As we know that the photon shot noise, or in other word quantum noise σ_p is proportional to the square root of the signal, we have

$$\sigma_p = \sqrt{G(S_d + S_p)} \quad \text{Equation 4-3}$$

Therefore, Equation 4-2 becomes

$$\sigma_r^2 = \sigma_0^2 + G^2(S_d + S_p) \quad \text{Equation 4-4}$$

When dark frame subtraction is introduced, we subtracted an averaged dark frame from the raw image. Similarly, we have

$$\sigma_d^2 = \sigma_0^2 + G^2 S_d \quad \text{Equation 4-5}$$

After dark frame subtraction, the noise expression in final image would be:

$$\sigma^2 = 2\sigma_0^2 + G^2(2S_d + S_p) \quad \text{Equation 4-6}$$

While the signal in the final image is $s=GS_p$

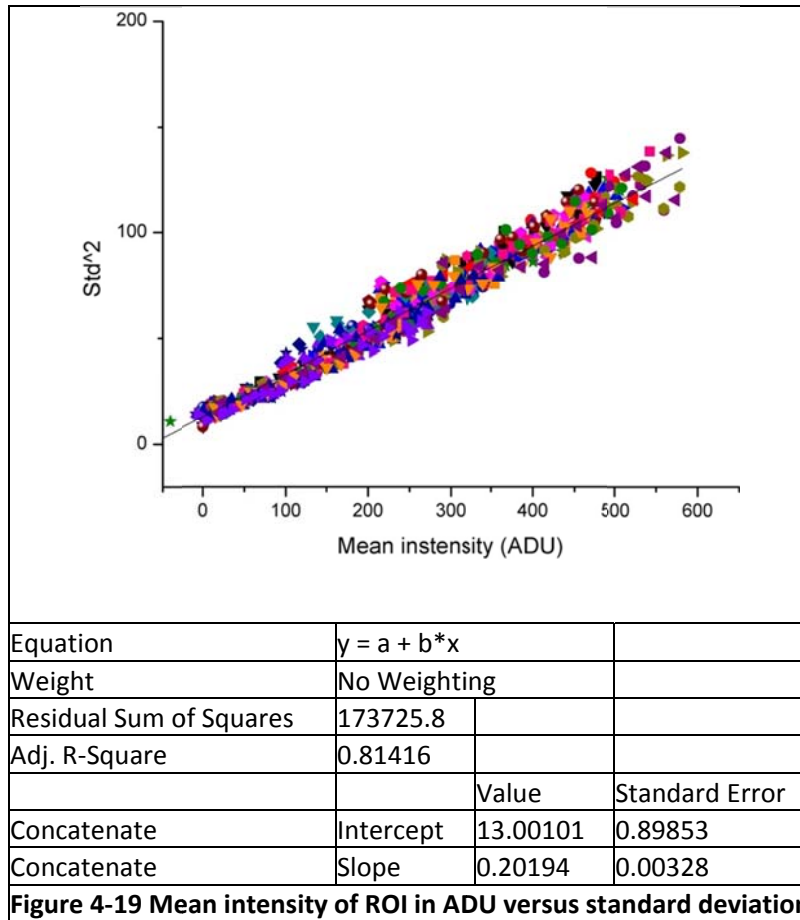
We can rewrite Equation 4-6 into:

$$\sigma^2 = \left(\sqrt{2\sigma_0^2 + 2G^2 S_d} \right)^2 + G^2 S_p \quad \text{Equation 4-7}$$

As we all know, electronic noise comprises not only noise from read-out bias, but also from the dark current. If we denote $\sigma_e = \sqrt{2\sigma_0^2 + 2G^2 S_d}$, now Equation 4-7 becomes

$$\sigma^2 = \sigma_e^2 + Gs \quad \text{Equation 4-8}$$

It is very obvious that, in a dark frame subtracted final image taken by a detector operating at certain integration time, the signal, in other words, intensity of a ROI read out in ADU has a linear relationship with the square of the standard deviation of pixel values in the same region, with the square of electronic noise as the intercept. And we noticed that the slope of this straight line corresponds to G , which we defined earlier as detector gain. Now that we have data from 4 identical exposures across 7 independent x-ray beams, with 31 different exposure windows respectively, it would provide sufficient sampling for extrapolation



As discussed previously, the intercept 13.00 ± 0.90 stands for the square of system electronic noise, therefore electronic noise σ_e in our specific setting is 3.61 ± 0.12 .

Another way to isolate electronic noise is simply subtracting the master dark frame out of any single dark image. For a certain ROI in a single dark frame, we have:

$$s_d = s_0 + GS_d + \sigma_e \quad \text{Equation 4-9}$$

When we average N frames of dark frames,

$$\overline{s_d} = \overline{s_0} + G \frac{\sum_{i=1}^N S_{di}}{N} + \frac{\sqrt{\sum_{i=1}^N \sigma_{ei}^2}}{N} \quad \text{Equation 4-10}$$

Then the subtracted dark frame becomes

$$S_{ds} = (s_0 - \overline{s_0}) + G \left(S_d - \frac{\sum_{i=1}^N S_{di}}{N} \right) + \sqrt{\sigma_e^2 + \frac{\sum_{i=1}^N \sigma_{ei}^2}{N^2}} \quad \text{Equation 4-11}$$

Electronic noise is also greatly related to detector intergration time, whereas in our experment, this parameter was kept constant, therefore, σ_e could be modeled as a constant component. Also the detector is operated in a well-cooled condition where the change of dark electrons induced by temperature change could be neglected. In the meantime, averaging multiple dark frames will smooth out the random noise in a single dark frame, getting closer to the true bias of the pixels. When subtracting the reference dark frame out from any single dark frame, we have

$$\sigma_{ds} \approx \sigma_e \sqrt{1 + \frac{1}{N}} \quad \text{Equation 4-12}$$

It is obvious that, the larger N is, the closer σ_{ds} to true electronic noise σ_e will be. Figure 4-20 depicts one single dark frame and the final image after the subtraction of the reference.

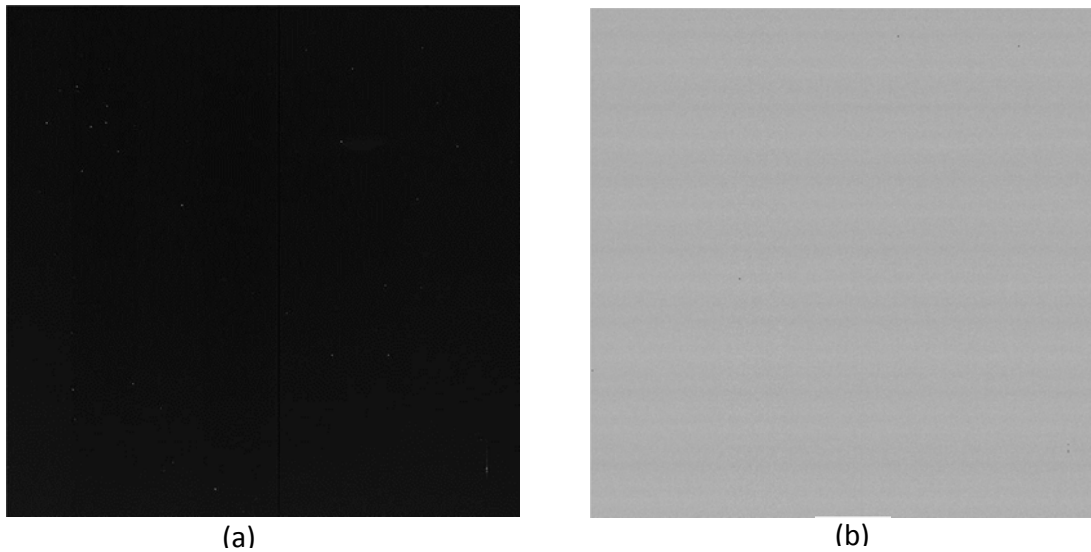


Figure 4-20 (a) is a single dark frame, (b) is the a subtracted the reference

Now we pick up a dark frame, with the correction algorithm applied, the majority of dead pixels and bright spots are removed. We then subtract the reference out of the individual dark frame, leaving pure electronic noise. The standard deviation over the FOV in the final image would then accurately represent the electronic noise of the detector.

With the same algorithm applied to all 2480 frames , we have the statistical distribution of the electronic noise illustrated in Figure 4-21. The mean value of standard deviation is 3.36 ± 0.27 , which agrees with the results we got from the intrapolation. Now we are confident to claim that the electronic noise in this specific imaging setting is about 3.5, therefore, the the P, proportional-to-constant noise ratio is demonstrated in Figure 4-22. Apparently, in our multi-beam x-ray imaging system under the experimental conditions, the majority of data we acquire are in quantum noise

dominant region where P is larger than 1, thus the binary multiplexing performs not as good as sequential imaging in terms of noise properties.

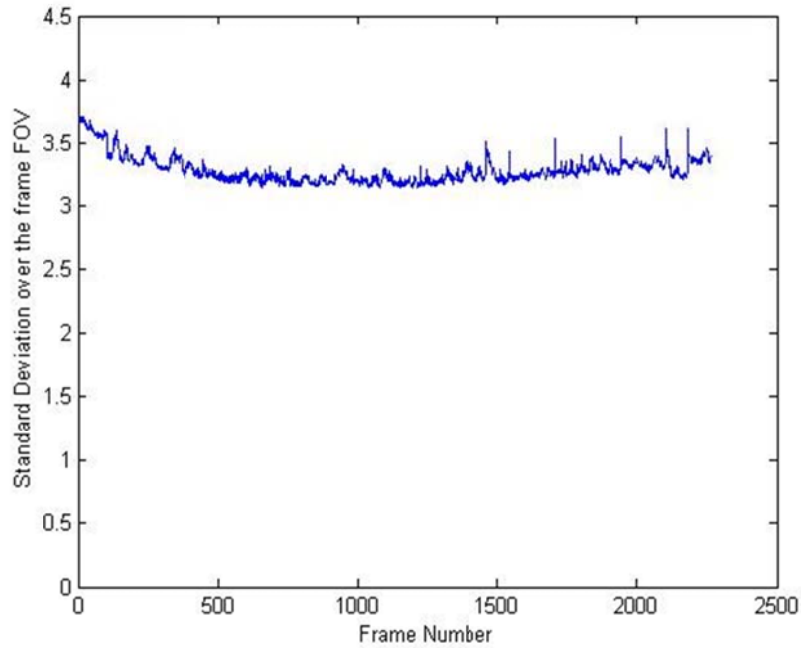


Figure 4-21 Standard deviation of all 2480 frames of dark images with the reference subtracted

Therefore, in order to find the critical point from previous simulation showed in Figure 4-13, and verify with experimental data, it's necessary to find a low-dose case where the quantum noise is negetible so that electronic noise will be dominant.

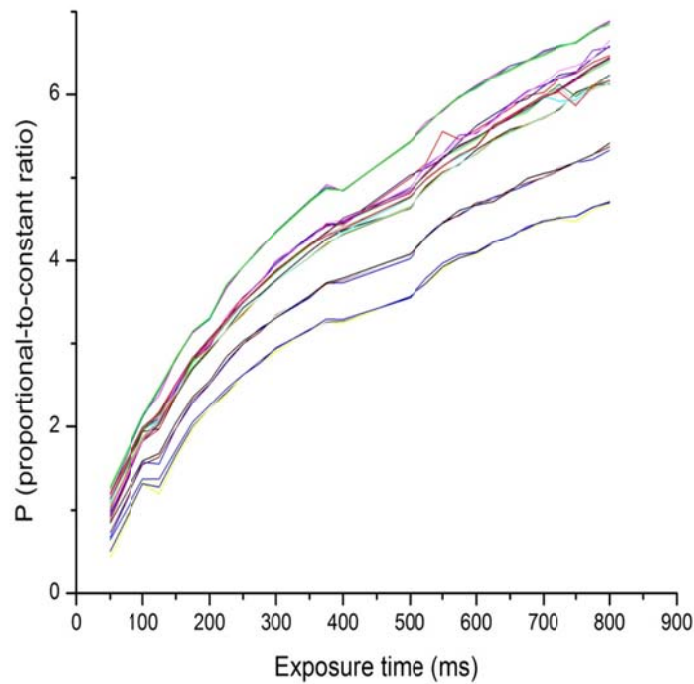


Figure 4-22 P value of our imaging system under the experimental condition. Total 28 curves were listed in the graph, illustrating data from 7 different x-ray beams with 4 identical exposures at each time spot.

In this study for relative relationship between electronic noise and quantum noise, we develop a simple mathematical model and prove it with experimental results. Two methods of isolating system electronic noise are tested in experiments. With the experiments and simulations, we have achieved better understanding for noise properties, especially electronic noise properties in our multi-beam x-ray imaging system.

The results further verifies that the proportional-to-constant noise ratio P in our system lies in the quantum noise dominant region. With the current scanning protocol,

it's essentially impossible for multiplexing mode to outperform sequential mode in terms of SNR.

To investigate the possibility of using binary multiplexing radiography for better image quality, we'll need to locate a low-dose region where the quantum noise is small enough for electronic noise to become dominant.

Now that we have figured out the relative relationship between the electronic noise and quantum noise in our specific imaging setting, a further analysis is carried on to directly compare the SNR of a certain ROI in sequential imaging mode and multiplexing mode. Another set of images is acquired with the same SNR phantom and imaging geometry. Given the currently imaging condition, an x-ray exposure longer than 50ms per frame would still be in the photon noise dominant region as indicated in Figure 4-22. We set the detector at constant 1 fps and vary the x-ray exposure from 50ms, 25ms down to 10ms. A 30 pixel \times 30 pixel ROI is chosen within a sub-region with uniform attenuation on the FOV. Then the SNR of this ROI is calculated from both demultiplexed and sequential image, denoted as SNR_{MUX} and SNR_{SEQ} respectively. A single demultiplexed image originating from one beam is used to compare with its sequential counterpart with the same length of x-ray exposure. This is essentially a *constant time* case in which multiplexing mode is able to deliver 4 times higher the dose than sequential imaging within the same amount of time.

Then the results of SNR_{MUX}/SNR_{SEQ} from the 7 beams with 3 different exposure time are recorded and compared. Since the 7 beams are essentially equivalent, we can take the mean of SNR_{MUX}/SNR_{SEQ} across the 7 beam at a certain exposure time.

As shown in Figure 4-23 that average SNR_{MUX}/SNR_{SEQ} increases to above 1 when x-ray exposure is shorter than 50ms, and such ratio keeps increasing as the x-ray exposure shortens. We have now confirmed experimentally that under certain conditions, multiplexing radiography would be able to provide images for better quality.

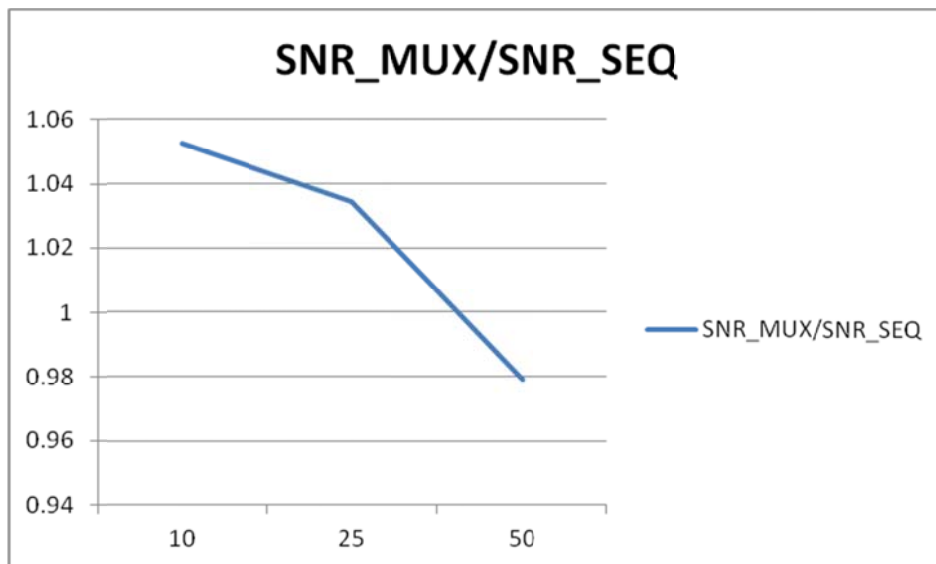


Figure 4-23 The mean of SNR ratio between a demultiplexed image and sequential image across the 7 beams.

In summary, in constant dose mode, N-beam binary multiplexing mode could acquire a data set $\frac{N+1}{2}$ times faster than sequential imaging at the expense of

compromised image quality. In some of the dose limited, high throughput screening case, such as IGRT, multiplexing radiography might be able to contribute.

On the other hand, in constant time mode, only at extreme low quantum noise scenario, multiplexing could offer even higher image quality than sequential imaging. It might be useful in a situation that needs the system to deliver more dose during a certain amount of time when the peak power of individual x-ray source is limited. In such case, N x-ray sources would be able to deliver $\frac{N+1}{2}$ times more dose in multiplexing mode than in sequential mode.

4-5 Summary

In summary, we have built a prototype MB μ CT scanner based on the CNT field emission multi-beam x-ray technology, to evaluate the feasibility of a stationary gantry-free MB μ CT. The system has been preliminary characterized and some of its basic characteristics have been measured. A mouse has been scanned using the device to test the imaging capability of the integrated imaging system. Multiplexing imaging has also been demonstrated with the system.

Our preliminary results show that the MB μ CT scanner is able to provide images with decent imaging quality. It has the potential to deliver fast CT scan speed due to its novel scanning configuration. As a prototype system, it will be used to perform various feasibility tests for the future development of a fully stationary multi-beam micro-CT scanner.

References

1. Cui, J.B. and J. Robertson, *Control of field emission current of individual sites by a local resistor*. Journal of Vacuum Science & Technology B, 2002. **20**(1): p. 19-24.
2. *European Committee for Standardization, EN 12543-5: 1999 E, Brussels*,. 1999.
3. Quan, E. and D.S. Lalush, *Evaluation of hexagonal and square geometries for motion-free arrayed-source x-ray micro-CT*. Biomedical Imaging: From Nano to Macro, 4th IEEE International Symposium, 2007: p. 221-224.
4. Zhang, J., et al., *Multiplexing radiography using a carbon nanotube based x-ray source*. Applied Physics Letters, 2006. **89**(6): p. 064106.
5. Zhang, J., et al. *Hadamard multiplexing radiography based on carbon nanotube field emission multi-pixel x-ray technology*. 2008: SPIE.
6. *Noise Sources in CMOS Image Sensors*, H.-P. Group, Editor. 1998.
7. Lundberg, K.H., *Noise Sources in Bulk CMOS*. 2002.
8. Lalush, D.S., *Binary Encoding of Multiplexed Images in Mixed Noise*. Medical Imaging, IEEE Transactions on, 2008. **27**(9): p. 1323-1332.

Chapter 5 Conclusion and future direction

CNT field emission technology has become an excellent alternative way of x-ray generation. As a result of its intrinsic field emission nature, fully digitally modulated x-ray generation, compact device size and flexible system design have been achieved with CNT x-ray source.

In this dissertation, I first introduced the fundamental background of x-ray generation and CNT field emission technology. Through the discussion, we realize that the conventional thermionic emission x-ray source has some disadvantages that limit its usage toward certain applications. The large amount of heat generation results in short life time and large device size, while the slow response time limits the temporal resolution of the x-ray source. It also requires complicated add-on apparatus to achieve finer spatial resolution, and modulated x-ray generation. On the other hand, CNT field emission x-ray source has shown some great advantages in terms of the programmability and flexibility for x-ray generation. With much simpler system design, CNT x-ray source has been able to generate fully digitized x-ray beam patterns. Thus, novel imaging geometry becomes achievable for further investigation.

CNT field emission x-ray source has been successfully integrated in a compact micro-focus tube to supply 100 μm isotropic x-ray focal spot with 100W power rating.

Equipped with this x-ray tube, a dynamic single-beam micro-CT scanner has been built and characterized. The single-beam micro-CT system is becoming a powerful tool in longitudinal biomedical research for its free-breathing live animal gated imaging capability.

As the development of CT, faster scanning speed and higher screening throughput becomes more and more desirable. However, the mechanical motion has become the bottleneck of further scanning speed improvement. Researchers have proposed various novel x-ray sources and imaging geometry to answer this challenge such as EBCT and DSR. These systems have achieved some encouraging progress but also suffer some intrinsic drawbacks which hinder their further development.

With all the aforementioned unique advantages of our CNT x-ray source, we proposed a multi-beam micro-CT scanner to test the idea of a gantry free CT geometry in which multiple x-ray sources are used to provide sufficient angle coverage for reconstruction. The overall design and preliminary characterization of this multi-beam micro-CT scanner is demonstrated. A 20-beam CNT linear x-ray source is designed and fabricated to provide micro-focus x-rays for fine spatial resolution required in micro-CT scanning. A MOSFET based control circuit is built and bundled with a homebrew LabVIEW software package. With such control electronics, the multiple CNT x-ray sources are individual addressable. Different pulsed x-ray patterns could be easily generated to suit for different imaging modes with a touch away. With the multi-beam linear geometry, our imaging system is able to cover the object from 20 different

viewing angles without any mechanical motion. In order to test the feasibility of multi-beam CT scanning, a mouse carcass is scanned. The results clearly demonstrated the multi-beam motion free scanning scheme.

Multiplexing radiography is also investigated with this system. A mouse carcass is scanned with 7-beam binary multiplexing radiography. In this imaging mode, multiple x-ray beams are switched on simultaneously at each of the 7 imaging cycles. The x-ray projections from different angles form a composite image of the object on the detector. Afterwards, projection data from individual x-ray beam could be recovered mathematically from the composite images. At the constant dose mode, 4 times of speed increase is achieved with the 7-beam multiplexing. To better understand the noise propagation in multiplexing. The noise characteristics of our imaging system have been tested. It has been confirmed that based on our imaging protocol and specific imaging setting, the system is operated in a photon noise dominant region. Therefore the speed gain in multiplexing is compensated by the SNR loss compared to sequential imaging. Multiplexing could still be very useful in applications which require high screening throughput and dose limited application such as IGRT.

Being the first multi-beam micro-CT system based on CNT multi-beam micro-focus x-ray, this system has been a powerful testing platform for novel imaging geometry. We fully realize that more work still needs to be done to better prepare this system for a comprehensive imaging application. A thorough geometry calibration is needed for the multi-beam system for the reconstruction, also specific reconstruction

algorithms are still under investigation. Overall this multi-beam micro-CT system still holds great potential for future investigation and application.